UNIVERSITY OF OKLAHOMA

GRADUATE COLLEGE

MOBILITY STUDY OF PROTEIN AND DYE MOLECULES WITHIN SILICA HYDROGEL, LIPOSOMES, AND BACTERIA CELLS BY FLUORESCENCE MICROSCOPY

A DISSERTATION

SUBMITTED TO THE GRADUATE FACULTY

in partial fulfillment of the requirements for the

Degree of

DOCTOR OF PHILOSOPHY

By

YONGYAO ZHOU
Norman, Oklahoma
2010

MOBILITY STUDY OF PROTEINS AND DYE MOLECULES WITHIN SILICA HYDROGEL, LIPOSOMES, AND BACTERIA CELLS BY FLUORESCENCE MICROSCOPY

A DISSERTATION APPROVED FOR THE
DEPARTMENT OF CHEMISTRY AND BIOCHEMISTRY

BY

Dr. Wai Tak Yip, Chair

Dr. C. LeRoy Blank

Dr. Richard W. Taylor

Dr. Robert L.White

Dr. Roger G. Harrison

Acknowledgements

First of all, I would like to express my deep gratitude to Dr. Yip, my advisor, for his guidance and support. I appreciate his patience in teaching me how to perform single molecule experiments and how to deal with all kinds of problems encountered through my Ph.D. study. Dr. Yip aroused my interest in understanding chemistry in deeper depth. He always encouraged me to think about “Why” and “How” beyond the “What” that we studied.

I would also like to express my appreciation to the members of my graduate committee, Dr.s Blank, Taylor, White, and Harrison for their helpful discussion and constructive criticism concerning my general exam, research work, analytical seminars, and other issues. I would like to thank Dr. Klebba for providing me the cells and giving me directions in the TonB project. I am also grateful to Dr. Rice for his substitution for Dr. White as my committee professor for the general exam defense and his help during the first semester I came.

I would like to thank all my group fellows, James, Ye, Becky, Tami, Qiong, Tim, Lucas, and Yan, and all my friends in the department of Chemistry and Biochemistry, at OU, and in the church for their friendship and their help. There are so many that I can not list all of them in here.

Finally I would like to thank my family. I thank my husband, Huaiwen, for his accompanying me and his encouragement during this long journey. I thank my adorable son, Andy, for making my ordinary days so special and becoming my strength moving forward. I thank my mother for her understanding of my choice in taking this long journey and her encouragement whenever I turned to her. I would also like to thank my parents-in-law for babysitting Andy during part of this time.

Table of Contents

Chapter 1: Introduction 1
1.1 Fluorescence techniques for mobility study 1
1.2 Fluorescence polarization/anisotropy (FP/FA) 3
1.3 Polarization modulation 7
1.4 Fluorescence recovery after photobleaching (FRAP) 9
1.5 Fluorescence microscopy 10
1.6 Research focus 12
1.6.1 Balance between Coulombic interactions and physical confinement inside silica hydrogel 12
1.6.2 TonB's motions in the gram negative bacteria E. Coli 13
1.6.3 Molecular Mobility under submicroscopic liposomal confinement inside the hydrogel matrix 14
Chapter 1 References 16
Chapter 2: Fluorescence Microscope Setup 19
2.1 The laser source 20
2.2 The excitation beam pathway 20
2.3 The nano-positioning sample stage 21
2.4 The emission beam pathway 21
2.5 The detectors 22
2.6 The computer program 23
2.7 Polarization alignment 23
Chapter 2 Reference 26
Chapter 3: Balance between Coulombic Interactions and Physical Confinement in Silica Hydrogel Encapsulation 27
3.1 Introduction 27
3.2 Experimental 32
3.2.1 Materials 32
3.2.2 Hydrogel preparation 33
3.2.3 Single molecule polarization 33
3.2.4 Fluorescence recovery after photobleaching (FRAP) 35

3.2.5 Steady-state fluorescence anisotropy 35
3.3 Results and Discussions 37
3.3.1 Structure and spectra characteristics of GFP, R6G, and FL 37
3.3.2 Single molecule spectroscopy 40
3.3.3 Fluorescence recovery after photobleaching 45
3.3.4 Steady-state fluorescence anisotropy (r) 50
3.4 Conclusions 56
Chapter 3 References 58
Chapter 4: TonB's Motion in the Gram Negative Bacteria E. Coli 62
4.1 Introduction 62
4.2 Experimental 68
4.2.1 Materials 68
4.2.2 Preparation of samples 69
4.2.3 Real-time fluorescence anisotropy measurements 70
4.2.4 Fluorescence recovery after photobleaching (FRAP) 71
4.3 Results and discussion 71
4.3.1 Fluorescence images 71
4.3.2 Fluorescence recovery after photobleaching (FRAP) 72
4.3.3 Fluorescence anisotropy measurements by microscopy 74
4.3.4 Comparison between the anisotropy of GFP-TonB and cyto- GFP in E. Coli cells 81
4.3.5 Comparison between the anisotropy of GFP-TonB and FM-FepA in E. Coli cells 83
4.3.6 Effect of the energy inhibitor carbonyl cyanide m-chlorophenyl hydrazone (CCCP) on GFP-TonB's motion 91
4.3.7 Effect of the energy inhibitor 2,4-dinitrophenol (DNP) on GFP-TonB's motion 96
4.3.8 Effect of the energy inhibitor sodium azide on GFP-TonB's motion 100
4.3.9 Change of anisotropy in GFP-TonB during iron transport 103
4.3.10 Comparison between the anisotropy of GFP-TonB and GFP-TonB with ExbB and ExbD deleted in E. Coli cells 107
4.4 Conclusion 109
Chapter 4 References 112
Chapter 5: Molecular Mobility under Submicroscopic Liposomal Confinement inside the Hydrogel Matrix 115
5.1 Introduction 115

5.2 Experimental 118
5.2.1 Materials 118
5.2.2 Preparation of dye loaded liposomes 119
5.2.3 Preparation of the liposome-incorporated hydrogel 120
5.2.4 Fluorescence modulations..... 121
5.2.5 Fluorescence anisotropy bulk measurements..... 123
5.2.5 Fluorescence anisotropy of FL in single liposomes..... 124
5.3 Results and discussion..... 125
5.3.1 Separation of dye-doped liposomes from the free dye residue..... 125
5.3.2 Fluorescence images 126
5.3.3 Polarization modulation..... 127
5.3.4 Steady-state fluorescence anisotropy..... 134
5.3.5 Fluorescence anisotropy of single FL-liposomes 137
5.4 Conclusion..... 140
Chapter 5 References..... 142

Lists of Tables

Table 3.1 Properties of R6G, FL, and GFP 39

Table 3.2 Single-molecule mobility distributions of R6G in Silica hydrogel and alcogel... 44

Table 3.3 Single-molecule mobility distribution of GFP and R6G in silica hydrogels..... 45

Table 3.4 Fluorescence recovery rate of FL encapsulated in hydrogel and free FL in water 47

Table 3.5 Steady-state fluorescence anisotropy of FL and R6G 51

Table 5.1 Fluorescence anisotropy of R6G in different samples 134

Table 5.2 Anisotropy of FL in liposomes of different sizes 138

List of Figures

Figure 2.1 Diagram of a home-built confocal microscope 19

Figure 2.2 Confocal fluorescence polarization microscope setup. 24

Figure 2.3 Modulation curves of FL molecules inside the alcogel thin film. 26

Figure 3.1 Structures of R6G (A), FL (B), and GFP (C). 39

Figure 3.2 Fluorescence excitation and emission spectra of FL (A), R6G (B), and GFP (C). 39

Figure 3.3 Fluorescence images of (A) GFP, (B) R6G, and (C) FL encapsulated in silica hydrogels. 40

Figure 3.4 Fluorescence recovery traces of FL in hydrogel after photobleaching. 46

Figure 3.5 Fluorescence recovery traces of FL in water. 49

Figure 3.6 Time evolution of fluorescence anisotropy of FL (top) and R6G (bottom) 52

Figure 3.7 Fluorescence anisotropy values of hydrogel encapsulated R6G as the pH of the Hydrogel decreases 54

Figure 3.8 Encapsulation model of R6G (star) during hydrogel formation. 55

Figure 4.1 Structure of enterobactin 63

Figure 4.2 Proteins involved in iron transport and their locations 64

Figure 4.3 Fluorescence images of GFP-TonB and cyto-GFP *E. Coli* cells 72

Figure 4.4 Fluorescence images of cells before and after photobleaching. 74

Figure 4.5 *G* factors as a function of focus positions 77

Figure 4.6 Anisotropy distribution of GFP-TonB (A) and GFP-in-cytoplasm(B) 82

Figure 4.7 Anisotropy distribution of FM-FepA (A) and GFP-TonB (B). 84

Figure 4.8 Localizations of FM-FepA and GFP-TonB..... 85

Figure 4.9 FM fluorescence modification to the cystine residue of FepA at S271C..... 86

Figure 4.10 Structure of CCCP..... 91

Figure 4.11 The anisotropy of GFP-TonB before and after adding CCCP 94

Figure 4.12 UV spectrum and structure of DNP..... 97

Figure 4.13 The anisotropy of GFP-TonB before (A) and after (B) adding DNP and the anisotropy change after adding DNP (C). 98

Figure 4.14 Structure of sodium azide..... 100

Figure 4.15 The anisotropy of GFP-TonB before (A) and after (B) adding azide and the anisotropy change after adding azide (C). 102

Figure 4.16 The anisotropy of GFP-TonB before (A) and after (B) adding FeEnt and the anisotropy change before and after adding FeEnt (C) 105

Figure 4.17 The anisotropy of GFP-TonB (A) and GFP-TonB-Mutant (B)..... 108

Figure 5.1 The separation of R6G-liposomes from free R6G solution by Nap^{TM} -10 column..... 126

Figure 5.2 Fluorescence images of R6G-liposomes (200 nm) in a hydrogel 127

Figure 5.3 Fluorescence time trace of ensemble R6G molecules for four periods..... 130

Figure 5.4 The fluorescence modulations of ensemble R6G molecules inside different sizes of liposomes entrapped in hydrogel. 133

Figure 5.5 Structure of DMPC (A), R6G (B), and FL (C)..... 136

Figure 5.6 The fluorescence anisotropy distribution of FL-liposomes..... 139

Abstract

Fluorescence techniques are very useful for understanding the various processes in biological science. This thesis presents the applications of several fluorescence techniques for studying the mobility of proteins and fluorescence dyes inside the living cells and in the silica hydrogel materials.

Chapter 1 gives a brief introduction of various fluorescence techniques, including fluorescence polarization and anisotropy, fluorescence recovery after photobleaching, fluorescence modulation, etc. In addition, the basic principle of fluorescence microscopy is covered.

Chapter 2 talks about the setup of the home-built fluorescence microscope as well as the polarization alignment that were applied in this thesis.

In Chapter 3, the behavior of various entrapped guest molecules within a silica hydrogel was investigated and the effects of Coulombic interactions and physical confinement on molecular mobility were evaluated using fluorescence techniques.

In Chapter 4, the motion of *E. Coli* inner membrane protein TonB was studied using fluorescence anisotropy in order to understand TonB's mechanism in facilitating iron transport in *E. Coli*.

In Chapter 5, the effects of the submicroscopic confinement exerted by the liposomes in the hydrogel on the mobility of entrapped molecules were examined using fluorescence polarization modulation and fluorescence anisotropy.

Chapter 1: Introduction

In this chapter, a brief overview about the fundamental principles and the applications of the fluorescence techniques is presented as background to our projects. Focus will be on fluorescence polarization and anisotropy, polarization modulation, and fluorescence recovery after photobleaching, which were used in the research projects. Since most of these fluorescence measurements (either single-molecule or ensemble measurements) were performed by a fluorescence microscope, the basic principle of fluorescence microscopy is also covered. In addition, the research focuses of the three projects are summarized.

1.1 Fluorescence techniques for mobility study

Understanding the dynamics of biological molecules, such as proteins, DNAs, and RNAs, is very important because functions of these molecules depend on not only their structures but also their dynamics. For instance, the inner membrane protein TonB, which is studied in this thesis, is believed to facilitate iron transport in bacteria. To fulfill its function, it is believed to undergo a series of conformational changes[1] or even constant surveying motions[2]**.** Mobility is also important for biological molecules studied in vitro. For instance, as used in silica sol-gel based biocomposites, biomolecules are trapped inside the gel network where motions are restricted. It is very important to ensure that inside the confined structure, macromolecules are able to maintain some kind of molecular

flexibility as a requirement for their functions.

Fluorescence techniques are now widely used in chemical and biological science. Fluorescence detection is highly sensitive, and has almost completely replaced the radioactive tracer methods in biochemical measurements and in medical research. Fluorescence techniques have extremely high resolution, which allows local observation of complex biological processes. Several fluorescence methods are available for the study of the dynamics of macromolecules in real time, such as fluorescence correlation spectroscopy (FCS)[3,4], fluorescence resonance energy transfer (FRET)[5-7], fluorescence polarization and anisotropy (FP/FA)[8,9], fluorescence recovery after photobleaching (FRAP)[10,11], to name just a few.

FCS measures the fluorescence intensity fluctuations to obtain quantitative information such as diffusion coefficients, hydrodynamic radii, average concentrations, and so on. FRET monitors distance changes between two fluorophores and tracks molecular motions between two dye-labeled sites on a macromolecule. FP/FA methods make use of fluorescence polarization to track the orientation and rotational diffusion of molecules. FRAP allows one to obtain the translational diffusion information of molecules and the molecular environment by deliberately photobleaching the molecules and observing their fluorescence recovery.

The extremely high sensitivity and resolution of fluorescence measurements even allows the observation of dynamics down to a single molecule level. Compared to bulk measurements, where only average characteristics are measured, single molecule

measurements can distinguish the individual behaviors. Single molecule fluorescence spectroscopy allows one to probe local heterogeneity and obtain distribution information, making it a very useful tool for understanding the heterogeneous chemical and biological properties of complex systems. While most single molecule measurements are performed by immobilizing the fluorophores (or the fluorophore-labelled molecules) on a surface or inside a gel matrix, they can be used for real-time observation of intracellular molecules with slight diffusions such as conformational changes of proteins and binding dynamics between proteins and DNAs[12-16].

1.2 Fluorescence polarization/anisotropy (FP/FA)

FP/FA measurements are based on the principle of photoselective excitation of the fluorophores by polarized light. Each fluorophore has a transition dipole moment ($\vec{u}$). Both the absorption and emission photons are polarized and oriented along the instantaneous direction of the transition dipole moment ($\vec{u}(t)$). When linearly polarized light shines on molecules with random orientations, those molecules with their $\vec{u}(t)$ aligned mostly along the electric field ($\vec{E}$) are selectively excited. Emission from the fluorophores also occurs along $\vec{u}(t)$. Fixed molecules, when excited, will stay aligned parallel with $\vec{E}$ during the process of emission, and as a result the emission will be polarized along $\vec{E}$. Molecules undergoing free Brownian motions will randomize the initial dipole orientation, resulting in a depolarized emission. The degree of polarization in the emission is defined by two terms, polarization (*P*) and anisotropy(*r*), expressed below

as,

$$P = \frac{I_{II} - I_{\perp}}{I_{II} + I_{\perp}}$$

$$r = \frac{I_{II} - I_{\perp}}{I_{II} + 2I_{\perp}}$$

where I_{II} is the emission intensity along the excitation polarization and $I_{\perp}$ is the emission intensity perpendicular to the excitation polarization. Polarization and anisotropy express the same information content and are interchangeable. They differ only in normalization. While polarization was used more often in earlier publications, anisotropy is now preferred because it is normalized by the total intensity $(I_{II} + 2I_{\perp})$.

When a population of randomly oriented molecules that do not rotate (for example, in a solution with very high viscosity) is excited, the emission will be predominantly polarized along the excitation polarization, which gives the maximum *P* value at +0.5 or maximum *r* at +0.4. For molecules in solution, however, a considerable amount of rotational diffusion during the excited state lifetime results in the depolarization of the emission ($-0.33 < P < +0.5$ and $-0.20 < r < +0.4$). The negative values of polarization and anisotropy are not very common and are possible only when the perpendicular intensity is larger than the parallel intensity, which can happen when the angle of the absorption and emission of the fluorophore is larger than 54.7 degree.

In 1920, scientists found that the degree of polarization is related to the molecular size, viscosity of the medium, and temperature. Considering all these, they realized that polarization is related to the mobility of the emitting substances. It was found that

polarization decreases as their mobility increases. Several years later, Francis Perrin related polarization to both the excited state lifetime and the rotational diffusion of a fluorophore and developed what is now called the Perrin equation[17],

$$\frac{r_0}{r} = 1 + \frac{\tau}{t_r} = 1 + 6D_r\tau$$

Where r_0 is the maximum fluorescence anisotropy, t_r is the rotational correlation time (which describes how fast a molecule rotates), τ is the fluorescence lifetime, and D_r is the rotational diffusion coefficient. t_r is related to viscosity (η), temperature (T), and the volume of the rotational unit (V), as expressed by the following equation for spherical molecules,

$$t_r = \frac{\eta V}{RT}$$

where R is the gas constant. As seen from the equation, larger molecules will have a longer correlation time than small molecules. Fluorescence anisotropy can be seen as a competition between the molecular rotation and the fluorescence lifetime of the fluorophore as shown in the Perrin equation. If the fluorescence lifetime of the fluorophore is much longer than the rotational correlation time, fluorescence anisotropy will be small. If the fluorescence lifetime is much shorter than the rotational correlation time, fluorescence anisotropy will be large.

The relationship between observed anisotropy and the rotational mobility of the fluorophore thus makes fluorescence anisotropy very useful for many biological science

and diagnostic fields. FP/FA is used to extract physical properties such as the size, shape, and rotational dynamics of macromolecules, which are then used to understand the chemical and biological properties. Fluorescence polarization measurements were used to observe protein-ligand binding and measure the binding constants [8,18,19]. The applications are based on the following: when a fluorescent ligand (usually small fluorescent molecules) binds to a protein, its fluorescence polarization/anisotropy will increase accordingly to reflect the slower rotation of the ligand–protein complex relative to the free ligand. Using polarization or anisotropy data, one can calculate the fraction of the ligand bound (x) at any protein concentration and then calculate the dissociation constant [18]. The same principle was extended to study substrate-protein[20], protein-protein, and protein-DNA interactions[21]. The first instrument designed specifically for clinical chemistry applications of fluorescence polarization was described by Spencer et al[22]. Afterwards, FP was applied for the immunoassays of numerous substances, such as drugs[23,24], antibiotics[25], fungal toxins[24], and so on. For example, for the fluorescence polarization immunoassay (FPIA) of a toxin (from the sample), the toxin (from known standard solution) is first covalently linked to a fluorophore to make a fluorescent tracer. The tracer will compete with the toxin from the sample to react with a limited amount of toxin-specific antibody. The sample was added with the antibody and then the tracer. When the sample does not contain the toxin, the antibody binds the tracer, restricting its motion and causing a high polarization. When the sample contains the toxin, fewer tracers are bound to the antibody and a greater fraction exists unbound in solution, where it has a lower polarization.

Different from other immunoassay methods, such as the most popular enzyme-linked immunosorbent assay (ELISA), FPIA does not require the separation of the free and bound tracer.

1.3 Polarization modulation

Similar to fluorescence polarization/anisotropy, polarization modulation uses linearly polarized light to excite the fluorophores. The difference is, instead of a fixed polarization, polarization modulation uses a modulated polarized excitation by adding a half-wave plate in the polarized excitation light pathway. The polarization direction of the excitation light is modulated from 0 to 180 degrees by the half-wave plate. For a single molecule, the intensity of the emission signal *I(t)* is proportional to the absorption, that is, $I(t) \propto \left|\vec{u} \cdot \vec{E}(t)\right|^2$ or to $cos^2(\theta)$ [26], where $\vec{u}$ is the molecular transition dipole moment, $\vec{E}$ is the electric field of the excitation light, and θ is the angle between $\vec{u}$ and $\vec{E}$.

Polarization modulation is able to probe both static orientations and rotational mobilities of single molecules through the analysis of the modulation depth and phase[27]. When excited by modulated polarized light, a fixed fluorophore obtains the maximum absorption when the polarization of the excitation beam is parallel with the transition dipole of the fluorophore and obtains the minimum absorption when the polarization is orthogonal to the transition dipole of the fluorophore. For a freely rotational fluorophore, the fast rotation of the transition dipole randomizes the absorption orientation, thus eliminating the modulation. The modulation depth of the emission curve of an immobile

fluorophore is thus larger than that of a mobile fluorophore; therefore modulation depth is a measure of the mobility of the molecules. The phase of modulated fluorescence can also distinguish the different mobilities. Similar to polarization/anisotropy measurements, the fluorescence intensity of the fluorophore is separated into parallel and perpendicular components, namely, I_{II} and $I_{\perp}$. I_{II} and $I_{\perp}$ are fit to $I(t)= A\cos^2(\alpha-\phi)+C$, where $I(t)$ is the fluorescence intensity for either the parallel or the perpendicular components, A is the amplitude of the cosine square curve, α is the polarization angle, ϕ is the phase shift, and C is the background. For an immobilized single molecule, the I_{II} and the $I_{\perp}$ curves are on phase. For a tumbling single molecule, there is a 90 degree phase shift between the I_{II} and the $I_{\perp}$ curves. For an intermediate molecule, the phase shift is between 0 and 90 degrees. The modulation phase shifts of ensemble molecules are quite different from that of single molecules, as will be discussed in this project.

Polarization modulation was used to observe the dynamics of single dye molecules absorbed on a glass surface[26,28-31]. Guttler et al used polarization modulation to study the orientations of the transition dipole moments of single pentacene molecules located in p-terphenyl[30]. Xie et al modulated the polarization of the excitation light between the x and y directions, and ruled out the possibility of molecular reorientation as the origin of the sudden emission jumps happening in single dye molecules of sulforhodamine 101 that are bound to DNA[28]. Ha et al modulated the excitation polarization continuously to observe and distinguish the origin of the abrupt photophysical events of single Texas red and tetramethylrhodamine molecules[26]. Single molecule polarization modulation was used

to characterize the dynamics of protein-protein interactions involved in calcium signaling in the biological system. The modulation depth and phase shift of the fluorescence trajectories were determined to measure the orientational mobility of the molecules[27].

1.4 Fluorescence recovery after photobleaching (FRAP)

Compared to other fluorescence techniques, FRAP is simple in both theory and practice. When a small spot of a sample containing mobile fluorescent molecules is exposed to a brief, intense laser excitation, molecules in that region are subjected to irreversible photobleaching, causing a sharp decrease in fluorescence intensity. Subsequent recovery of fluorescence is observed when the laser beam is attenuated back to a lower level. Recovery of fluorescence occurs due to the translational diffusion of unbleached fluorophores into the bleached spot from other areas of the sample. The translational diffusion coefficient can be determined by measuring the rate of fluorescence recovery. FRAP can also be used to identify the different transport processes through the shape of the recovery curves, which reflects underlying biological processes [32].

FRAP was developed in the 1970s; now with the advent of GFP fusion technology, it is widely used to study macromolecular dynamics in biological cells[33]. Sprague et al used FRAP to investigate binding interactions in live cells[32]. Using FRAP, Tripathi et al observed the differential dynamics of the splicing factor SC35 during the cell cycle[34]. Dundr et al used FRAP to study the dynamics of the recruitment of RNA pol I components to endogenous ribosomal genes[35]. Lever et al observed histone H1-chromatin interactions

in human living cells by fusing GFP to H1 and monitoring H1 movement by FRAP[36].

1.5 Fluorescence microscopy

Fluorescence microscopes require the following basic components, an excitation light source, an excitation filter, a dichroic mirror that reflects light shorter than a certain wavelength (the excitation light) and transmits light longer than that wavelength (the emission light), an objective, an emission filter, and a detector.

Most florescence microscopes are epifluorescence microscopes, that is, the objective lens is used twice, both to illuminate and to image the sample. This gives an improved signal to noise ratio because most excitation light is transmitted through the sample, only reflected excitation light reaches the objective together with the emitted light.

Confocal fluorescence microscopy (CFM)[37] is an advanced optical technique designed to obtain higher-quality images with better resolution compared to the conventional wide-field microscopes. The two key features in CFM are point illumination and the use of a pinhole at the conjugated plane situated in front of the detector. Point illumination avoids most of the unwanted scattered light from entire illumination of a sample, which obscures the image. The pinhole blocks the signal that is out of focus, which otherwise would cause a background haze in the image. CFM enables one to obtain serial optical sections by imaging the sample at a different depth each time. These serial images can then be re-assembled to form a 3D image of the sample using digital image processing techniques. Like conventional wide-field microscopes, the drawback of CFM is that the resolution is

inherently limited by diffraction. The size of the Airy disk on the image is determined by the wavelength of the excitation light and the numerical aperture of the objective lens. The best resolution that is achieved by CFM was reported to be about 200 nm [37] based on the Rayleigh criterion, which states that two Airy disks must be separated by at least their radii in order to be resolved. This diffraction-limited spatial resolution restricts its usefulness in studying nanometer level structural information associated with complex biological samples.

Different from CFM, total internal reflection fluorescence microscopy (TIRFM) uses evanescent waves to illuminate a thin region of a sample at the glass surface. When the excitation light strikes on one side of the glass surface at an angle larger than the critical angle, and if the refractive index of the other side is lower, all of the light is reflected. The evanescent wave is generated at the glass-water interface of the sample, penetrating to a depth of only roughly 100 nm into the sample, thus providing high axial discrimination. Similar to CFM, the horizontal resolution of TIRFM is diffraction-limited to about half of the wavelength used, which is the characteristic of wide-field microscopy.

Near-field scanning optical microscopy (NSOM), on the other hand, overcomes the diffraction limit. NSOM offers sub-diffraction resolution on the order of 50-100 nm, which is determined by the optical aperture of a tapered fiber tip. The drawbacks of NSOM are the significant tip disturbance to the sample and low excitation signal.

1.6 Research focus

This thesis is focused on investigating the mobility of molecules in a silica hydrogel matrix and in living cells using fluorescence techniques. Three projects are included. The first project investigated the balance between Coulombic interactions and physical confinement within silica hydrogel encapsulation. The second project was focused on studying the mobility and activity of a membrane protein TonB in living bacteria cells. On the third project, the focus was to examine how the spatial restriction exerted by the liposomes might affect the mobility of the entrapped molecules.

1.6.1 Balance between Coulombic interactions and physical confinement inside silica hydrogel

Controlling the mobility of entrapped molecules within sol-gel derived materials is very important because many applications require some molecular flexibility to maintain their functions. Among the various guest-host interactions, Coulombic interactions and physical confinement are two important forces dictating the mobility of entrapped molecules inside silica sol-gel materials. In this project we examined the behavior of various entrapped guest molecules within a silica hydrogel and evaluated the effects of Coulombic interactions and physical confinement on molecular mobility using fluorescence techniques. The cationic R6G and anionic FL dyes were used as molecular probes in view of their similar molecular structures so that any difference in their behavior

could be confidently attributed to their opposite molecular charges. The green fluorescence protein (GFP) was used to examine the effect of molecular templating on mobility. Single molecule spectroscopy imaging and fluorescence polarization measurements were used to reveal the information about the rotational mobility of single molecules whereas fluorescence recovery after photobleaching enabled us to look into the translational diffusion of molecules. Steady-state fluorescence anisotropy of R6G and FL in hydrogel under various conditions were monitored and compared in order to understand the encapsulation mechanism of the guest molecules. Results of these experiments provide a better understanding of guest-host interactions in silica hydrogel and suggest possible future applications based on our findings, i.e. the repulsion between FL and silica could be used to monitor the change in viscosity and physical confinement during hydrogel formation.

1.6.2 TonB's motions in the gram negative bacteria *E. Coli*

It is believed that the cytoplasmic membrane protein TonB is required for the transduction of energy from the inner membrane to the outer membrane receptor for the transport of iron-siderophore complex, but precisely how it interacts with the receptors and how it transports energy across the periplasmic space remains an unsolved question. To understand the mechanism of TonB' functions, several theories have been postulated. One of the prevailing models suggests that TonB remains anchored to the cytoplasmic membrane and undergoes constant motions to facilitate energy transduction for iron

transport[2].

In an effort to understand the TonB function, we used fluorescence anisotropy to monitor the motions of TonB in living *E. Coli* cells. The GFP-TonB hybrid protein was expressed in the wild type *E. Coli* strain BN1071. It was constructed by genetically engineering GFP to the N-terminus of TonB. The GFP-TonB protein was found to maintain TonB's function and GFP's fluorescence. The mobility of the bacteria inner membrane protein TonB in single living cells was studied based on observing changes in the anisotropy of GFP using fluorescence anisotropy. The mobility of GFP expressed in different locations in the bacteria cells as well as the motion of the fluorescent label fluorescein maleimide (FM) bound to the outer membrane protein FepA are compared to demonstrate the validity of our methodology. The work was then focused on monitoring the rotational change of GFP-TonB at different conditions, such as adding different energy inhibitors to stop its energy source and adding the iron-enterobactin complex to motivate iron transport. The findings of this project would contribute an important step to the full understanding of the bacteria membrane protein TonB in facilitating iron transport.

1.6.3 Molecular Mobility under submicroscopic liposomal confinement inside the hydrogel matrix

Previously, a liposome-based bioencapsulation protocol was developed in our lab[38], which produced active silica sol-gel biocomposites. In the protocol, enzymes were encapsulated inside the liposomes (200 nm in diameter), which were then trapped in a

hydrogel. The liposomes served as a protective coating to prevent the enzymes from interacting with the active silane reagent. Meanwhile the liposomes templated the pore sizes of the hydrogel and thus eliminated the templating effect that the proteins may have when they were directly trapped in the hydrogel.

In this project, we are interested in understanding the effect of the submicroscopic confinement exerted by the liposomes on the mobility of entrapped molecules. The R6G and FL serve as the fluorescence probes due to their opposite charge and similar molecular structure. Fluorescence polarization modulation and fluorescence anisotropy were used to evaluate and measure the mobility of R6G and FL in the liposomes of different sizes (100 nm, 200 nm, and 400 nm in diameter). This study would provide valuable information for the applications of the liposome-based silica sol-gel bioencapsulation method.

Chapter 1 References

(1) Larsen, R. A.; Thomas, M. G.; Postle, K. *Mol. Microbiol.* **1999**, *31*, 1809.

(2) Kaserer, W. A.; Jiang, X.; Xiao, Q.; Scott, D. C.; Bauler, M.; Copeland, D.; Newton, S. M. C.; Klebba, P. E. *J. Bacteriol.* **2008**, *190*, 4001.

(3) Pristinski, D.; Kozlovskaya, V.; Sukhishvili, S. A. *J. Chem. Phys.* **2005**, *122*, 14907.

(4) Schwille, P.; Haupts, U.; Maiti, S.; Webb, W. W. *Biophys. J.* **1999**, *77*, 2251.

(5) Clegg, R. M. *Curr. Opin. Biotechnol.* **1995**, *6*, 103.

(6) Wu, P.; Brand, L. *Anal. Biochem.* **1994**, *218*, 1.

(7) Sapsford, K. E.; Berti, L.; Medintz, I. L. *Angew Chem. Int. Ed. Eng.* **2006**, *45*, 4562.

(8) Jameson, D. M.; Croney, J. C. *Comb. Chem. High Throughput Screen.* **2003**, *6*, 167.

(9) Kawski, A. *Crit. Rev. Anal. Chem.* **1993**, *23*, 459

(10) Axelrod, D.; Koppel, D. E.; Schlessinger, J.; Elson, E.; Webb, W. W. *Biophys. J.* **1976**, *16*, 1055.

(11) Sprague, B. L.; McNally, J. G. *Trends Cell Biol.* **2005**, *15*, 84.

(12) Lu, H. P. *Acc. Chem. Res.* **2005**, *38*, 557.

(13) Nan, X.; Sims, P. A.; Chen, P.; Xie, X. S. *J. Phys. Chem. B* **2005**, *109*, 24220.

(14) Yu, J.; Xiao, J.; Ren, X.; Lao, K.; Xie, X. S. *Science* **2006**, *311*, 1600.

(15) Lord, S. J.; Lee, H. L.; Moerner, W. E. *Anal. Chem.* **2010**, *82*, 2192.

(16) Ueda, M.; Sako, Y.; Tanaka, T.; Devreotes, P.; Yanagida, T. *Science* **2001**, *294*, 864.

(17) *Principles of Fluorescence Spectroscopy*; Third Edition ed.; Lakowicz, J. R., Ed.; Springer, 2006.

(18) Jameson, D. M.; Mocz, G. In *Protein-Ligand Interactions: Methods and Applications*; Nienhaus, G. U., Ed. 2005, p 301.

(19) Laurence, D. J. *Biochem. J.* **1952**, *51*, 168.

(20) Rozema, D. B.; Poulter, C. D. *Biochemistry* **1999**, *38*, 13138.

(21) Rusinova, E.; Tretyachenko-Ladokhina, V.; Vele, O. E.; Senear, D. F.; Alexander Ross, J. B. *Anal. Biochem.* **2002**, *308*, 18.

(22) Spencer, R. D.; Toledo, F. B.; Williams, B. T.; Yoss, N. L. *Clin. Chem.* **1973**, *19*, 838.

(23) Jolley, M. E.; Stroupe, S. D.; Schwenzer, K. S.; Wang, C. J.; Lu-Steffes, M.; Hill, H. D.; Popelka, S. R.; Holen, J. T.; Kelso, D. M. *Clin. Chem.* **1981**, *27*, 1575.

(24) Maragos, C. M.; Jolley, M. E.; Plattner, R. D.; Nasir, M. S. *J. Agric. Food Chem.* **2001**, *49*, 596.

(25) Jolley, M. E.; Stroupe, S. D.; Wang, C. H. J.; Panas, H. N.; Keegan, C. L.; Schmidt, R. L.; Schwenzer, K. S. *Clin. Chem.* **1981**, *27*, 1190.

(26) Ha, T.; Glass, J.; Enderle, T.; Chemla, D. S.; Weiss, S. *Phys. Rev. Lett.* **1998**, *80*, 2093.

(27) Osborn, K. D.; Singh, M. K.; Urbauer, R. J.; Johnson, C. K. *ChemPhysChem* **2003**, *4*, 1005.

(28) Xie, X. S.; Dunn, R. C. *Science* **1994**, *265*, 361.

(29) Ha, T.; Enderle, T.; Chemla, D. S.; Selvin, P. R.; Weiss, S. *Phys. Rev. Lett.* **1996**, *77*, 3979.

(30) Guttler, F.; Sepiol, J.; Plakhotnik, T.; Mitterdorfer, A.; Renn, A.; Wild, U. P. *J. Lumin.* **1993**, *56*, 29.

(31) Ha, T.; Laurence, T. A.; Chemla, D. S.; Weiss, S. *J. Phys. Chem. B* **1999**, *103*, 6839.

(32) Sprague, B. L.; Pego, R. L.; Stavreva, D. A.; McNally, J. G. *Biophys. J.* **2004**, *86*, 3473.

(33) Houtsmuller, A. B. *Adv. Biochem. Eng. Biotechnol.* **2005**, *95*, 177.

(34) Tripathi, K.; Parnaik, V. K. *J. Biosci.* **2008**, *33*, 345.

(35) Dundr, M.; Hoffmann-Rohrer, U.; Hu, Q.; Grummt, I.; Rothblum, L. I.; Phair, R. D.; Misteli, T. *Science* **2002**, *298*, 1623.

(36) Lever, M. A.; Th'ng, J. P.; Sun, X.; Hendzel, M. J. *Nature* **2000**, *408*, 873.

(37) Prasad, V.; Semwogerere, D.; Weeks, E. R. *J. Phys.-Condens. Mat.* **2007**, *19*.

(38) Li, Y.; Yip, W. T. *J. Am. Chem. Soc.* **2005**, *127*, 12756.

Chapter 2: Fluorescence Microscope Setup

The fluorescence images and kinetics traces of various molecules studied in this thesis, including single dye and protein molecules, liposomes, and bacteria cells, were obtained using a home-built sample scanning microscope (confocal or otherwise, depending on whether a pinhole is used or not). The instrument is based on an inverted microscope (Nikon, TE-200 or TE-300) and a nano-positioning stage equipped with position feedback electronics. The instrumental setup is shown in Figure 2.1.

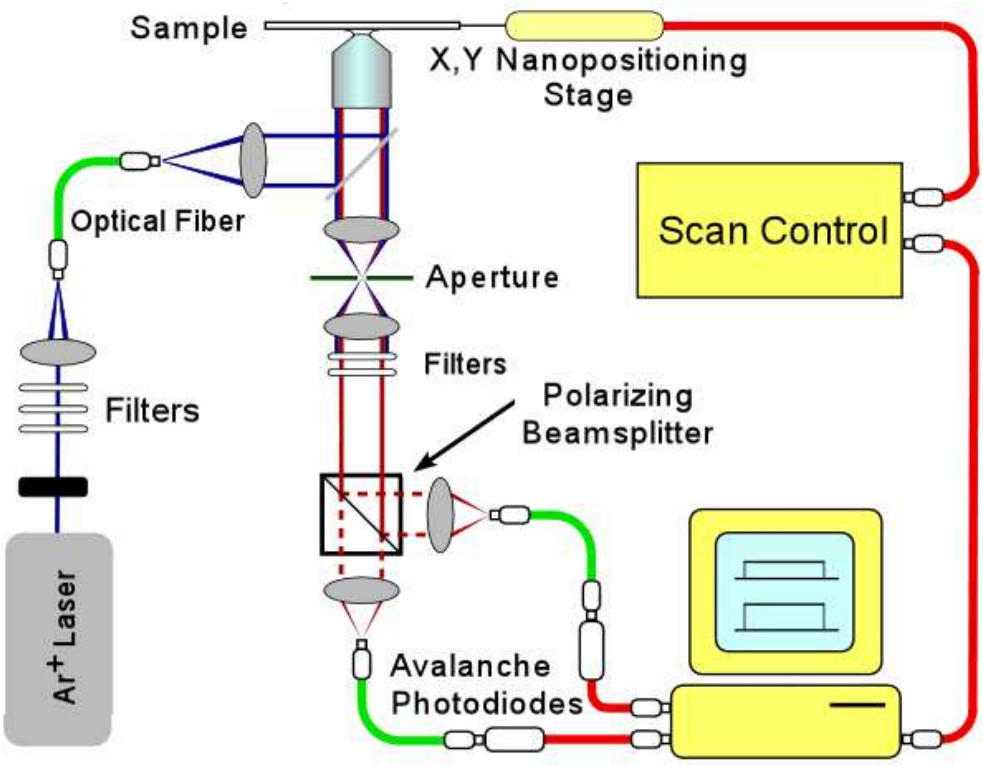

Figure 2.1 Diagram of a home-built confocal microscope

2.1 The laser source

The light source is an argon-ion laser which provides 514 nm, 488 nm, and 457 nm continuous excitation wavelengths. Selection of an excitation wavelength is obtained by dispersing the laser light using a prism and blocking the undesired wavelengths from continuing along the beam path using three adjustable apertures and reflecting mirrors.

2.2 The excitation beam pathway

The laser light with chosen wavelength is passed through a quarter-wave plate which allows us to tune the light to be circularly polarized or linearly polarized when necessary. For single molecule polarization experiments, a circularly polarized excitation is used to guarantee that all molecules with transition dipole moments at different angles have an equal chance to get excited so that the final polarization distribution was not biased. For anisotropy ensemble measurements, a linearly polarized light was used so that molecules with transition dipole moment aligned with the excitation polarization were preferentially excited.

The circularly or linearly polarized light is passed through the neutral density filters which allow us to adjust the power of excitation light to meet the need of different samples. Afterwards, the laser light is converged into a single-mode optical fiber by a 10× objective. The single-mode fiber transfers the light and meanwhile serves as a 3.3 μm diameter spatial filter. The laser light coming out of the other end of the single-mode fiber is then

collimated by a 10× objective and directed to an inverted microscope by a reflecting mirror. Inside the microscope, the laser passes through an interference filter, is reflected by a dichroic beamsplitter (Chroma Technology), and finally is focused onto a diffraction-limited spot on the sample by a 100×, 1.25 N.A., oil immersion objective (Nikon, CFI Achroma). The objective tightly focuses the laser beam into a diffraction-limited spot, so called the Airy disk. The size of the Airy disk on the image plane depends on the wavelength (λ) of the excitation light and the numerical aperture (*N.A.*) of the objective lens. The objective determines the resolution (*R*) of this microscope to be about half of the wavelength used, according to the equation[1] $R = 0.61\lambda / N.A.$.

2.3 The nano-positioning sample stage

The sample, usually loaded on a clean cover glass or in a solution chamber with one cover glass attached at the bottom, is placed on the nano-positioning stage that is mounted at the focal plane of the microscope objective. The nano-positioning stage contains positional feedback electronics (Melles Griot "NanoBlock"), which facilitate raster scanning of an area of $10 \times 10\ \mu m^2$ of the sample and allow the molecules to relocate to the objective focal point for fluorescence measurements.

2.4 The emission beam pathway

Upon excitation, fluorescence from the sample is collected by the same objective, passes through the dichroic beamsplitter (Chroma Technology), and is directed out from a

microscope side port. A 100 μm pinhole is placed at the first image plane, which is used to eliminate the out-of-focus fluorescence. The diverging fluorescence from the pinhole is then collimated by an achromatic lens, passes through a notch filter (Kaiser Optical Systems) and a longpass filter. The notch filter is used to eliminate residual laser excitation, and the long-pass filter is used to eliminate scattered laser light. For fluorescence polarization measurements (fluorescence polarization, anisotropy, and modulation), the fluorescence is passed through a polarizing beamsplitter cube, which resolves the fluorescence into two orthogonal components, a parallel polarization component (I_{II}) and a perpendicular polarization component ($I_{\perp}$).

2.5 The detectors

The two fluorescence polarization components are each coupled into their own multiple-mode fibers by achromatic lenses. The resolved fluorescence signals are then detected by two avalanche photodiode (APD) detectors (Perkin Elmer, SPCM-AQR). Upon raster scanning of the sample, each APD detector would produce a fluorescence image from the same area with the respective fluorescence polarization. The size of each fluorescence image was maintained at 10 μm × 10 μm throughout the entire investigation. To examine the photophysical properties, one single molecule, liposome, or cell is chosen from the fluorescence image and relocated to the laser focus by the nano-positioning stage. The fluorescence trajectory of the molecule, liposome, or cell is then collected by the two detectors at a 50 ms dwell time upon continuous laser excitation.

2.6 The computer program

Both the nano-positioning electronics and APD detector signals are controlled through a LabVIEW software installed in the computer.

2.7 Polarization alignment

For bulk anisotropy measurement of single liposomes and single cells, in addition to the use of a quarter-wave plate, a half-wave plate was placed into the excitation pathway, at the second end of the single-mode optical fiber after the achromatic lens. A simplified instrument set-up for anisotropy measurements is shown in Figure 2.2. The quarter-wave plate was used to correct for birefringence caused by various optical components and ensure that a linear excitation polarization was obtained. The half-wave plate was used to align the direction of the excitation polarization to the detectors so that one detector recorded the fluorescence component parallel to the laser excitation and the other detector recorded the fluorescence component perpendicular to the laser excitation.

Polarization alignment included two steps. The first step was to obtain a linearly polarized excitation light. After the laser power at the nanostage was measured and recorded, a polarizer was temporarily inserted at the position of the half-wave plate (position 5, as shown in the diagram). Both the polarizer and the quarter-wave plate were rotated until the maximum power was obtained at one polarizer angle and the minimum power was obtained by rotating the polarizer 90 degrees from the previous one.

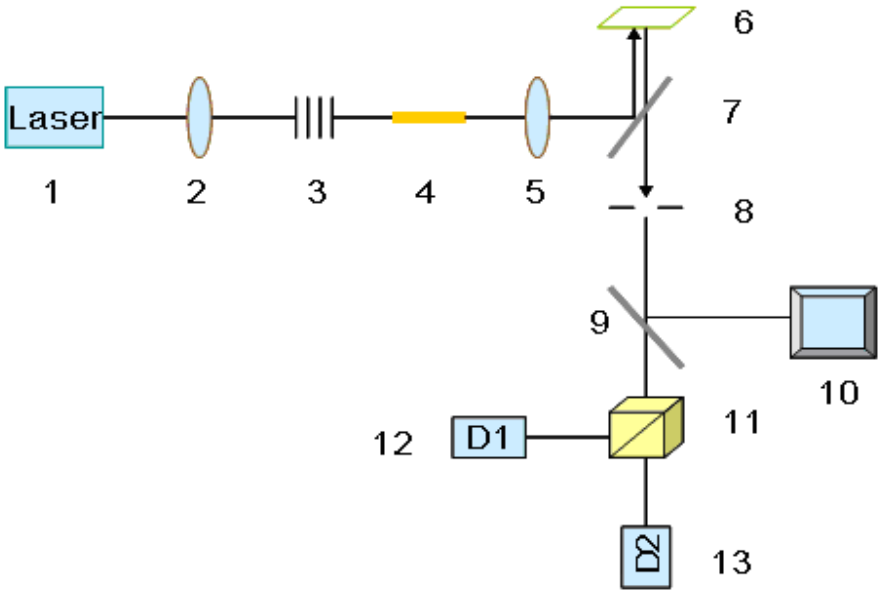

Figure 2.2 Confocal fluorescence polarization microscope setup.

1. Ar ion laser; 2. Quarter-wave plate; 3. Neutral density filters; 4. Single-mode optical fiber; 5. Half-wave plate; 6. Nano-positioning sample stage; 7. Dichroic mirror; 8. Pinhole; 9. Reflection mirror; 10. Monitor; 11. polarizing beamsplitter; 12. APD detector; 13. APD detector.

The second step was to adjust the direction of the polarized excitation. The polarizer was removed and a half-wave plate was placed at the same place as that of the polarizer (position 5, as shown in the diagram). Before adjusting the half-wave plate, a cover glass coated with a FL alcogel thin film was placed on the sample stage. According to the literature, FL in the alcogel thin film is mostly immobilized. When the linearly polarized light shines on the immobilized FL molecules, molecules with the transition dipole moment parallel to the electric field of the excitation light are preferentially excited, leading to large I_{II} intensity and small $I_{\perp}$ intensity. We adjusted the half-wave plate

angle to align the direction of the excitation polarization so that one detector collects I_{II} and the other collects $I_{\perp}$. The half-wave plate angle was rotated from 0 degrees to 90 degrees at an interval of 5 degrees. The fluorescence intensity modulation curve as a function of half-wave plate angle for both detectors was plotted. The half-wave plate was set at the angle that one detector was at the maximum intensity and the other was at the minimum intensity.

For example, in one of our many alignments, the quarter-wave plate was set at 115 degrees to obtain a linearly polarized excitation. The half-wave plate was rotated from 130 to 230 degrees. And the fluorescence modulation curve for both detectors (Figure 2.3A) and the D2/D1 intensity ratio modulation curve (Figure 2.3B) showed that at 145 degrees Detector 2 had the maximum signal while Detector 1 had the minimum, and vice versa at 190 degrees. The quarter-wave plate was set at 145 degrees, which meant that D2 was assigned to the parallel component (I_{II}) and D1 to the perpendicular component ($I_{\perp}$).

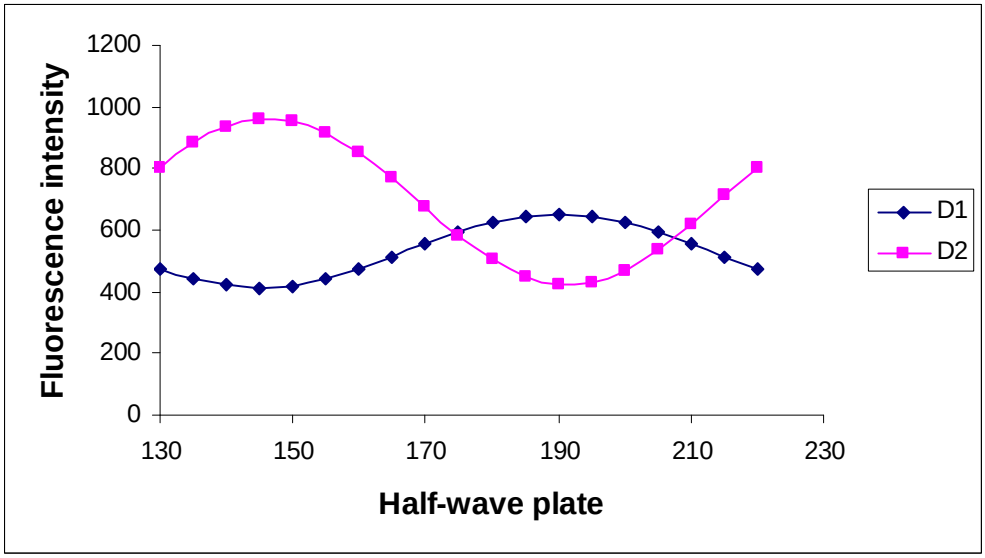

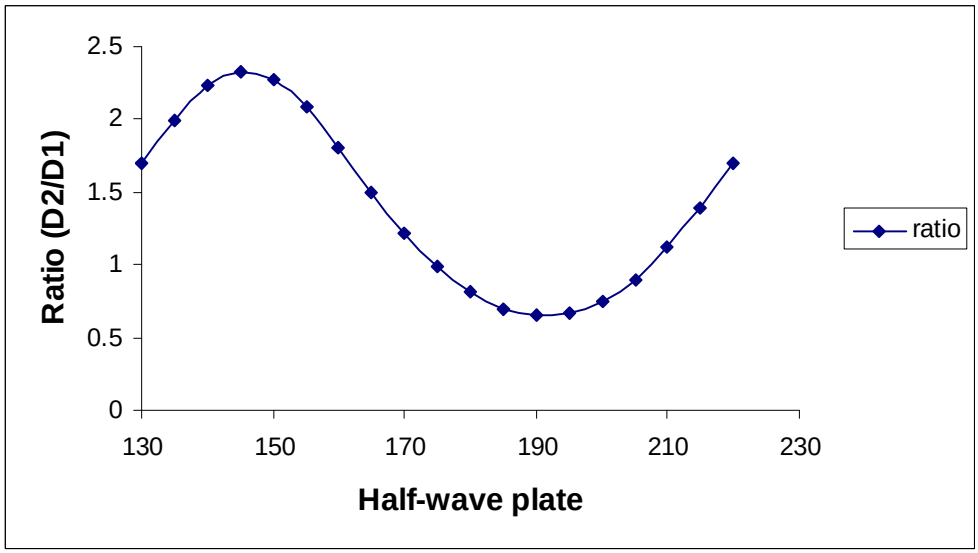

Figure 2.3 Modulation curves of FL molecules inside the alcogel thin film.
A. Modulation of the fluorescence intensity from two detectors
B. Modulation of the fluorescence intensity ratio of the two detectors

Chapter 2 Reference

(1) Huang, B.; Bates, M.; Zhuang, X. *Annu. Rev. Biochem.* **2009**, *78*, 993.

Chapter 3: Balance between Coulombic Interactions and Physical Confinement in Silica Hydrogel Encapsulation

3.1 Introduction

The sol-gel process is a wet chemical technique well suited for the encapsulation of a variety of molecules. The silica sol-gel process [1-4] is usually performed at room temperature using silica alkoxides, such as tetramethyl orthosilicate (TMOS) and tetraethyl orthosilicate (TEOS), as the precursor materials. Two reactions can be used to summarize this process, as shown in Scheme 3.1. First, in the presence of water, silicon alkoxide is hydrolyzed into silanol. This step is usually catalyzed by an acid (HCl) or a base (NaOH). Second, the silanol undergoes polycondensation with one another randomly, forming a porous, three-dimensional sol-gel framework of polymeric silicon oxides.

Scheme 3.1. Sol-gel Process

$$Si(OR)_4 + 4H_2O \xrightarrow{\text{hydrolysis}} Si(OH)_4 + 4ROH$$

$$\equiv Si\text{-}OH + OH\text{-}Si \equiv \xrightarrow{\text{poly-condensation}} \equiv Si\text{-}O\text{-}Si \equiv + H_2O$$

The silica sol-gel is called “alcogel” or “hydrogel” according to the preparation solvent used[5]. A silica alcogel is formed when alcohol is used as co-solvent and there is a high percentage of alcohol in the sol-gel whereas a silica hydrogel is formed when water is used as solvent and there is a high percentage of water in the sol-gel.

Sol-gel process has many advantages such as simplicity, low temperature, low cost, and versatility. Its product, the sol-gel network, also has many advantages, for instance, (i) the porous nature allows the trapping of many guest molecules, inorganic, organic, and biological, into the matrix; (ii) the entrapped guest molecules can retain their functional characteristics to a large extent inside the matrix; (iii) it also allows small-molecule reagents to diffuse through and interact with the guest molecules while they are physically trapped inside the matrix; (iv) the transparency of the matrix enables us to use optical spectroscopic methods to investigate the physical and chemical properties of the entrapped components.

The incorporation of biomolecules into porous silica glass has become an active research area with most interest in biosensors development [6-11]. Sol-gel networks are ideal candidates as hosts for biological molecules because, in addition to those advantages mentioned above, they are synthesized at room temperatures and under fairly mild reaction conditions; and the pores of water-filled gels provide an aqueous environment necessary for biological molecules to function. It was reported that biological molecules trapped inside are able to retain their activity and can even be protected from degradation and thermal denaturation [6]. To date, biological molecules including enzymes and other proteins [7,12-15], antibodies [16], DNA[17,18], and whole cells[19,20] have been encapsulated and studied.

For sol-gel encapsulation applications, the guest–host interactions (interactions between entrapped molecules and the sol-gel) are important issues that need to be

considered in examining the performance of entrapped molecules. Electrostatic interaction is one of the most important guest-host interactions for molecules' adsorption on the silica surface. Under physiological conditions, the silica surface (isoelectric point *pI* = 2.0) is negatively charged, which attract positively-charged small organic dyes like R6G and large biomolecules through electrostatic interaction. While allowing adsorption of guest molecules onto the surface, electrostatic interactions at the same time affect the mobility of the entrapped molecules. Physical confinement, a force imposed by the silica sol-gel structure onto entrapped molecules, can alter the confined molecule's behavior. Not only can it restrict the motion of a guest molecule directly but also it can modify the dynamic and thermodynamic properties of the confined fluid [21,22] thereby to control the structure, function, and dynamics of the guest molecule. Dopants, on the other hand, can impose a "molecular templating" effect onto the sol-gel network, directing the pore formation during gelation of the silica sol [23]. The sol-gel network therefore carries the structural characteristics of the entrapped molecules, which can be used to create artificial receptors for molecular recognition (a technique called molecular imprinting). In addition to these major forces, shorter range interactions such as H-bonding, hydrophobic interaction, and van der Waals force, might also affect dopants' mobility. Obviously, the different behavior of guest molecules inside the sol-gel matrix depends on a balance of all the forces they encounter.

Though the importance of guest-host interactions has been realized, not much is known about how they influence the physical and chemical properties of encapsulated

biological molecules. Due to diversities in the entrapped molecules as well as the sol-gel matrix, answers to these questions may vary from one application to another: what kind of interactions it may have between the guest and host, how important they are compared to each other, how do they balance to contribute to such behavior, which one dominates among all these interactions? Once the answers to these questions become clear, understanding and even controlling the behavior of the dopants will be much easier.

Previous work in our lab was focused on studying the effects of charge-charge interactions, hydrogen bonding, and solvation effects on the rotational mobility inside silica alcogels. The study of a variety of dyes demonstrated that none of these control the mobility of entrapped molecules inside the alcogel, rather, mobility is largely controlled by the physical confinement imposed by the small silica pores. From other groups' research, the positive charged dye molecules (R6G) were demonstrated to exhibit high fluorescence anisotropy when bound to silica particles[24]. On the other hand, R6G molecules were also able to diffuse on a humid silica surface[25] and on silica films[26], which together suggested that Coulombic interaction is not sufficient for complete immobilization of R6G. As for anionic dyes, such as pyranine and fluorescein, they were reported to display much higher mobility (rotation and translation) compared to cationic dyes in a hydrogel□indicating that Coulombic interaction may dominate the mobility. Collectively, these imply that Coulombic interaction and physical confinement could be leading candidates that control the mobility inside the sol-gel network.

In this project, we investigated the leading factor that controls the molecular mobility

inside a silica hydrogel using the Cationic R6G and anionic FL. R6G and FL were chosen in view of their similar molecular structures, so that any difference in their behavior could be confidently attributed to their opposite molecular charges. Meanwhile, the green fluorescence protein, GFP, was used to examine the effect of molecular templating on mobility. The hydrogel with much larger pore size and rich in aqueous solution was constructed in favor of biomolecules encapsulation. Tetramethyl orthosilicate (TMOS) was used as the hydrogel precursor. Called biogel, TMOS hydrogel is more environmentally compatible with biomolecules as its by-product, methanol, has less denaturing activity on the entrapped biological moiety than the by-product of TEOS, ethanol[6].

For macromolecules like proteins, it is very possible that even the large pores in a hydrogel may not be big enough to completely eliminate molecular templating, which may cause a negative effect on the activity of a silica based biocomposite material. Fluorescence anisotropy studies on dye-labeled proteins reveal that the encapsulated protein (bovine and human serum albumin) can retain a considerable amount of rotational mobility in a hydrogel, implying that these proteins are not severely constrained inside a hydrogel[27]. However, the rotational freedom associated with the covalent linkage between the dye and the protein makes these measurements less conclusive.

The auto-fluorescent green fluorescent protein (GFP) is an ideal probe for examining the mobility of an encapsulated protein. The fluorophore of GFP is permanently locked into a fixed orientation with respect to the protein itself. As a result, fluorescence

anisotropy measurements on GFP should eliminate any uncertainty due to rotation about a single bond and truly reflect the rotational mobility of the protein. GFP has been found mostly immobilized in small silica pores in hydrogel with high silica content [28,29]. However, it is not known if the same holds true in a hydrogel that constitutes of substantially bigger silica pores, like the one we prepared.

In this study, the mobility of R6G, FL, and GFP was compared using single molecule spectroscopy. The translational diffusion of FL within the hydrogel was monitored by fluorescence recovery after photobleaching, Hydrogel encapsulated R6G was subjected to low pH and high salt conditions and the change in fluorescence anisotropy in R6G and FL as the hydrogel solidified was compared in order to gain insight to the placement of R6G in the hydrogel.

3.2 Experimental

3.2.1 Materials

Sol-gel materials including tetramethyl orthosilicate (TMOS) and tetraethyl orthosilicate (TEOS) and fluorescence dyes including rhodamine 6G (R6G) and fluorescein (FL) were all purchased from Sigma-Aldrich. The green fluorescence protein, rEGFP, was purchased from BD Biosciences. All reagents were used as received. Microscope cover glasses (Fisher Premium) were purchased from Fisher Scientific and were thoroughly cleaned by consecutive sonication in a 10% sodium hydroxide solution, distilled water, acetone, and deionized water for 1 hour each, respectively, before use.

3.2.2 Hydrogel preparation

A sol solution was firstly prepared by mixing TMOS, H_2O, and HCl (0.01N) with volumes of 562.5, 120, and 11.25 μL, respectively. To facilitate acid hydrolysis, the sol solution was sonicated in an ice bath for half an hour. Trapping of the dye or protein molecules was made before polycondensation of the sol solution. That is, the sol solution was mixed with 10 mM phosphate buffer (pH 7.0) that contained the dyes or the protein encapsulates to facilitate the formation of a gel network. The volume ratio of the sol to the buffer was 1:10. Formation of the hydrogel occurred within half an hour.

A sandwich-structure hydrogel thin film sample was made by first stacking two cover glasses together using double-sided tape as a spacer to form a thin solution chamber. Then a 40 μL sol solution was added to a 400 μL 10 mM phosphate buffer (pH 7.0) that contained either the dye or the protein encapsulates. 40 μL of the sample mixture was then transferred and spread inside the chamber. The opening of the solution chamber was then sealed to prevent the rapid drying of hydrogel after gelation. The sandwich-structured sample was then aged for 12 hours before use.

To prepare a hydrogel monolith, 1100 μL sample mixture was added to a plastic cuvette (1.5 mL), and the cuvette was sealed for gelation.

3.2.3 Single molecule polarization

We used fluorescence polarization to study single dye and protein molecules to compare their mobility inside the silica hydrogel matrix. Single GFP and FL molecules

were studied using 488 nm laser excitation while R6G was studied using 514 nm laser excitation. The circularly polarized excitation light was used such that all molecules have an equal opportunity to be excited regardless of the orientation of their transition dipole moments. Time dependent polarization of a single molecule was calculated according to Eq. 3.1

$$P(t) = \frac{I_{II}(t) - G \cdot I_{\perp}(t)}{I_{II}(t) + G \cdot I_{\perp}(t)} \qquad (3.1)$$

where *P(t)* is time-dependent anisotropy, and I_{II} and $I_{\perp}$ are the fluorescence intensity that are parallel with and perpendicular to the excitation polarization, respectively. *G* is a correction factor used to correct for bias between I_{II} and $I_{\perp}$ due to variances in detectors' alignment and sensitivity as well as optical birefringence. The *G* factor was daily calculated using free dye solution by forcing the average anisotropic value ($\overline{P}$) of the isotropic dye solution to be zero.

To compare the mobility of molecules, the $\overline{P}$ of each molecule was calculated, together with its standard deviation σ. A molecule was classified as 'tumbling' when the $\overline{P}$ of this molecule fell within the range of the standard deviation of the isotropic dye solution ($\pm\sigma_{iso}$). A molecule with its $\overline{P}$ outside the range of $\pm\sigma_{iso}$ was classified as 'fixed'. A third kind of molecule belongs to those whose time-dependent polarizations vary dramatically and therefore have a big σ. Such molecules were classified as 'intermediate', since their behavior was between "tumbling" and "fixed". Because our classification scheme could not differentiate a tumbling molecule from a fixed molecule

that lies 45 degrees between the parallel and perpendicular axes, the number of tumbling molecules reported using this method should be regarded as an upper limit.

3.2.4 Fluorescence recovery after photobleaching (FRAP)

FRAP of FL in hydrogel was performed using the confocal microscope as mentioned in chapter 2. A spot on the sample was chosen and was moved to the laser focus. A probe laser light was used to obtain stable, initial fluorescence intensity first. The laser power was then increased by 10,000 fold to photobleach the molecules for 10 seconds. Immediately after photobleaching, the power was decreased back to the probe level again to begin monitoring the recovery of fluorescence due to diffusion of FL from adjacent areas into the bleached region. The fluorescence immediately after photobleaching would drop to its lowest intensity (F_0). The experiment was stopped when the fluorescence recovery reached a plateau (F_∞). The procedure was repeated 5 times to obtain FRAP data at other areas. For comparison, FRAP of FL in solution was also studied. The FRAP data (fluorescence intensity *vs.* time) were fit using the following equation,

$$I(t) = A_1(1-\exp(-k_1 t)) + A_2(1-\exp(-k_2 t)) + C \qquad (3.2)$$

where $I(t)$ is the fluorescence intensity, k_1 *and* k_2 are the recovery rate constants, A_1 and A_2 together are the difference between the final plateau intensity and the initial intensity after photobleaching (F_∞ - F_0). Separately, A_1 and A_2 are the portions that contribute to k_1 *and* k_2, respectively. C is F_0.

3.2.5 Steady-state fluorescence anisotropy

Bulk fluorescence anisotropy measurements were performed using a Shimadzu RF-3101PC fluorometer in order to study the mobility of dyes entrapped inside hydrogel monoliths. Spectra were recorded at λ_{ex} = 488 nm for FL and GFP and λ_{ex} = 514 nm for R6G. To determine steady-state fluorescence anisotropy λ_{em} = 509 nm, 513 nm, and 551 nm were used for GFP, FL, and R6G, respectively. All fluorescence anisotropy values were calculated based on the following equations,

$$r = \left(I_{VV} - GI_{VH}\right)/\left(I_{VV} + 2GI_{VH}\right) \qquad (3.3)$$

$$G = I_{HV}/I_{HH} \qquad (3.4)$$

where r is the anisotropy, and G is a correction factor used to correct any polarization bias in the fluorometer. I_{VV}, $I_{VH,}$ I_{HH}, and I_{HV} are the fluorescence intensities measured with different polarized excitation and emission schemes. For example, I_{VV} is the fluorescence intensity with vertically polarized excitation and vertically polarized emission whereas I_{VH} is the fluorescence intensity with vertically polarized excitation and horizontally polarized emission.

The R6G anisotropy as a function of the pH of the silica hydrogel monolith was investigated over a 3-month period. To change the acidity of the hydrogel matrix, a 100-300 μL aliquot of HCl solution at pH 2.0 was added to the top of a R6G-encapsulated hydrogel monolith and allowed to equilibrate for at least one week before the anisotropy was measured again. The pH of the monolith was then tested by measuring the pH of the solution on top of it. During the 3-month period, the pH of the hydrogel monolith was gradually brought down from 7.0 to 3.5. In a separated experiment, NaCl was introduced

to the hydrogel in an attempt to weaken the Coulombic attraction between R6G and the hydrogel. A 300 μL aliquot of 1M NaCl was added to the top of a R6G-encapsulated hydrogel monolith and allowed to equilibrate for two weeks before the anisotropy of R6G was measured again.

To investigate the time evolution of fluorescence anisotropy of FL and R6G during hydrogel formation, 100 μL liquid TMOS sol and 1 mL buffer solution containing 10^{-6} M dye was added to a 1.5 mL cuvette. Before the experiments, a *G* factor was first measured by recording the I_{HV} and I_{HH} from a 10^{-6} M R6G solution. Monitoring the fluorescence intensity in real time was started 15 seconds after the dye-containing buffer was mixed with the TMOS sol and lasted for approximately 30 minutes. The fluorescence anisotropy evolution as a function of time was plotted. The data was fit according to the following equation,

$$r(t) = A\exp(-k_{\text{aniso}}t) + C \quad (3.5)$$

where A is the change of anisotropy during the gelation process from 15 seconds to 30 minutes, k_{aniso} is the rate of change of anisotropy, and C is the initial anisotropy.

3.3 Results and Discussions

3.3.1 Structure and spectra characteristics of GFP, R6G, and FL

As shown in Figure 3.1, R6G and FL are both xanthene dyes. They show similar size, shape, and mass (see Table 3.1). The most difference between them is the opposite charge they have, that is, under neutral pH condition, R6G (pKa = 11) carries a positive charge

whereas the relatively smaller FL (pK_{H3FL} = 2.2, pK_{H2FL} = 4.4, pK_{HFL} = 6.4) carries at least two negative charges[30]. The fluorescence spectra of R6G and FL solution used in this research show that R6G has the maximum excitation and emission at 530 nm and 551 nm, respectively, whereas for FL the maximum excitation and emission are at 493 nm and 514 nm, respectively (see Figure 3.2 and Table 3.1).

GFP is much larger (27 kD and 239 amino acids) in size compared to R6G and FL. The structure in Figure 3.1 shows that it has a beta-can shape, with 11 antiparallel beta strands forming a very compact cylinder. Inside this cylinder is an alpha-helix, inside the middle of which lies the well-protected chromophore, formed by the cyclization of three amino acid residues Ser65, *dehydro*Tyr66, and Gly67. The cylinder has a diameter of about 30 Å and a length of about 40 Å. The fluorescence spectra of GFP solution used in this research show that, very similar to FL, GFP has the maximum excitation and emission at 493 nm and 510 nm (Figure 3.2 and Table 3.1), respectively. In Table 3.1 it also shows that the isoelectric point (*pI*) of GFP is 5.9, which means that under neutral condition, GFP carries net negative charge(s), which is also similar to FL in this regard.

Structure and Spectra of R6G, FL, and GFP

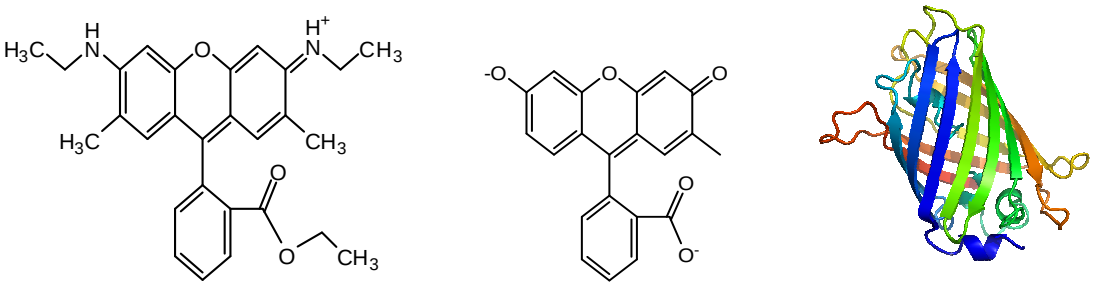

(A) (B) (C)

Figure 3.1 Structures of R6G (A), FL (B), and GFP (C).

(Figure of GFP was from RCSB Protein Data Bank (ID: 3ADF))

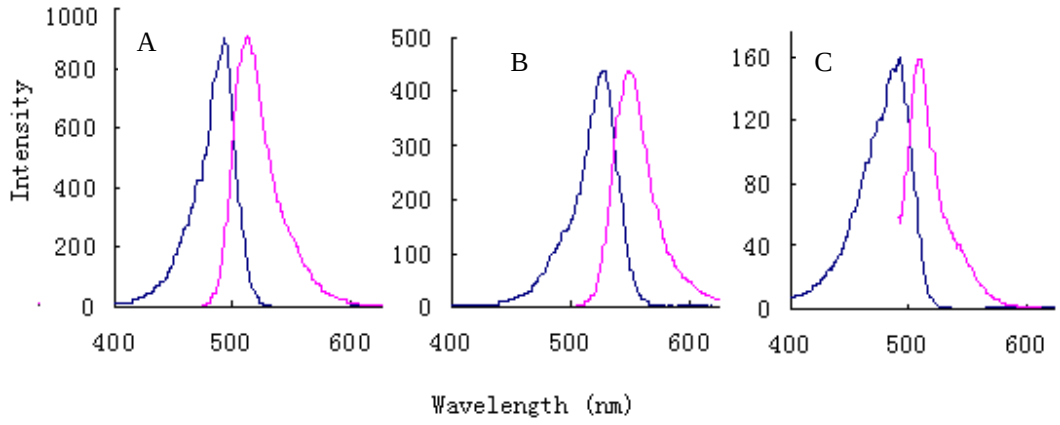

Figure 3.2 Fluorescence excitation and emission spectra of FL (A), R6G (B), and GFP (C).

Table 3.1 Properties of R6G, FL, and GFP

	MW	pI/pKa	Excitation (nm)	Emission (nm)	Em (cm-1M-1)	Quantum Yield (%)
GFP	27,000	5.9	493	510	55,000[31]	0.6[31]
R6G	479	11	530	551	114,000[32]	0.95[33]
FL	332	4.4, 6.4	493	514	92,300[34]	0.97[34]

3.3.2 Single molecule spectroscopy

R6G, FL, and GFP samples were prepared under identical sol-gel conditions (in phosphate buffer at pH7, and sol to buffer ratio (1:10 (v/v), and gelation time of 12 hours, etc). The samples were then scanned using the home-built confocal microscope. Single molecule fluorescence images, shown in Figure 3.3, demonstrate that GFP, FL and GFP experienced different mobility when encapsulated in the silica hydrogel.

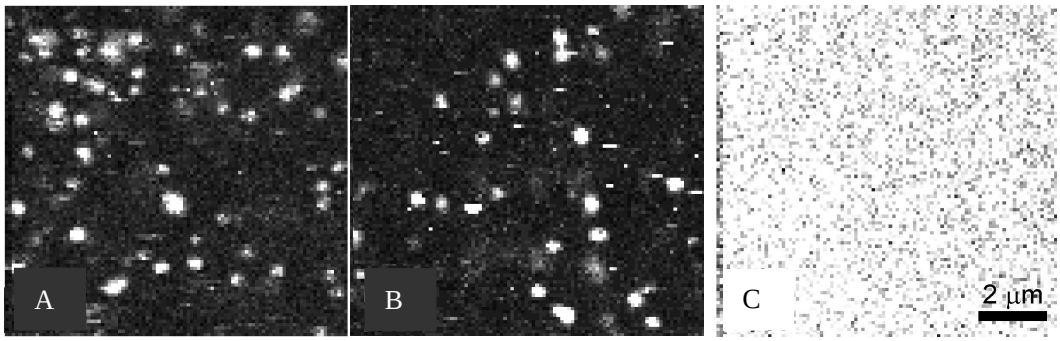

Figure 3.3 Fluorescence images of (A) GFP, (B) R6G, and (C) FL encapsulated in silica hydrogels.

R6G. The R6G image (Figure 3.3B) displays easily discernable, distinct fluorescent spots. The well-defined circular fluorescent spots indicate that many R6G molecules were immobilized in the hydrogel. The non-circular fluorescent spots in the image are probably due to photobleaching or blinking of R6G molecules. The apparent presence of fluorescence streaks in the image suggest that though being immobilized to a great extent, some R6G molecules are still quite mobile in the hydrogel[35].

R6G molecules have been shown to be mostly immobilized when encapsulated inside

silica alcogel [3], but diffuse quite freely with a diffusion coefficient of 4.89×10^{-7} cm^2/s within the mesoporous glass [26]. As demonstrated recently, a thin layer of absorbed water is known to facilitate R6G diffusion on glass surfaces[25]. With a more porous silica framework practically filled with water, the hydrogel employed in this study is expected to allow substantial R6G diffusion. Instead, the vast number of fluorescent spots relative to the very few number of fluorescence streaks in the image suggests otherwise, indicating that despite the small molecular size and the moderate solubility of R6G in water, the majority of R6G was immobilized in the extremely porous hydrogel. Strong Coulombic attraction between cationic dyes and silica surface have been demonstrated and utilized to monitor the growth of nanosize silica colloids during the sol-gel formation process[36-42]. In our case, R6G molecules are also attracted to the silica surface through Coulombic interactions, which renders them mostly immobilized despite being trapped inside an extremely porous hydrogel framework. Most recently, time-resolved fluorescence anisotropy measurements on R6G ionically adsorbed on various silica substrates implies that R6G can be rigidly bound to a silica surface via a maximum of four hydrogen bonds[43]. This will further enhance the efficiency of R6G immobilization in our hydrogel, which favors the observation of stationary fluorescence spots in Figure 3.3B.

FL. The FL image (Figure 3.3C), very different from that of R6G, is characterized by a featureless fluorescent background. Neither fluorescent spots nor fluorescence streaks are seen. Any attempt to obtain an image of immobilized FL in the hydrogel by changing FL concentration only resulted in a corresponding change in the featureless fluorescence

background. This implies that FL molecules in hydrogel are too mobile for imaging by raster scanning. Moreover, the absence of distinct fluorescence streak implies that FL diffusion in the hydrogel is considerably faster than that of R6G. A recent report put the diffusion coefficient of FL encapsulated inside a 2-day aged hydrogel with higher silica content at 3.93×10^{-7} cm^2/s[44]. For FL in our freshly prepared hydrogel that contains more than 90% water (≈3.0 wt% SiO_2), diffusion is expected to become even faster.

The completely different diffusion behavior of FL and R6G depicted in Figure 3.3 suggests that the Stokes-Einstein equation alone is no longer an adequate model to describe their diffusion in silica hydrogels. It is influenced by other factors that clearly go beyond the physical dimension of FL and R6G. At a neutral pH, we expect that strong Coulombic attractions of cationic R6G toward negatively charged silica surfaces would severely impair R6G diffusion inside the hydrogel, whereas anionic FL would be sufficiently repelled from the silica surfaces and remains relatively mobile in the solvent phase. FL diffusion would only be weakly hindered by mesopores and channels that make up the hydrogel. Similar observations have been reported from a 3.1 wt% SiO_2 sodium silicate gel where R6G was found to be effectively immobilized while the anionic pyranine dye only experienced a modest drop in mobility[42]. In a previous study, we observed a similar but less dramatic trend in Columbic effect on the mobility of Oregon Green (ORG, a more photostable derivative of FL) and R6G in alcogel thin films, where the silica framework is much more constricted than that of a hydrogel. Both molecules were found to be incapable of translational diffusion in an alcogel, with ORG displaying

only a moderate increase in rotational diffusion after the alcogel was equilibrated with a neutral pH buffer[3,45]. The observation of a significantly bigger contrast in mobility between R6G and FL in the present work suggests that the influence of Coulombic interactions on mobility can be effectively adjusted by controlling the porosity of a silica sol-gel host, with higher porosity favors bigger contribution of Coulombic interactions to mobility. While it is tempting to apply a similar argument to attribute the lack of R6G mobility to Coulombic attraction alone, however, there is evidence from subsequent experiments that physical confinement may also play a significant role in the immobilization of R6G in hydrogel.

Although translational diffusion is prohibited in most silica hydrogel encapsulated R6G molecules, it is still possible to examine their rotational mobility by performing emission polarization measurements on single R6G molecules[46]. The mobility of 296 R6G molecules were classified, and the results are compared to those previously obtained from alcogel encapsulated R6G also shown in Table 1. While the mobility distributions of R6G in hydrogel and dry alcogel do not resemble one another, there is a striking similarity in R6G mobility between those measured from hydrogel and wet alcogel. Both silica gels are dominated by fixed R6G molecules with significantly less contributions from intermediate and then tumbling molecules. This similarity implies that despite the very different structural architecture between silica alcogel and hydrogel, once the more mobile R6G molecules (e.g., those loosely adsorbed on thin film surface) in a dry alcogel are washed off by water, the remaining molecules that left in the wet alcogel are probably residing in

microenvironments that are similar to those surrounding the hydrogel encapsulated R6G molecules. It is known that physical confinement is responsible for the low rotational mobility of R6G in alcogel. A similar microenvironment to the alcogel-encapsulated R6G would suggest that physical confinement may also have a considerable influence on R6G in a solidified hydrogel. On top of physical confinement, it has also been pointed out recently that R6G molecules entrapped inside silica pores of comparable physical dimension are less capable of free rotations because of the formation of multiple hydrogen bonds with the pore surface[43]. The combined effect of physical confinement and hydrogen bonding may help explain why a dramatic increase in the percentage of fixed R6G molecules is observed in both hydrogel and wet alcogel relative to that encapsulated in dry alcogel, regardless of gel architecture.

Table 3.2 Single-molecule mobility distributions of R6G in Silica hydrogel and alcogel

	Fix (%)	Tumbling (%)	Intermediate (%)
hydrogel	77±2	4±1	19±2
wet alcogel	69±3	4±1	27±3
dry alcogel	23±3	2±1	75±3

GFP. Under neutral condition, GFP should carry a net negative charge since the isoelectric point of GFP is at 5.9. The behavior of GFP is therefore expected to be similar to FL, mobile and is therefore featureless in the fluorescence image. Surprisingly, GFP does not behave like FL, but behaves more like R6G: well-defined fluorescence spots from GFP can be clearly seen in Figure 3.3A, indicating that GFP molecules are mostly

immobilized despite the net negative charge. The obviously lower mobility of GFP than that of FL can be attributed to molecular templating effect.

The fluorescence polarization of single molecules was measured in order to compare the mobility of GFP and R6G. As summarized in Table 3.3, 250 GFP and 296 R6G single molecules were classified into three different categories in terms of rotational mobility: fixed, tumbling, and intermediate. Although GFP is much bigger than R6G and is therefore more affected by molecular templating, the smaller %fixed and higher %tumbling molecules found in GFP suggests that GFP molecules are more mobile than R6G molecules. The higher mobility of GFP than that of R6G can be attributed to electrostatic repulsion due to the net negative charge GFP carries. The data also reveals that close to 2/3 of the GFP molecules examined are immobilized. This again suggests that the effect of molecular templating in hydrogel is still significant although the gel framework has been opened up to decreases this effect. Meanwhile, Coulombic attractions between positively charged regions of GFP and the silica surface may also contribute to the low mobility of GFP in the hydrogels.

Table 3.3 Single-molecule mobility distribution of GFP and R6G in silica hydrogels

	Fix (%)	Tumbling (%)	Intermediate(%)	Total molecules
GFP	64±3	11±2	25±3	250
R6G	77±2	4±1	19±2	296

3.3.3 Fluorescence recovery after photobleaching

FL. Figure 3.4A illustrates two fluorescence transients of FL in the hydrogel after

photobleaching, revealing two distinct recovery behaviors. The rapid fluorescence recovery in both transients solidly points to a high FL translational mobility in the hydrogel. The failure of a complete recovery back to its original intensity within the measurement time in one case, despite the high FL mobility, is a vivid reminder of the heterogeneous pore structure inside the hydrogel. The incomplete recovery could be due to the photobleaching of irreplaceable FL that was embedded deep inside the silica matrix of the hydrogel or the photo-depletion of FL inside a big, well-isolated hydrogel domain, within which are mesopores and channels that are large enough to allow FL diffusion to fuel a rapid recovery.

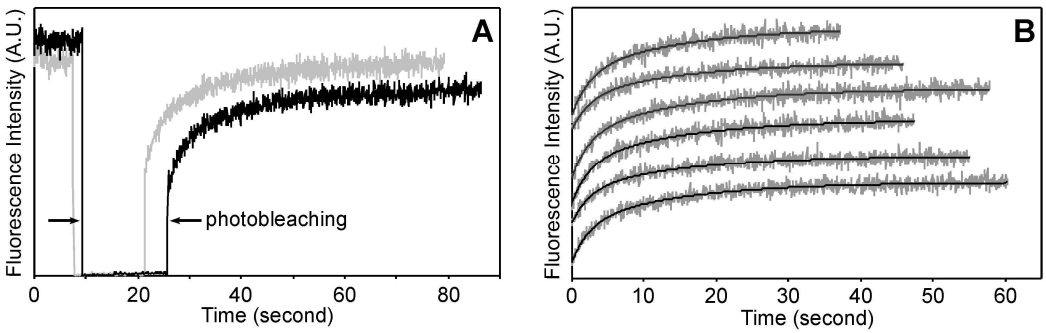

Figure 3.4 Fluorescence recovery traces of FL in hydrogel after photobleaching. (A) An example of full (gray) and partial recovery of fluorescence intensity. (B) The FL fluorescence recovery traces obtained from six separate locations inside a silica hydrogel. The solid curves are obtained from a global fitting to the recovery traces. For illustration purposes, all recovery traces are vertically displayed to remove congestion.

Since the domain is well-isolated from the surrounding hydrogel such that infusion of external FL is either completely excluded or significantly impaired, the dwindling supply

of FL inside the domain would result in a partial fluorescence recovery. If however photobleaching is performed at pore domains where mesopores are connected to the vast hydrogel structure effectively, the continuous supply of FL would make it possible to achieve 100% recovery within the short experimental time frame. Regardless of the final percentage recovery, all transients are characterized by a fast and a slow recovery rate, possibly due to FL traveling through the center and near the surface of silica channels, respectively.

Table 3.4 Fluorescence recovery rate of FL encapsulated in hydrogel and free FL in water

In hydrogel				
A_1 (%)	k_1 (s^{-1})	A_2 (%)	k_2 (s^{-1})	k_{avg} (s^{-1})
46±10	0.23±0.01	54±10	0.01±0.01	0.11±0.01
46±10	0.38±0.01	54±10	0.07±0.01	0.21±0.01
40±10	0.50±0.01	60±10	0.09±0.01	0.25±0.01
46±10	0.42±0.01	54±10	0.07±0.01	0.23±0.01
43±10	0.48±0.01	57±10	0.07±0.01	0.24±0.01
40±10	0.69±0.01	60±10	0.08±0.01	0.33±0.01
In water				
A_1 (%)	k_1 (s^{-1})	A_2 (%)	k_2 (s^{-1})	k_{avg} (s^{-1})
52±10	0.50±0.01	48±10	0.09±0.01	0.30±0.01
29±10	1.12±0.01	71±10	0.15±0.01	0.43±0.01
34±10	0.74±0.01	66±10	0.14±0.01	0.34±0.01
37±10	0.85±0.01	63±10	0.15±0.01	0.41±0.01
26±10	1.35±0.01	74±10	0.17±0.01	0.48±0.01
34±10	1.23±0.01	66±10	0.15±0.01	0.52±0.01

Table 3.4 summarizes the recovery rate extracted from six FRAP curves fit individually. A global fitting of the same six curves (Figure 3.4B) yields 0.069 s^{-1} and

0.411 s^{-1} respectively as the slow and fast rate, which suggests a six-fold decrease in Fl diffusion near a silica surface. With 53% contributed by the slow recovery, this gives an averaged recovery rate of 0.229 s^{-1} in the hydrogel.

When the same FRAP experiment was performed on an aqueous solution of FL near a glass substrate, recovery rates of 0.129 s^{-1} and 0.714 s^{-1} were obtained from a global fit of six recovery curves (Figure 3.5). The faster recovery rates for FL in water as opposed to those in hydrogel indicate that despite constituting more than 90% water, the hydrogel still imposes a considerably drag to FL diffusion. The close to six-fold difference between the fast and the slow rates here again suggests that diffusion near the surface of a glass substrate is responsible for the slower recovery rate. A major difference between the FL recovery curves in water and in hydrogel is that under the same probe laser intensity, all recovery curves in water contain a distinct, gradually declining component, which amounts to a continuous depletion of FL even under the weak probe laser excitation. On the other hand, the recovery curves in hydrogel continue to remain steadily up at the end of every measurement illustrated in Figure 3.4B. The gradual decrease in FL fluorescence intensity in water is attributed to a less photostable FL. Once hydrogel bound and less mobile, FL becomes more photostable because of impaired oxygen diffusion as well as the freezing of dynamic motions that facilitate photodegradation.

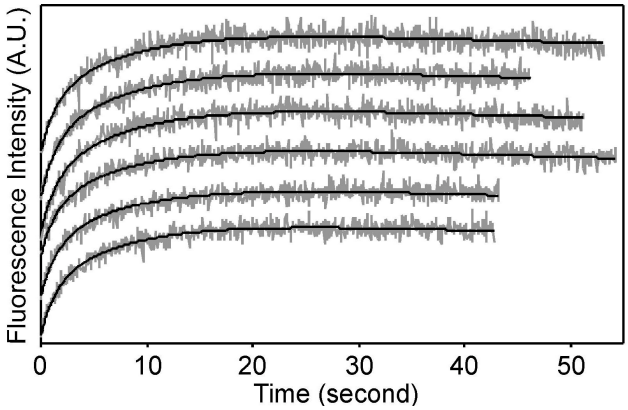

Figure 3.5 Fluorescence recovery traces of FL in water.
The solid curves are the global fitting to the recovery traces collected from six separate locations. For illustration purposes, all recovery traces are vertically displayed.

Using 6.4×10^{-6} cm^2 s^{-1} as the diffusion coefficient of FL in water to relate to the fast 0.714 s^{-1} recovery rate we recorded[47], the diffusion coefficient of FL near the glass substrate would be ca. 1.2×10^{-6} cm^2 s^{-1}, about a factor of five faster than that of R6G[25]. The slower R6G diffusion is attributed to a strong electrostatic attraction between R6G and a silica surface. Based on the same calculation, the averaged diffusion coefficient of FL in our hydrogel was found to be ca. 2.1×10^{-6} cm^2 s^{-1}. This is about five times higher than that obtained from a two-day old hydrogel with a significantly higher silica content and therefore a much denser framework to slow FL diffusion[44]. The diffusion coefficients of FL in hydrogel and in water also indicate, according to the Stokes-Einstein equation, that the viscosity in the hydrogel is approximately 3 times higher than that in water. Our estimate is slightly higher than that reported from a 3.2 wt% sodium silicate hydrogel using time-resolved fluorescence anisotropy (TRFA) measurement on pyranine. In that report □ viscosity was estimated from its effect on rotational diffusion using the

Debye-Stokes-Einstein equation, and was found to be marginally higher in the hydrogel. Collectively, this suggests that while an anionic probe may experience slightly hindered rotation in a hydrogel, its translational diffusion can still be considerably impaired by the hydrogel framework. The discrepancy is attributed to the very different timescales associated with TRFA and FRAP measurements. Fast dynamics like rotational diffusion appears to be less sensitive to the presence of a surrounding silica matrix as long as a guest molecule is residing in large enough silica pores, where the molecule is unlikely to encounter a silica surface within sub-nanosecond timescales. On the other hand, when the relatively slower translational dynamics is considered, numerous collisions between a guest molecule and its surrounding silica matrix could occur in microsecond timescales that are typical of molecular diffusion. Consequently, translational diffusion experiences a more pronounced surface effect than molecular rotation, thereby registering a higher micro-viscosity in the hydrogel.

3.3.4 Steady-state fluorescence anisotropy (r)

Anisotropy of entrapped FL and R6G. The reduction of translational and rotational diffusion is expected to result in a corresponding increase in fluorescence anisotropy of FL and R6G. Table 3.5 compares the steady-state fluorescence anisotropy values of free and hydrogel encapsulated FL and R6G. As expected, R6G registers a bigger increase in *r* value after encapsulation because of a significant loss in mobility. On the other hand, the marginal increase in *r* seen in FL after encapsulation suggests that FL still enjoys a high

degree of freedom in the hydrogel. Both observations are consistent with results obtained from the fluorescence images and FRAP measurements. Since FL and R6G interact differently with hydrogel, the change in *r* observed from FL and R6G here provides a unique opportunity to examine the gelation process of hydrogel from two different perspectives. Particularly, the lack of attraction between FL and silica allow FL to exclusively monitor how viscosity increases as the silica framework buildups during gelation. Whereas the strong attraction between R6G and silica is more suitably used to reveal the grow rate of silica colloids during gelation[48].

Table 3.5 Steady-state fluorescence anisotropy of FL and R6G

	solution	hydrogel	infusion
FL	0.010±0.001	0.022±0.001	0.02
R6G	0.008±0.001	0.325±0.0012	0.18

Infusion of FL and R6G after gelation. Also included in Table 3.5 is the anisotropy values of FL and R6G infused into the hydrogel long after gelation set in. While FL remains free to rotate regardless of when and how it is introduced into the hydrogel, the data from R6G suggest the otherwise. The anisotropy value of infused R6G almost drops by half to 0.18 relative to 0.32 obtained from those introduced into the hydrogel before gelation, implying a higher mobility for the infused R6G. This indicates that the local environment of R6G depends strongly on when R6G is introduced into a hydrogel. Unlike FL, R6G is directed toward a more restrictive environment during the solidification of a

hydrogel. In view of the possible difference between FL and R6G, this alternative placement is most likely related to the opposite charges carried by the two fluorophores.

Evolution of anisotropy during gelation. Figure 3.6 shows the *r* values of FL and R6G as a function of time after adding 10 volume of dye containing buffer to 1 volume of liquid TMOS sol. Both dyes exhibit increasing *r* as gelation proceeded, with R6G displaying a bigger increase relative to that of FL.

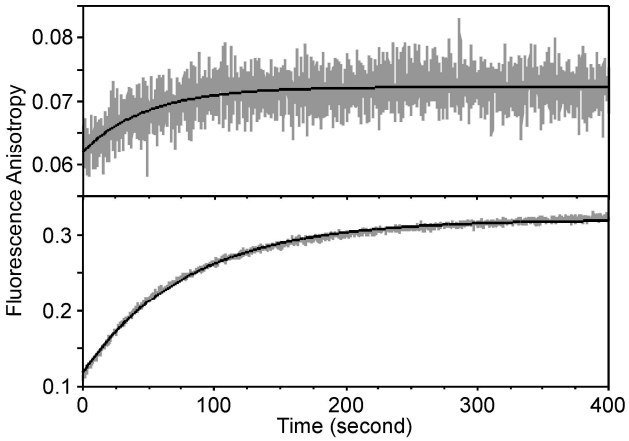

Figure 3.6 Time evolution of fluorescence anisotropy of FL (top) and R6G (bottom)

Despite the very different final r values, FL and R6G produce comparable gelation rates of 0.025 ± 0.004 and 0.012 ± 0.001 s^{-1}, respectively. Although a 2-fold difference between the two rates may imply that the gelation process could be influenced by the nature of the encapsulated probe, this explanation is deemed unlikely as the concentrations of FL and R6G used in these measurements were far below that of the silane precursor used. A more probable explanation is that oppositely charged FL and R6G were encapsulated in different types of local environment and sampling the gelation process therein. Presumably, the faster rate observed in FL indicates that, immediately after mixing, the

viscosity of the sol−buffer mixture increases rapidly. The formation of oligosilane at this early stage of reaction is probably responsible for the increase in viscosity. Unfortunately, FL soon lost the ability to interrogate its local environment after three minutes as the increasing physical confinement imposed by the hydrogel was eventually out-weighed by the strong repulsion between FL and silica. As FL was forced to remain solvated, the minor mobility decrease due to occasional encounters of oligosilane and larger silica colloids could only result in a marginal increase in anisotropy. This continues to be the case through gelation, as the collapsing pores inside the hydrogel were nowhere near the dimension that is small enough to physically impair FL mobility.

In the case of R6G, the much bigger increase in anisotropy (0.306±0.011) suggests that on top of the anticipated higher viscosity, R6G was also drawn to a constricting environment that eluded FL's detection. The influence of this restrictive environment completely overwhelms the viscosity effect and raises the anisotropy of R6G far beyond that viscosity alone can account for. In view of the widely adapted nanoparticle metrology approach, the gradual rise to large anisotropy value can be readily explained by the Coulombic attraction of R6G toward rapidly formed oligosilane, followed by the coalescence of oligosilane to secondary/higher-order particles at a slower rate.

Effect of pH. To determine whether R6G in a hydrogel remains accessible to external stimulants, we tried to exchange encapsulated R6G with H^+ by equilibrating a solidified hydrogel with a pH 2 HCl solution and monitored the change in R6G anisotropy value as the pH of the hydrogel gradually decreased with time. As shown in Figure 3.7, the

anisotropy values of R6G was practically unchanged as the pH of the hydrogel decreased from 7 to 3. This indicates that even as the charges on a silica surface was neutralized at low pH, R6G remained immobilized in a hydrogel and was unavailable for exchange with H^+, hence no change in the anisotropy values. The slowly upward trend in anisotropy value in Figure 3.7 is probably caused by continuous hydrogel aging, which further reduces R6G mobility.

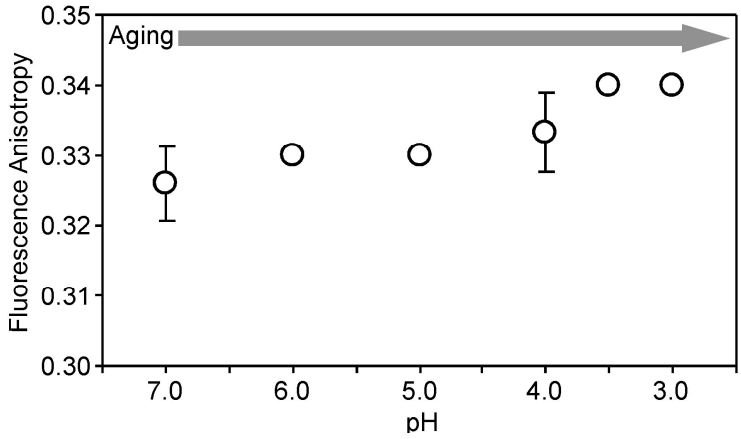

Figure 3.7 Fluorescence anisotropy values of hydrogel encapsulated R6G as the pH of the hydrogel decreases

Effect of salt. We also equilibrated R6G doped hydrogel with a 1 M NaCl solution in an attempt to weaken Coulombic attraction and free R6G from the hydrogel surface to no avail. The anisotropy value of R6G remained unchanged despite extended hours of equilibration.

Collectively, the picture shown in Figure 3.8 describes the encapsulation mechanism of R6G in the silica hydrogel. Once a hydrogel is formed, encapsulated R6G becomes

inaccessible, an outcome that is made possible only if all R6G molecules are permanently embedded inside the silica matrix of a hydrogel. During the early stage of a gelation process, R6G is attached exclusively onto the surface of oligosilane primary particles. However, subsequent coalescence between primary particles as well as continuous polymerization of silanol on primary particles may easily trap those once surface-bound R6G molecules inside secondary/higher order particles. They eventually become molecular templates deeply embedded inside the silica matrix of a hydrogel, displaying highly restrained rotational and translational mobility. This interpretation is also consistent to the observation that R6G infused into a hydrogel exhibits higher mobility compared to R6G that added before the solidification of hydrogel.

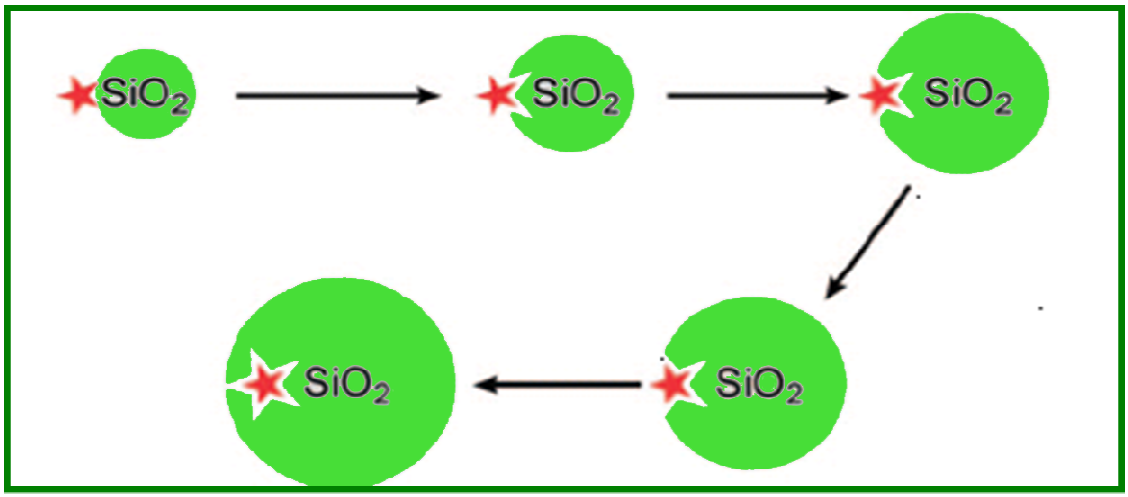

Figure 3.8 Encapsulation model of R6G (star) during hydrogel formation.

3.4 Conclusions

Moving from silica alcogel to the more porous hydrogel, we found that physical confinement become less important and Coulombic interactions become more dominant for small molecules like dyes. While the majority of cationic and anionic dyes are immobilized in alcogel, anionic dyes like FL enjoys a substantial increase in mobility in hydrogel. R6G, however, remains immobilized in hydrogel despite the larger pore size. In view of their similar molecular structures except for molecular charge, we attribute the dramatic difference between the mobility of FL and R6G to Coulombic interactions, with R6G firmly attracted to and FL repelled from silica surfaces at neutral pH. The opposite Coulombic interactions thus cause FL and R6G to reside in different microenvironments within the hydrogel.

The fluorescence image and the fluorescence mobility distribution of single GFP molecules show that GFP is mostly immobilized despite its net negative charge at neutral pH. This indicates that molecular templating still governs the mobility of GFP inside the hydrogel. Compared to FL, the Coulombic repulsion between negatively charged GFP and the silica surface is largely offset by molecular templating, resulting in a much lower mobility. Compared to R6G, GFP does show a slightly higher mobility than the positively charged R6G, regardless of its bigger size. These imply that molecular templating can be influenced by Coulombic interactions, with cationic and anionic templates producing tight and loose silica pores, respectively.

The difference in steady-state anisotropy values for R6G added before and after the solidification of hydrogel helps reveal the influence of Coulombic interactions in the placement of a guest molecule in a hydrogel. The larger anisotropy value for R6G when added before gelation agrees with the notion that R6G binds to oligosilane surface through Coulombic attraction as gelation proceeds. Subsequent coalescence between oligosilane to form secondary/higher order particles then physically trapped the once surface-bound R6G deep inside the resultant silica matrix and trapped in pores templated by the molecules themselves, leading to an additional drop in mobility due to physical confinement. This is consistent to our failed attempts to release the encapsulated R6G with low pH buffers and high ionic strength solutions. On the other hand, R6G that diffuses into a silica matrix after gelation is only attached to a silica surface through Coulombic attraction. The lack of any physical confinement for these R6G molecules results in a smaller anisotropy value relative to those that are physically embedded inside a hydrogel matrix. Collectively, this implies that the extent of physical confinement experienced by a molecule can be influenced by Coulombic interactions during gelation, with cationic and anionic molecules producing tighter and looser encapsulating silica pores correspondingly and therefore leading to stronger and weaker physical confinement effect, respectively.

Chapter 3 References

(1) Dunn, B.; Zink, J. I. *Chem. Mater.* **1997**, *9*, 2280.

(2) Viteri, C. R.; Gilliland, J. W.; Yip, W. T. *J. Am. Chem. Soc.* **2003**, *125*, 1980.

(3) Gilliland, J. W.; Yokoyama, K.; Yip, W. T. *Chem. Mater.* **2004**, *16*, 3949.

(4) Gilliland, J. W.; Yokoyama, K.; Yip, W. T. *J. Phys. Chem. B* **2005**, *109*, 4816.

(5) Quinson, J. F.; Pauthe, M.; Lacroix, M.; Woignier, T.; Phalippou, J.; Hdach, H. *J. Non-Cryst. Solids* **1992**, *147*, 699.

(6) Avnir, D.; Coradin, T.; Lev, O.; Livage, J. *J. Mater. Chem.* **2006**, *16*, 1013.

(7) Pierre, A. C. *Biocatal. Biotransform.* **2004**, *22*, 145

(8) Tess, M. E.; Cox, J. A. *J. Pharm. Biomed. Anal.* **1999**, *19*, 55.

(9) Livage, J.; Coradin, T.; Roux, C. *J Phys-Condens Mat* **2001**, *13*, R673.

(10) Gill, I.; Ballesteros, A. *J. Am. Chem. Soc.* **1998**, *120*, 8587.

(11) Gill, I.; Ballesteros, A. *Trends Biotechnol.* **2000**, *18*, 469.

(12) Diaz, A. N.; Peinado, M. C. R.; Minguez, M. C. T. *Anal. Chim. Acta* **1998**, *363*, 221.

(13) Ellerby, L. M.; Nishida, C. R.; Nishida, F.; Yamanaka, S. A.; Dunn, B.; Valentine, J. S.; Zink, J. I. *Science* **1992**, *255*, 1113.

(14) Smith, K.; Silvernail, N. J.; Rodgers, K. R.; Elgren, T. E.; Castro, M.; Parker, R.

M. *J. Am. Chem. Soc.* **2002**, *124*, 4247.

(15)Braun, S.; Rappoport, S.; Zusman, R.; Avnir, D.; Ottolenghi, M. *Mater. Lett.* **1990**, *10*, 1.

(16)Tan, F.; Yan, F.; Ju, H. X. *Biosens. Bioelectron.* **2007**, *22*, 2945.

(17)Pierre, A.; Bonnet, J.; Vekris, A.; Portier, J. *J Mater Sci Mater Med* **2001**, *12*, 51.

(18)Breadmore, M. C.; Wolfe, K. A.; Arcibal, I. G.; Leung, W. K.; Dickson, D.; Giordano, B. C.; Power, M. E.; Ferrance, J. P.; Feldman, S. H.; Norris, P. M.; Landers, J. P. *Anal. Chem.* **2003**, *75*, 1880.

(19)Premkumar, J. R.; Sagi, E.; Rozen, R.; Belkin, S.; Modestov, A. D.; Lev, O. *Chem. Mater.* **2002**, *14*, 2676.

(20)Nguyen-Ngoc, H.; Tran-Minh, C. *Anal. Chim. Acta* **2007**, *583*, 161.

(21)Gilliland, J. W.; Yokoyama, K.; Yip, W. T. *Chem. Mater.* **2005**, *17*, 6702.

(22)Baumann, R.; Ferrante, C.; Kneuper, E.; Deeg, F.-W.; Brauchle, C. *J. Phys. Chem. A* **2003**, *107*, 2422.

(23)Fireman-Shoresh, S.; Avnir, D.; Marx, S. *Chem. Mater.* **2003**, *15*, 3607.

(24)Tleugabulova, D.; Duft, A. M.; Zhang, Z.; Chen, Y.; Brook, M. A.; Brennan, J. D. *Langmuir* **2004**, *20*, 5924.

(25)Mitani, Y.; Shimada, A.; Koshihara, S.; Fukuhara, K.; Kobayashi, H.; Kotani, M. *Chem. Phys. Lett.* **2006**, *431*, 164.

(26)Mahurin, S. M.; Dai, S.; Barnes, M. D. *J. Phys. Chem. B* **2003**, *107*, 13336.

(27)Jordan, J. D.; Dunbar, R. A.; Bright, F. V. *Anal. Chem.* **1995**, *67*, 2436.

(28) Chirico, G.; Cannone, F.; Diaspro, A.; Campanini, B.; Bettati, S.; Ruotolo, R.; Mozzarelli, A. *Biophys. J.* **2003**, *84*, 163A.

(29) Chirico, G.; Cannone, F.; Beretta, S.; Diaspro, A.; Campanini, B.; Bettati, S.; Ruotolo, R.; Mozzarelli, A. *Protein Sci.* **2002**, *11*, 1152.

(30) Diehl, H.; Horchakmorris, N. *Talanta* **1987**, *34*, 739.

(31) Patterson, G.; Day, R. N.; Piston, D. *J. Cell Sci.* **2001**, *114*, 837.

(32) Du, H.; Fuh, R. C. A.; Li, J. Z.; Corkan, L. A.; Lindsey, J. S. *Photochem. Photobiol.* **1998**, *68*, 141.

(33) Kubin, R. F.; Fletcher, A. N. *J. Lumin.* **1982**, *27*, 455.

(34) Seybold, P. G.; Gouterman, M.; Callis, J. *Photochem. Photobiol.* **1969**, *9*, 229.

(35) Bardo, A. M.; Collinson, M. M.; Higgins, D. A. *Chem. Mater.* **2001**, *13*, 2713.

(36) Geddes, C. D. *J. Fluoresc.* **2002**, *12*, 343.

(37) Geddes, C. D.; Karolin, J.; Birch, D. J. S. *J. Fluoresc.* **2002**, *12*, 113.

(38) Geddes, C. D.; Karolin, J.; Birch, D. J. S. *J. Fluoresc.* **2002**, *12*, 135.

(39) Geddes, C. D.; Karolin, J.; Birch, D. J. S. *J. Phys. Chem. B* **2002**, *106*, 3835.

(40) Birch, D. J. S.; Geddes, C. D. *Phys. Rev. E* **2000**, *62*, 2977.

(41) Geddes, C. D.; Birch, D. J. S. *J. Non-Cryst. Solids* **2000**, *270*, 191.

(42) Tleugabulova, D.; Zhang, Z.; Brennan, J. A. *J. Phys. Chem. B* **2003**, *107*, 10127.

(43) Tleugabulova, D.; Sui, J.; Ayers, P. W.; Brennan, J. D. *J. Phys. Chem. B* **2005**, *109*, 7850.

(44) Hungerford, G.; Rei, A.; Ferreira, M. I. C.; Suhling, K.; Tregidgo, C. *J. Phys. Chem. B* **2007**, *111*, 3558.

(45) Gilliland, J. W.; Yokoyama, K.; Yip, W. T. *J. Phys. Chem. B* **2005**, *109*, 4816.

(46) Viteri, C. R.; Gilliland, J. W.; Yip, W. T. *J. Am. Chem. Soc.* **2003**, *125*, 1980.

(47) Furukawa, R.; Arauzlara, J. L.; Ware, B. R. *Macromolecules* **1991**, *24*, 599.

(48) Tleugabulova, D.; Duft, A. M.; Zhang, Z.; Chen, Y.; Brook, M. A.; Brennan, J. D. *Langmuir* **2004**, *20*, 5924.

Chapter 4: TonB's Motion in the Gram Negative Bacteria *E. Coli*

4.1 Introduction

E. Coli is one of the simplest microorganisms, with a rod shape and a size of 2 μm long and 0.5 μm in diameter. *E. Coli* belongs to gram-negative bacteria because when detected by the Gram's Stain test it does not retain the crystal violet color in their cell wall but stays pink instead. Its envelope consists of two membranes, the outer membrane (OM) and the inner (cytoplasmic) membrane (CM), separated by the aqueous compartment called the periplasm[1]. The OM is an asymmetric lipid bilayer. From the outside to the inside, it consists of lipopolysaccharides (LPS), phospholipids, and peptidoglycan (PG)[2]. The CM is a phospholipids bilayer that is rich in proteins that generate and harvest ion gradients for energy conversion, nutrient transport and other essential processes[3]. The periplasm is a viscous compartment containing a variety of proteins and other materials.

It has been recognized for many years that iron is important for microorganisms. It plays a critical role in microbial growth, metabolism, and interactions with the host. Though iron is known as one of the most abundant elements in the Earth's crust, the concentration of free Fe^{3+} is very limited (10^{-18} M) in the aerobic, neutral-pH environment, due to the very low solubility of $Fe(OH)_3$. This concentration is far below that is required for many microorganisms (10^{-8} M)[4].

To overcome the nutritional limitation for iron, many microorganisms secrete

siderophores into the extracellular environment. These low-molecular-weight chelators can bind strongly and specifically to iron, which is then solubilized and delivered to microbial cells. Most *E. coli* bacteria obtain iron by producing the siderophore enterobactin[5]. Enterobactin has a high affinity with ferric ion, forming FeEnt[6]. As seen in Figure 4.1, Ent contains three catechollate rings that complex Fe^{3+} in a C_3 symmetric structure. When FeEnt is formed, the molecule contains three net negative charges (-3). These net negative charges and the aromatic catecholate groups are believed responsible for the association between FeEnt and FepA, the FeEnt receptor protein.

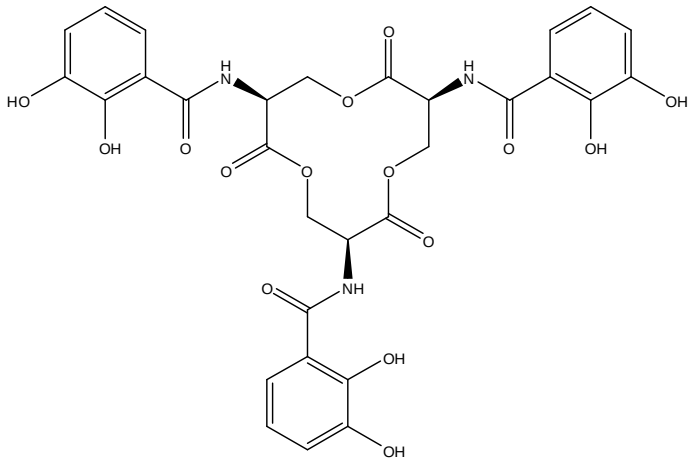

Figure 4.1 Structure of enterobactin

Since FeEnt is too large□726 Da□for the OM pores which allows ~600 Da to pass[7], it is not able to diffuse through. Rather, it has to be actively transported across the OM into the periplasmic space[8]. Active transport of FeEnt into microbial cells includes two stages [5,9]. Figure 4.2 shows all the proteins involved in the two stages and their locations. First, the iron complex is recognized and bound by the receptor proteins sitting in the OM, such

as FepA. Through a not well-understood mechanism, FepA internalizes FeEnt and discharges it into the periplasm. Second, in the periplasmic space, FeEnt binds to its periplasmic binding protein and is then transported across the cytoplasmic membrane into the cytoplasm.

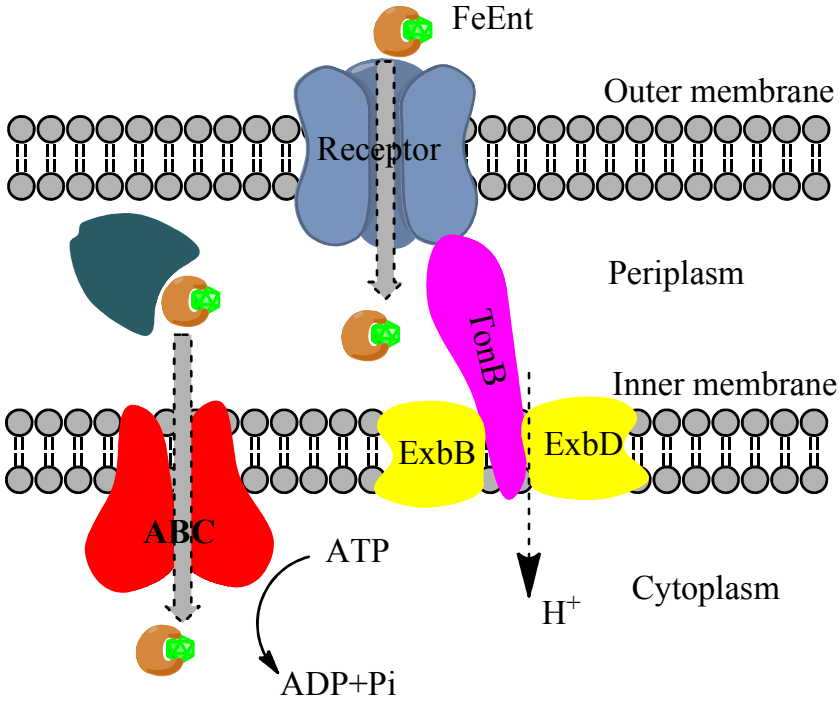

Figure 4.2 Proteins involved in iron transport and their locations

The accomplishment of transporting iron siderophore complex requires energy and TonB, a CM protein[10]. Iron transport from periplasm to cytoplasm is easily energized by ATP through an ATP-transporter system[11]; however, iron transport across OM into periplasm does not have access to ATP. Instead, the cytoplasmic membrane proton motive force (PMF) is utilized as the energy source for this process [12,13]. In a not-well-understood

mechanism, TonB, in the complex with two other cytoplasmic proteins, ExbB and ExbD, couples PMF and transduces energy from the inner membrane to the outer membrane receptor for transport of FeEnt[14].

The inner membrane protein TonB consists of 239 amino acids residues and has a weight of 26 kDa. The TonB sequence can be divided into three functional domains, that is, the N-domain (residues 1-32), the center domain (residues 33-102), and the C-domain (residues 103-239). The hydrophobic N-terminus is anchored to the inner membrane, whose function is to couple the cytoplasmic membrane PMF. The center domain spans about half the distance across the periplasmic space. The C-terminus is believed required for interaction with the OM proteins[15].

The importance of TonB in facilitating iron transport has been well established, however, not much is known about its functional mechanism. Since TonB was first mentioned as energy transducer by Hancock and Braun in 1976[16], many hypotheses and theoretical models have been proposed in an effort to understand the mechanisms of TonB's activities [3,14,17-19]. The models can be classified into two major categories. One, the anchored model, suggests that TonB remains anchored to the cytoplasmic membrane and undergoes conformational change to store and discharge the energy for iron transport [5,9,17,20-22]. The other, the shuttling model, suggests that TonB disengages entirely from the cytoplasmic membrane and associates with the outer membrane. Once the energy has been transduced, TonB repositions within the cytoplasmic membrane, to start the next cycle [14,19]. The shuttling model was refuted in a recent publication by Kaserer et al [17]. The authors

demonstrated that TonB does not need to leave the inner membrane while performing its function. Thus they suggested a membrane surveillance model for TonB' activity. That is, TonB finds occupied receptor proteins by surveying the underside of peptidoglycan-associated outer membrane proteins. Besides the experimental data, the surveillance model finds its rationality from the large stoichiometric difference between TonB and the outer membrane proteins (1:35)[23] that require it for their functions.

Since the surveillance model addressed that TonB is under constant motion in search of iron-bond receptors at the outer membrane, we are interested to know what can be the driving force for such motion and how TonB changes its motion once it finds the target. To find out the answer, we applied fluorescence anisotropy [24] and designed experiments to observe the motions of TonB under different circumstances in living *E. Coli*. An *E. Coli* bacteria construct that expresses GFP genetically fused to the TonB protein (GFP-TonB) was mainly used for this study. Several other *E. Coli* bacteria constructs were also used for control experiments, which include those with GFP expressed in the cytoplasm (cyto-GFP), with fluorescence maleimide (FM) covalently linked to the OM protein FepA (FM-FepA), and with ExbB and ExbD proteins deleted.

The GFP-TonB fusion protein was expressed in wild type *E. Coli* strain BN1071. It was constructed by genetically engineering GFP to the N-terminus of TonB[17]. GFP, as mentioned previously, is a self-fluorescent protein (239 aa and 27 kDa) that is firstly isolated from the jellyfish *Aequoria Victoria*. Its fluorophore, formed by the cyclization of three amino acids (Ser65, Try66 and Gly67), locates at the center of the cylinder-shaped

beta-can[25]. In the bacteria expressing GFP-TonB hybrid protein (which is called GFP-TonB cells for convenience), GFP stayed in the cytoplasm side with its C-terminus linked to the N-terminus of TonB at CM. The GFP-TonB hybrid protein was found to retain TonB's function and GFP's fluorescence.

We monitored the motions of TonB through measurements of anisotropy of GFP-TonB cells. Firstly, to validate our methodology for monitoring the motions of TonB in *E. coli* cells in vivo through observation of GFP, we compared the fluorescence anisotropy of GFP-TonB and cyto-GFP. These two cell constructs had GFP localized differently in the cell and were expected to show different mobility. One with a higher anisotropy reflects a lower mobility. A second experiment was performed to validate our methodology, that is, we compared the fluorescence anisotropy of GFP-TonB and FM-FepA in order to compare their motions. In this case, both the fluorophores and their localizations were different. Subsequently, our focus would be measuring the anisotropy change of GFP-TonB in living *E. Coli* cells in order to understand the role of the energy (PMF) availability on TonB's motions. Three energy inhibitors were used to interrupt PMF, including carbonyl cyanide m-chlorophenyl hydrazone (CCCP), 2,4-dinitrophenol (DNP), and sodium azide. The anisotropy before and after adding the energy inhibitor was measured on a one-cell-per-sample basis. The anisotropy change (the difference between the two anisotropy values) reflected the change in motion of GFP-TonB. That is, a positive anisotropy change showed that motion of GFP-TonB decrease, and vice versa. Additionally, the motions of TonB during iron transport were studied by comparing the

anisotropy before and after adding FeEnt. Finally, to understand the role of the two CM proteins, ExbB and ExbD, on TonB's motion, the anisotropy of GFP-TonB (with ExbB/D) and GFP-TonB-mutant (without the ExbB/D) were compared.

4.2 Experimental

4.2.1 Materials

Two *E. Coli* bacteria strains were used□BN1071 and GUC41, which were used to prepare several *E. Coli* constructs including BN1071/pGT, BN1071/pTpG, BN1071/pFepAS271C, and GUC41/pGT. BN1071/pTpG expresses soluble, cytoplasmic GFP (cyto-GFP) under the control of TonB promoter (for convenience, the cell is also called cyto-GFP). BN1071/pGT expresses (under the same promoter) the GFP-TonB hybrid protein with the GFP linked to the N-terminal of the inner membrane TonB at the cytoplasm side (for convenience, the cell is called GFP-TonB). BN1071/pFepAS271C expresses the outer membrane FepA with Ser deletion and Cys substitution at position 271. For fluorescence labeling, the BN1071/pFepAS271C cell construct is covalently modified with fluorescein maleimide (FM) linked to the side chain of the Cys residue (for convenience, this cell is called FM-FepA). GUC41/pGT expresses the GFP-TonB hybrid protein in the cells that have the ExbB/D inner membrane proteins deleted (for convenience, this cell is called GFP-TonB-Mutant). All cell strains were prepared fresh each day in Dr. Klebba's lab. The energy inhibitors carbonylcyanide m-chlorophenylhydrazone (CCCP) (100 mM in 70% dimethylformamide (DMF)),

dinitrophenol (DNP) (200 mM in DMF), sodium azide (1M in water), and the iron siderophore complex, ferric enterobactin (FeEnt) (100 µM), were prepared in Dr. Klebba's lab.

The fluorescence dye fluorescein (FL) was purchased from Sigma-Aldrich. The green fluorescence protein, rEGFP, was purchased from BD Biosciences. Microscope cover glasses (Fisher Premium) were purchased from Fisher Scientific and were thoroughly cleaned by consecutive sonication in a 10% sodium hydroxide solution, distilled water, acetone, and deionized water for 1 hour each, respectively, before use.

4.2.2 Preparation of samples

A cuvette-coverslip sample chamber was made by gluing the opening side of a cuvette (4.5 mL) onto a clean coverslip using the 5 Minutes Epoxy. The bottom part of the cuvette was cut off to allow loading of the sample solution. To immobilize the bacteria, the cuvette-coverslip sample chamber was first coated with 300 µL (8.33 µg/mL) poly-L-lysine hydrobromide (purchased from Sigma) for at least 15 minutes. After the poly-L-lysine solution was removed, the cuvette was coated with 100 µL cell solution (from Dr. Klebba's lab) and set for at least 15 minutes. The mobile cells together with the residual solution were then removed using a pipette. The sample chamber with the immobilized cells was then rinsed twice with 500 µL phosphate buffer (pH7.0) each. Finally, a 500 µL TBS solution with a small amount of glucose was added to the cell chamber. The glucose was added to energize the cells so that they maintained activity

during the period of measurements.

4.2.3 Real-time fluorescence anisotropy measurements

The fluorescence anisotropy of GFP molecules inside single *E. coli* cells was measured using the home-built fluorescence microscope. The excitation wavelength chosen for these measurements was 488 nm. The instrument was aligned to obtain a linearly polarized excitation light, which allowed one to look at a group of molecules with the same orientation of transition dipole moment. Details about the polarization alignment were described in section 2.7 in Chapter 2.

The sample chamber with immobilized cells at the bottom was placed on the microscope stage. Once the sample settled down on the stage, a fluorescence image was taken. For anisotropy measurements, a single cell from the image was brought to the laser focus by the nano-positioning controlling program. The cell was then exposed to the excitation light for 5 to 10 seconds. Meanwhile, the fluorescence intensity was recorded by two detectors. All fluorescence anisotropy values were calculated on the basis of the following equation:

$$r(t) = \frac{I_{II}(t) - G \cdot I_{\perp}(t)}{I_{II}(t) + 2 \cdot G \cdot I_{\perp}(t)} \qquad (4.1)$$

where r is anisotropy, I_{II} and $I_{\perp}$ are the fluorescence intensities that are parallel with and perpendicular to the excitation polarization, respectively. G is a correction factor used to correct any polarization bias in the microscope. The G factor was calculated daily using FL solution (10^{-5}M) by artificially forcing the anisotropy of this solution to be 0.

4.2.4 Fluorescence recovery after photobleaching (FRAP)

To compare the mobility of GFP-TonB and cyto-GFP, a first kind of FRAP experiments was performed using the same microscope as mentioned above. The cells were imaged using a probe laser light. Following that, a spot (at the corner) of single cells was chosen and was moved to the laser focus by the nano-positioning electronics. The laser power was then increased to photobleach the molecules at that spot. The same was applied to other cells for photobleaching. The sample was then imaged again with the probe laser. The images before and after photobleaching were compared. In a second kind of FRAP experiments, as did in section 3.2.4 in Chapter 3, we monitored the rate of recovery after photobleaching. In experiments here, however, we did not observe a slow recovery in fluorescence intensity. Instead, fluorescence dropped to a lower level and stayed at the same level.

4.3 Results and discussion

4.3.1 Fluorescence images

Figure 4.3 shows that both the GFP-TonB and cyto-GFP cell constructs are rod-shaped, like the wild-type cells, indicating that they retained the same cell morphology with GFP expressed inside. The GFP-TonB and the cyto-GFP cells look similar when viewed at a low intensity scale (Figure 4.3A and 4.3C). However, the difference shows up when the image is viewed at a higher intensity scale: cyto-GFP cells still show homogeneous fluorescence intensity through the whole cell although they all become less bright (Figure

4.3D), whereas GFP-TonB cells (Figure 4.3B) are brighter at the periphery and dimmer in the center. These images agree with the different localization of the GFP molecules inside these two cell constructs. Inside the cyto-GFP cells, GFP molecules locate in the cytoplasm. Since they enjoy more translational diffusion, they are homogeneously distributed through the cytoplasmic space. On the other hand, GFP molecules inside the GFP-TonB cells are attached to the N-terminus of TonB at the cytoplasmic side; therefore, they are distributed close to the cytoplasm membrane.

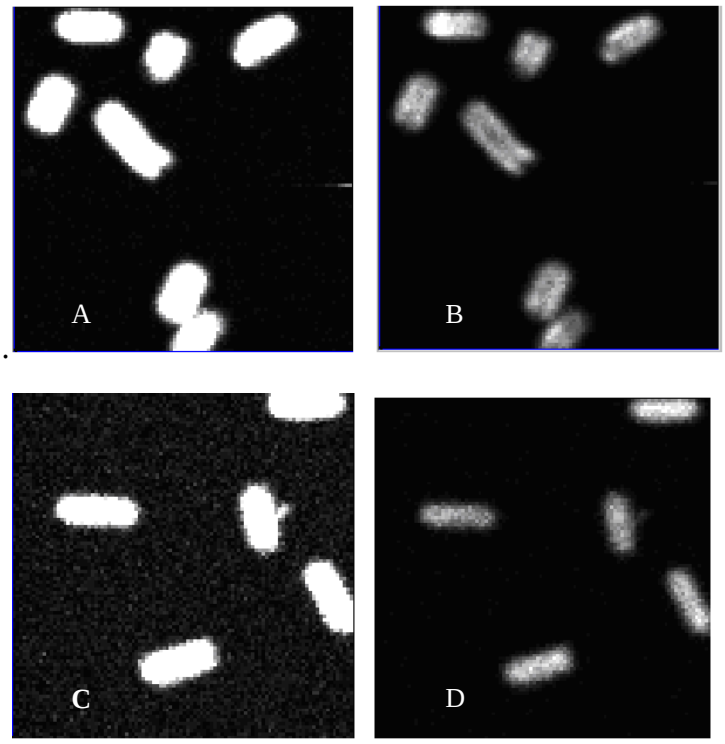

Figure 4.3 Fluorescence images of GFP-TonB and cyto-GFP *E. Coli* cells.
A. GFP-TonB viewed at a low intensity scale; B. GFP-TonB viewed at a high intensity scale; C. cyto-GFP viewed at a low intensity scale; D. cyto-GFP viewed at a high intensity scale.

4.3.2 Fluorescence recovery after photobleaching (FRAP)

Fluorescence photobleaching experiments were performed to compare the

translational diffusion of GFP molecules inside cyto-GFP and GFP-TonB *E. Coli* Cells. The cell sample was first imaged at a probe laser (Figure 4.4A for cyto-GFP and Figure 4.4C for GFP-TonB). Several cells from each image were chosen and were photobleached at the corner for 1 minute by the laser light 100 times higher in intensity than the probe laser. The cells were then imaged again (Figure 4.4B for cyto-GFP and Figure 4.4D for GFP-TonB). It was found that after photobleaching, cyto-GFP cells became less bright but were still homogeneous. As control, two cyto-GFP cells were left un-photobleached. Figure 4.4B shows that the fluorescence image of these two un-photobleached cells remains the same, indicating that instrumental conditions remained the same before and after phobobleaching and that the decrease in fluorescence intensity of other cells were due to photobleaching. For GFP-TonB cells, however, the result was different. After photobleaching, the fluorescence at the photobleached spot of the GFP-TonB cells was almost gone while the un-photobleached area was still as bright as before photobleaching. These experiments demonstrated that GFP in the cytoplasm seemed to enjoy relatively free translational motion whereas GFP-TonB enjoyed less translational motion due to being anchored to the N-terminus of TonB.

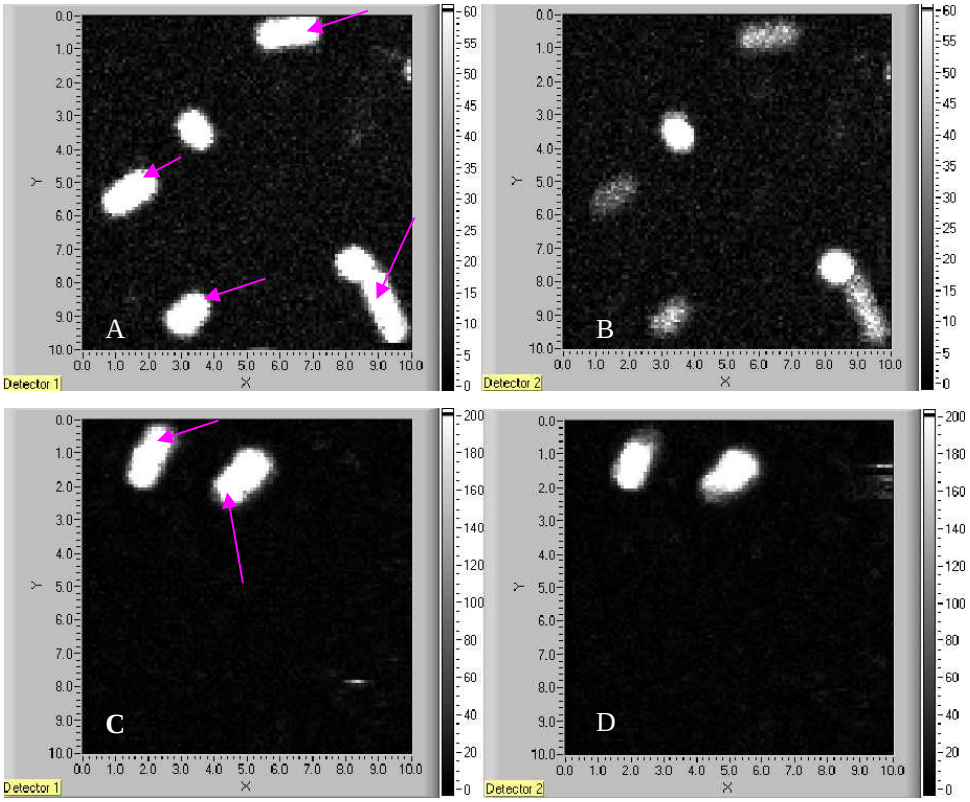

Figure 4.4 Fluorescence images of cells before and after photobleaching.
A. The cyto-GFP cells before photobleaching (the arrows point to the locations that will be photobleached); B. The cyto-GFP cells after photobleaching (the two bright cells in the middle were not photobleached); C. The GFP-TonB cells before photobleaching; D. The GFP-TonB cells after photobleaching (the cell on the left was photobleached at the upper corner, and the cell on the right was photobleached at the bottom corner).

4.3.3 Fluorescence anisotropy measurements by microscopy

In the following paragraphs, we would discuss some instrumental limitations using our method for measuring the anisotropy of single cells. As mention before, the fluorescence anisotropy of the fluorophores in living *E. Coli* cells were measured using a home-built fluorescence microscope. The fluorescence anisotropy, *r*, was calculated according to Eq. 4.1.

$$r(t) = \frac{I_{II}(t) - G \cdot I_{\perp}(t)}{I_{II}(t) + 2 \cdot G \cdot I_{\perp}(t)} \qquad (4.1)$$

where r is anisotropy, I_{II} and $I_{\perp}$ are the fluorescence intensity that is parallel with and perpendicular to the excitation polarization, respectively. G is a correction factor used to correct any polarization bias in the microscope. The G factor was daily calculated using FL solution (10^{-5}M). During the anisotropy measurements, it was found that the experimental conditions, for example, the laser power that reached the microscope stage, the sample's focusing position, the alignment of the laser polarization, and the alignment of the detectors, affected the anisotropy values of *E. coli* cells. The instrumental conditions were subject to change from time to time, which resulted in difficulties in obtaining reproducible anisotropy. In the following paragraphs, we would first focus on investigating the effects of the instrumental conditions on the fluorescence anisotropy measurements of single cells and discuss the possible solutions to such limitations.

4.3.3.1 Effects of the focusing positions on anisotropy values

The G factor, as mention before, was used to correct any polarization bias in the microscope. The G value was obtained by using a FL solution (10^{-5} M): both I_{II} and $I_{\perp}$ of the FL solution were recorded for 10 seconds and G was calculated by forcing the average r value of the solution to be 0. In anisotropy measurements, the laser light was usually focused at the cover glass's upper surface (for convenience, this focus point was called "position 0"), and the G factor at position 0 was then extracted and used for calculation of anisotropy, as shown in Eq. 4.1. The G factor was found very sensitive to changes in the

focus positions of the laser light on the sample. To investigate this effect, the *G* values at 14 different laser focus positions along the vertical direction, z axis, were measured. The focus positions range from z = -1 μm (1 μm below position 0) to z = +30 μm (30 μm above position 0), including z = 0 (position 0). The measurements were repeated for 6 days. The *G* factors as a function of focus positions were plotted, as shown in Figure 4.5. It was found that *G* value decreases significantly from z = -1 μm to about z = +0.5 μm, shown in Figure 4.5 as a steep slope. Afterwards, from about z = +0.5 μm to z = +30 μm, the *G* factor is almost constant. The decreasing trend below z = 0 seems to show that while the focus was moved up and approach 0, less excitation light reflected from the cover glass surface was collected by the objective. The linearly polarized excitation light thus causes less background interference to the emission, resulting in a decrease in *G* factor. Then from z = 0 to further above into the solution, z = +0.5 μm, the further decrease in *G* factor could possibly be explained by the less retardant motion of FL molecules as they are further away from the cover glass surface and become less adhered to the glass surface. In another word, FL molecules at the surface adhere more to the glass surface so that they are less mobile. FL molecules with slower motion give a higher *G* factor. This is because the fluorescence emission of these molecules is less depolarized (the I_{II} to $I_{\perp}$ ratio is bigger), therefore when we force the anisotropy of such molecules to become zero, a bigger *G* has to use to force the numerator of Eq. 4.1, $I_{II}(t) - G \cdot I_{\perp}(t)$, to become 0.

It was also found that the *G* factors measured on different days changed dramatically. For instance, all at position 0, *G* measured on three different days under the same power

and the same polarization alignment is 1.60, 2.03, and 1.35 (the average is 1.66, standard deviation is 0.34), respectively. This is probably because the judgment on whether or not the focus is at 0 is based on what our naked eyes saw, which might be a little bit too arbitrary. When the focus is put at z = 30 μm, where FL molecules are relatively further in the solution, *G* becomes less fluctuated. For instance, all at position 30 μm, *G* measured at the three different days with the same polarization alignment is 1.26, 1.57, and 1.44 (the average is 1.42 and standard deviation is 0.16), respectively.

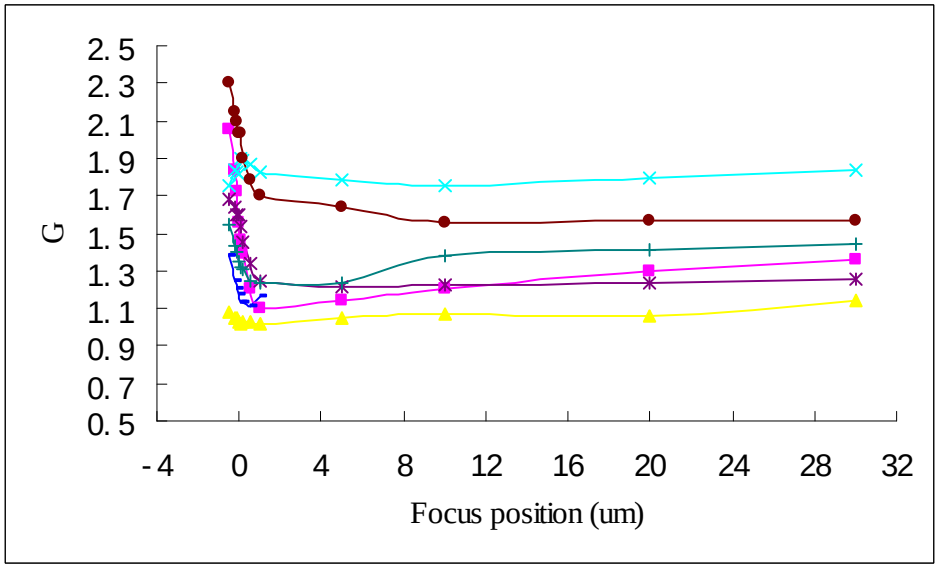

Figure 4.5 *G* factors as a function of focus positions
(Different curves indicate data measured on different days)

As Eq. 4.1 shows, *G* factor affects the magnitude of the *r* value. Since we meant to focus the laser light at position 0 (the upper surface of the coverslip of the sample), we used the *G* factor, obtained by artificially forcing the anisotropy of a FL (10^{-5}M) solution (measured at position 0) to be zero, to calculate the *r* of the sample. However, it happens

that during the anisotropy measurements, when the sample was moved by the nano-positioning electronics to bring the cells to the laser focus one by one, the laser focus might drift slightly away from position 0. As Figure 4.5 shows, *G* is very sensitive around position 0. So even though it is close to position 0, the *G* factor has already changed significantly. Still the *G* factor at position 0 calculated from FL solution was used to calculate the anisotropy. As a result, the *r* value calculated for the sample, through a fixed *G* factor, might not be the actual *r* value of the sample.

In a word, due to the difficulty in focusing the sample exactly at position 0, our method can not provide accurate, absolute *r* values for the cells. Fortunately, we are able to minimize this negative effect to obtain more reliable *r* values by taking the following measures. (1) We decreases the uncertainty in focusing position by adding some immersion oil to the edges of the cover glass to help fix the sample chamber on the sample stage and wait long enough for the sample to settle down before the anisotropy measurements. The sticky immersion oil helps to stabilize the sample, especially to decrease the possible change in focus position caused by raster scanning of the sample. One way to judge whether or not the sample stabilizes on the stage is to check the cell images taken by a Panasonic video camera and viewed through a monitor. It was found that when the sample was just put on the stage, the focus would drift very easily from the original focus point, making the cells blurred in a short period of time. We need to refocus it again and again until the cells shown on the monitor stay solid and firm for a long time, meaning the focus is stabilized. (2) We increase the sample size. A sample size as big as 50

is much better than a smaller sample size as they provide a more reliable statistic average of the anisotropy. More measurements also allow one to build a distribution histogram and check if the data can fit to a Gaussian curve or not, by mean of which one can judge the reliability of the data and find problems easily. (3) As experience found, a better way to focus the laser light is using the cell images at the monitor as a guide, rather than using the excitation light. It is easier to tell whether the cells are on focus or not than to tell whether the laser is on focus or not, although if alignment is done correctly, both focuses should overlap.

4.3.3.2 Effects of polarization alignment on fluorescence anisotropy measurements

The average anisotropy for each cell construct was found different when measured at different periods (the periods are considered different when there is a new polarization alignment between them). For example, the anisotropy of GFP-TonB cells were measured at three different periods and the average anisotropy values were 0.218, 0.173, and 0.255, respectively. This points to another limit of our method in measuring the anisotropy of GFP in *E. Coli* living cells. That is, the average anisotropy measured at different periods, where alignment of the instrument has been changed, varied to some extent. As mentioned previously, the instrument was aligned periodically. The alignment included maximizing laser power at the microscope stage, maximizing the detectors' intensity, checking the quarter-wave plate angle to guarantee that the laser light is still linearly polarized, and checking the half-wave plate angle to ensure that the parallel and perpendicular

components of the emission light are aligned according to the detectors. Details about how the alignment was performed were described in Chapter 2. The anisotropy value relies on the excitation polarization. However, whenever the polarization was realigned, the instrument was never back to the same alignment condition with all the parameters of the instrument kept at the same values. This explained why we were unable to give a reproducible average anisotropy value for the same cell strain measured at different periods. In a word, the change in instrumental alignment causes the anisotropy to change. Fortunately, for the measurements within the same alignment, the average anisotropy was more reproducible even though they were measured on different days. Therefore to avoid the limit caused by the polarization alignment, we tried to finish the measurements within the same day or within a short period of time while the instrumental conditions are the same. And we compared only the results measured within the same period.

The anisotropy can also be affected by the scattering light or background fluorescence. In one of our control experiments, we measured the intensities of the cell strain that did not express GFP. We found that, under the same experimental conditions, the scattering light or the background fluorescence contributed a small portion to the total fluorescence intensity of the cyto-GFP and the GFP-TonB cells. Therefore when the intensity from cyto-GFP and GFP-TonB cells were not high enough, the signal to noise ratio was low and as a result, the *r* value would become unusually large. To avoid this, we would use the cell batch that provides bright enough cells and chose those cells that had similar fluorescence intensity before anisotropy measurements.

4.3.4 Comparison between the anisotropy of GFP-TonB and cyto- GFP in E. Coli cells

In this experiment, we compared the average anisotropy of GFP-TonB with that of cyto-GFP to validate our methodology for observation of GFP in living cells. To measure the anisotropy of single cells, the cells were first immobilized on a cuvette-coverslip sample chamber, and then the sample was placed on the stage of the inverted confocal microscope. When the sample settled down on the stage, a fluorescence image was taken and anisotropy of single *E. Coli* cells from the image was then measured, one by one, by recording the fluorescence intensities of the cells at the center for 5 seconds. The anisotropy of GFP in GFP-TonB and cyto-GFP cells were measured under the same conditions. A sample size of about 50 cells of both GFP-TonB and cyto-GFP were measured. The results showed that: (1) the anisotropy value of single GFP-TonB cells spanned from 0.15 to 0.36, and the average anisotropy was 0.218 (n=53, standard deviation was 0.024); (2) the anisotropy values of single cyto-GFP cells spanned from 0.12 to 0.21, and the average anisotropy was 0.161 (n=51, and standard deviation was 0.015). Figure 4.6 shows the anisotropy distribution of GFP-TonB (A) and cyto-GFP (B) cells. Both curves showed roughly a Gaussian bell shape, with the cyto-GFP curve locating more on the left side of the x-axis that stood for smaller anisotropy. The result showed that GFP-TonB had higher anisotropy values than cyto-GFP, which was consistent with the localizations of GFP in these cells.

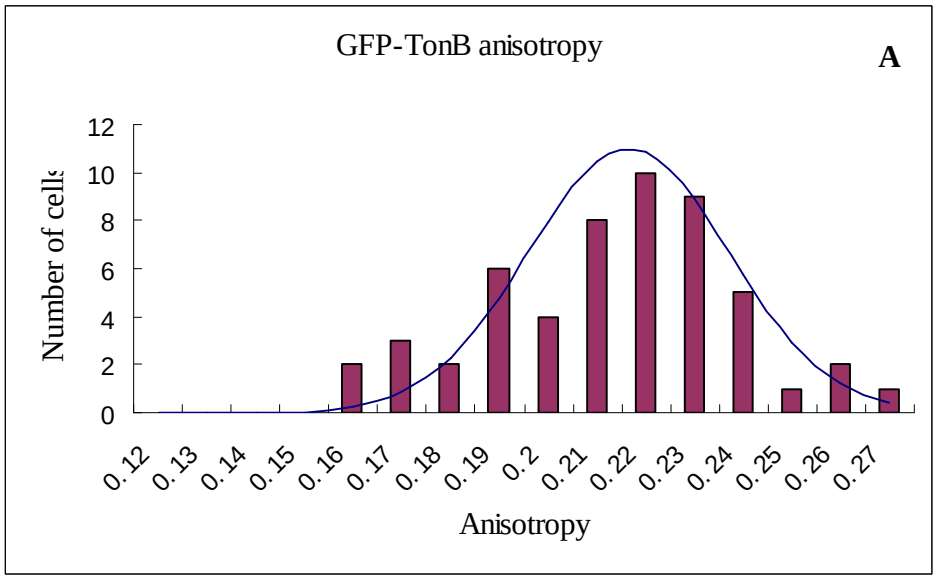

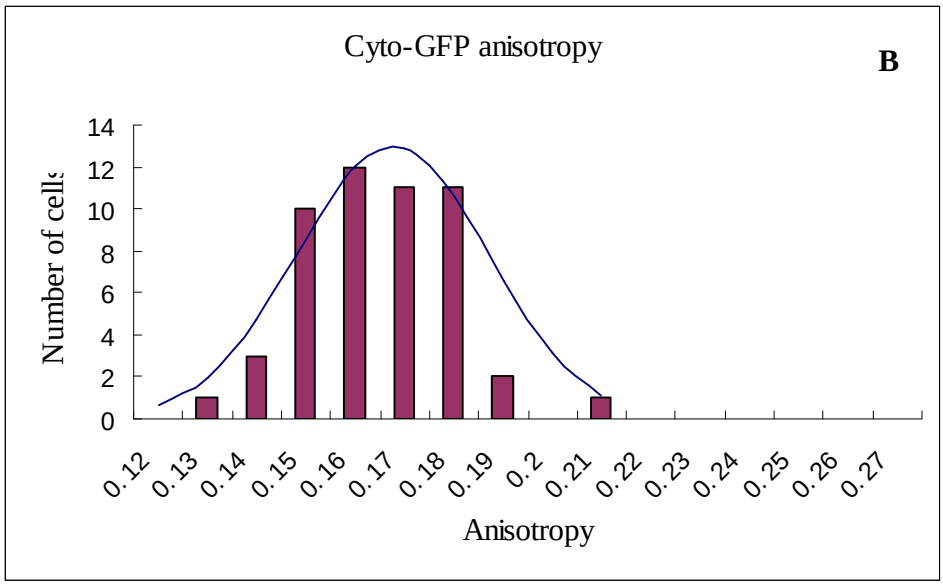

Figure 4.6 Anisotropy distribution of GFP-TonB (A) and GFP-in-cytoplasm(B)

This experiment was repeated in other period where the instrumental polarization alignment had been changed. In one period, the average anisotropy of GFP-TonB was 0.255 (n=19, standard deviation was 0.070), and the average anisotropy of cyto-GFP was 0.240 (n=15, standard deviation was 0.059). In another period, the average anisotropy of

GFP-TonB was 0.173 (n=34, standard deviation was 0.046), and the average anisotropy of cyto-GFP was 0.159 (n=31, standard deviation was 0.045). These results showed that the average anisotropy measured in different periods is not reproducible. This could be due to the change in the instrumental conditions after the polarization realignment. Meanwhile, the sample size might also affect the results. The measurements on the second and the third periods were performed with the sample sizes less than 20 and 40, respectively. The results were less precise as that on the first period (sample size is 50), as seen from the larger standard deviations. The result on the first period was therefore more representative, since it was based on a larger sample size.

Overall, the results from all three periods agree with one another, in a semi-quantitative fashion, that the GFP-TonB has a higher anisotropy than the cyto-GFP. The slightly higher anisotropy indicates that GFP-TonB is less mobile than the cyto-GFP, which is consistent with the different localization of GFP in the two cell constructs. In GFP-TonB cells, GFP is genetically fused to TonB, the inner membrane protein with equal size as GFP in number of amino acid residues (TonB has 239 aa whereas GFP has 238 aa), whereas in cyto-GFP cells GFP is placed in the aqueous cytoplasmic compartment without linking with any other substance.

4.3.5 Comparison between the anisotropy of GFP-TonB and FM-FepA in E. Coli cells

In this experiment, we compared the average anisotropy of GFP-TonB with the

anisotropy of FM-FepA (fluorescein maleimide linked to the outer membrane FepA) to validate our methodology for the observation of GFP motions in living *E. Coli* cells. The anisotropy of these two fluorophores in the cells was measured under the same conditions.

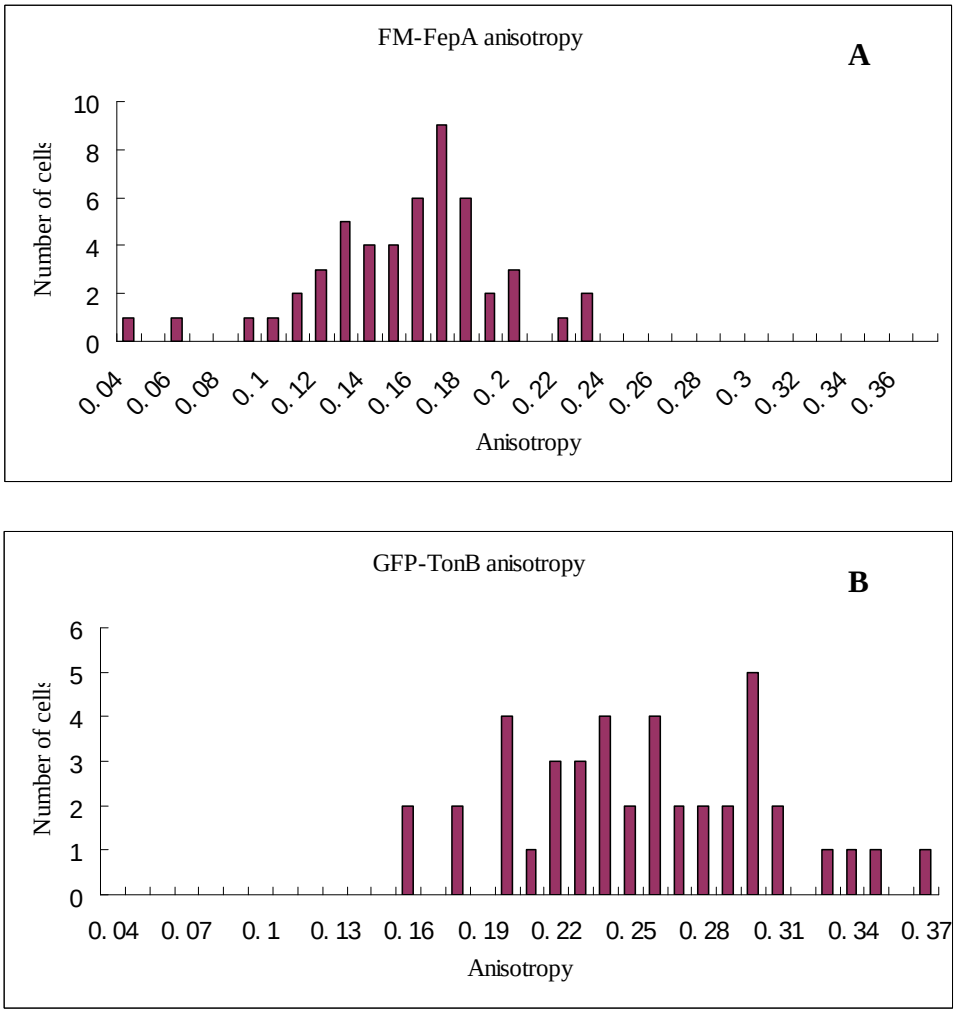

Figure 4.7 Anisotropy distribution of FM-FepA (A) and GFP-TonB (B)

The data showed that (1) the average anisotropy of FM-FepA was 0.151 (n=51, standard deviation was 0.037); (2) the average anisotropy of GFP-TonB was 0.251 (n=42, standard deviation was 0.050). Figure 4.7 showed that the anisotropy distribution of

cyto-GFP locates more on the left side of the x-axis standing for smaller anisotropy values, compared to that of GFP-TonB. The result demonstrates that overall FM-FepA has a small anisotropy than GFP-TonB does, suggesting that FM enjoys more rotational motion.

These two fluorophores expressed in *E. Coli* Cells, GFP and FM, are very different in their molecular weight. FM, being a small dye, is 427 D. GFP, being a small protein, is 27 kD. Their locations in the cell are also different. As shown in Figure 4.8, GFP links to the inner membrane protein TonB (239 aa) at the cytoplasmic side. FM binds to the outer membrane protein FepA (725 aa).

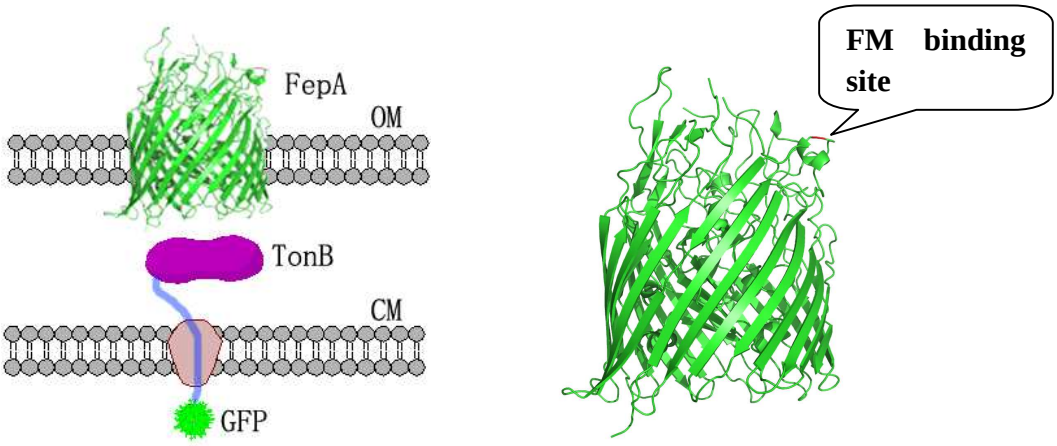

Figure 4.8 Localizations of FM-FepA and GFP-TonB
1. FM-FepA and GFP-TonB in the membrane (left). 2. Magnified FepA structure with FM labeled (right). Crystallographic structures of FepA (ID: 1FEP) was from the RCSB Protein Data Bank (http://pdbbeta.rcsb.org/pdb/home/home.do).

To label the FepA with FM, the original amino acid residue serine at the position 271 of FepA was deleted and substituted with cysteine by site-directed mutagenesis. The sulfhydryl side chain of the cysteine reacted with FM at pH 8□forming a stable thio-ether bond. The reaction between FM and the cysteine is shown in Figure 4.9.

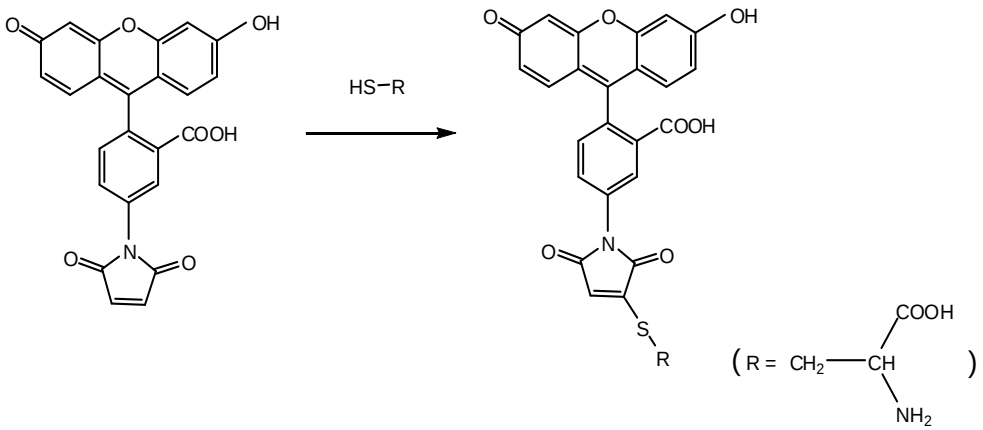

Figure 4.9 FM fluorescence modification to the cystine residue of FepA at S271C (FepA structure is not shown)

Our data demonstrated the different level of mobility the membrane-bound FM and membrane-bound GFP undergo in *E. Coli* cells. Being a smaller molecule (427D), FM seems to enjoy more rotational motion compared to GFP (27 kD), which is about 63 times larger than FM in molecular weight, shown as a lower anisotropy, FM (r=0.151) compared to GFP (r = 0.251).

In a previous experiment, we measured the anisotropy of fluorescein (FL, from which FM is derived) and GFP solution using the same microscope. The data showed that the anisotropy of FL and GFP in aqueous solution were 0 and 0.22, respectively (notice that the *G* factor for calculating the anisotropy was obtained by forcing the anisotropy of FL to be 0). FM is derived from FL with an addition of a maleimide group; therefore we should expect that free FM in solution should have an anisotropy value very close to 0, due to very similar molecular size (332D *vs.* 427D) and shape. The anisotropy measured using the fluorescence microscope was lower than that measured using a fluorometer (the

anisotropy value of GFP in solution was 0.283±0.002 measured by a fluorometer). This could possibly be due to the mixing of the polarization components of both the excitation and emission light caused by the high numerical aperture objectives. Also notice that the bulk measurements of the anisotropy of a fluorophore in the solution were more reproducible compared to the measurements of a fluorophore in the cell.

Together with FM and GFP measured in aqueous solution, our results indicated that, firstly, no matter bound (in the cell) or unbound (in the aqueous solution) FM is relatively more mobile than GFP. This can be attributed to the dramatic difference in molecular weight between these two molecules, with GFP 63 times larger than FM. Secondly, both bound FM and bound GFP show a higher anisotropy than their unbound forms, indicating a restricted rotational motion.

Our data also indicated that compared with GFP-TonB and cyto-GFP experiments (Section 5.3.4), the difference between GFP-TonB and FM-FepA seems more significant. The former experiment compared a larger fluorophore (GFP) at the two different locations, one anchored to TonB at the cytoplasmic side and the other solely staying in the cytoplasm of the living cells, whereas the latter experiment compared two fluorophores (GFP and FM) with totally different molecular weight (27 kD and 427 D, one is 63 times larger than the other). The anisotropy of a molecule is affected by the intrinsic properties of the molecule itself (e.g. the size and shape, and fluorescence lifetime) and the environment where it resides (e.g. the viscosity). According to Perrin equation,

$$\frac{r_0}{r} = 1 + \frac{\tau}{t_r} = 1 + 6D_r\tau \quad (4.2)$$

where r_0 is the maximum fluorescence anisotropy, τ is the fluorescence lifetime, t_r is the rotational correlation time, and D_r is the rotational diffusion coefficient. t_r is given by

$$t_r = \frac{\eta V}{RT} \quad (4.3)$$

where η is the viscosity, T is the temperature, R is the gas constant, and V is the volume of the rotating unit. The translational diffusion coefficient (D_t) is related to the average hydrodynamic radius (R_h) of the molecules as shown in the Stokes-Einstein equation assuming spherical particles,

$$R_h = \frac{\kappa_B T}{6\eta\pi D_t} \quad (4.4)$$

where k_B is the Boltzmann constant. These equations reveal how anisotropy values are affected by the size and fluorescence lifetime of the molecules. Small molecules have a small volume (or hydrodynamic radius) and the rotational correlation time is smaller than the fluorescence lifetime of the molecules, resulting in a small anisotropy value in aqueous solution (close to zero). For macromolecules, the change in motion cannot be easily distinguished by fluorescence anisotropy, because high intrinsic steady-state anisotropy is associated with its large hydrodynamic radius. GFP is a cylinder-shaped protein, with a physical dimension of 2.4 nm in diameter and 4.2 nm in length[26]. The R_h of GFP in

solution was reported to be about 2.3 nm [27]. With such a large size, the rotational correlation time is also large (20 ns), which is much larger than the fluorescence lifetime (τ = 2.9 ns in solution and τ = 2.6 ns in cells)[28], therefore the anisotropy value of GFP in solution is relatively larger (0.283 as measured in a fluorometer).

Due to the high intrinsic steady-state anisotropy of GFP, we should not see a significant change in anisotropy between GFP-TonB and cyto-GFP. As for FM and GFP, bound or unbound, the difference is much easier to see since we compare two fluorophores that have dramatically different weight (one is 63 times larger than the other) and different size). Our experiments demonstrated that when GFP and FM both bind to a membrane protein, their motions are restricted, but being a smaller molecule, bound FM still enjoys more motion compared to bind GFP.

Another thing we need to consider in comparing the anisotropy of FM-FepA and GFP-TonB is the relative motion of the membrane proteins that FM and GFP bind to. FepA resides in the outer membrane (OM) while TonB resides in the inner membrane (IM). The OM is less thermally mobile compared to the IM, probably because the phospholipid bilayer connects to the lipopolysaccarides at the outside leaflet. For IM, however, the IM phospholipids do not have those parts to connect with. Rather, they connect to two aqueous compartments at sides, the periplasm and the cytoplasm. The IM protein TonB therefore may enjoy more thermal motion than the OM protein FepA does, since the IM is more fluid-like than the OM. This may lower the anisotropy of GFP-TonB slightly. Furthermore, as will be discussed later, TonB, known to function as energy transducer

during iron transport in *E. Coli*, is speculated to undergo constant conformational change in fulfilling its function. As the surveillance model postulates in describing its mechanism, TonB may undergo some constant motions with the consumption of the energy in form of proton motive force. If so, we may also see another anisotropy decrease, too. Yet, even though these (thermal motion of the IM and motion of TonB) might contribute to the decrease of anisotropy, the GFP (linked to TonB) still have a higher anisotropic value than FM (linked to FepA), simply because it is too much larger in size.

In conclusion, although a reproducible absolute anisotropic value can not be achieved due to change in instrumental conditions (such as polarization alignment and *G* factor), our methodology is able to show that that FM-FepA in the living cells has a lower anisotropy than GFP-TonB in the living cells, which make sense when we consider their huge difference in molecular size. Binding to the membrane proteins limit their motion in a way that increases their anisotropy, still bound FM has a relatively lower anisotropy than bound GFP. As controlled experiments, these experiments (including Sections 4.3.4 and 4.3.5 experiments) validated our methodology in measuring the motion of GFP in living cells. With this methodology, we were able to distinguish the different motions between cytoplasmic GFP and TonB bound GFP as well as FepA-bound FM and TonB-bound GFP. After these, the major part of our experiments would be focused on observing the motion of GFP-TonB under various conditions, for instance, under difference energy poisons or during the process of iron transport.

4.3.6 Effect of the energy inhibitor carbonyl cyanide m-chlorophenyl hydrazone (CCCP) on GFP-TonB's motion

As mentioned in the introduction, the transport of iron across OM into periplasm requires energy and TonB. The cytoplasmic membrane PMF is utilized as the energy source in this process. A recently developed model for TonB's mechanism in iron transport hypothesize that TonB is constantly surveying under the peptidoglycan-associated outer membrane proteins until it finds the ligand-bound receptor protein. The question is what is the driving force for such motion? Is it energy-dependent?

To answer this question, the energy inhibitor CCCP was used to stop the PMF and the motions of TonB before and after addition of CCCP was investigated. The structure of CCCP is shown in Figure 4.10. CCCP is a weak acid (pKa = 5.7) and is soluble in fat. Being a weak acid it binds protons on one side of a membrane, and being fat-soluble it drifts to the opposite side of the membrane and gives away the protons. The proton ionophore CCCP can therefore disrupt cell membrane proton gradient and dissipate the PMF across the membrane[29].

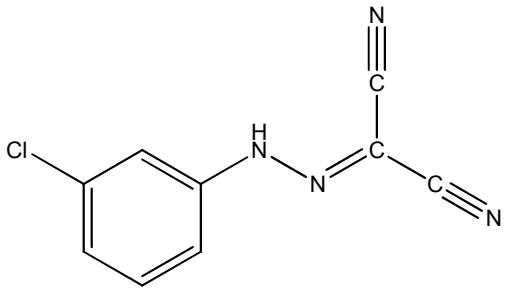

Figure 4.10 Structure of CCCP

In this experiment, the anisotropy of a cell before and after adding CCCP was measured. Considering the instrumental limitations, this measurement was performed very carefully on a one-cell-per-sample basis, that is, we measured the fluorescence anisotropy of GFP at the same location in a cell before and after adding CCCP, without changing anything in the microscope during the two measurements. The only difference was the addition of CCCP and a 10 minute wait after its addition. These would make sure that the result (change in anisotropy) is reliable, not caused by the change of the experimental condition but caused exactly by the addition of CCCP. Each time after the initial measurement of anisotropy, 5 μL CCCP (100 mM) was carefully added to the 500 μL cell solution, resulting in a final concentration of 1 mM CCCP. The real-time fluorescence intensity trajectory of the cell was recorded for 5 seconds for each anisotropy measurement. The anisotropy of each cell was then calculated, based on the fluorescence trajectory. The results showed that the average anisotropy of GFP-TonB cells before adding CCCP was 0.256 (n=50, standard deviation was 0.031), and after adding CCCP the average anisotropy of these cells was changed to 0.302 (n=50, and standard deviation was 0.042). Figure 4.11A and B give the anisotropy distribution of GFP-TonB before (A) and after (B) adding CCCP. From the curves, it was found that the anisotropy distribution of GFP-TonB after adding CCCP shifts slightly to the right side of x-axis compared with that after adding CCCP, indicating that GFP-TonB's motion was restricted after the addition of CCCP. Figure 4.11C gives the distribution of the anisotropy change after adding CCCP for the same 50 cells studied. The curves roughly show a Gaussian distribution, with the

mean of the curve at 0.048 (indicating the average amount of change in anisotropy) and the full width at half maximum (FWHW) at 0.069. Together, these data show that GFP-TonB cells respond to change in energy: when the energy is depleted of by the energy inhibitor CCCP, GFP-TonB's motion is restricted.

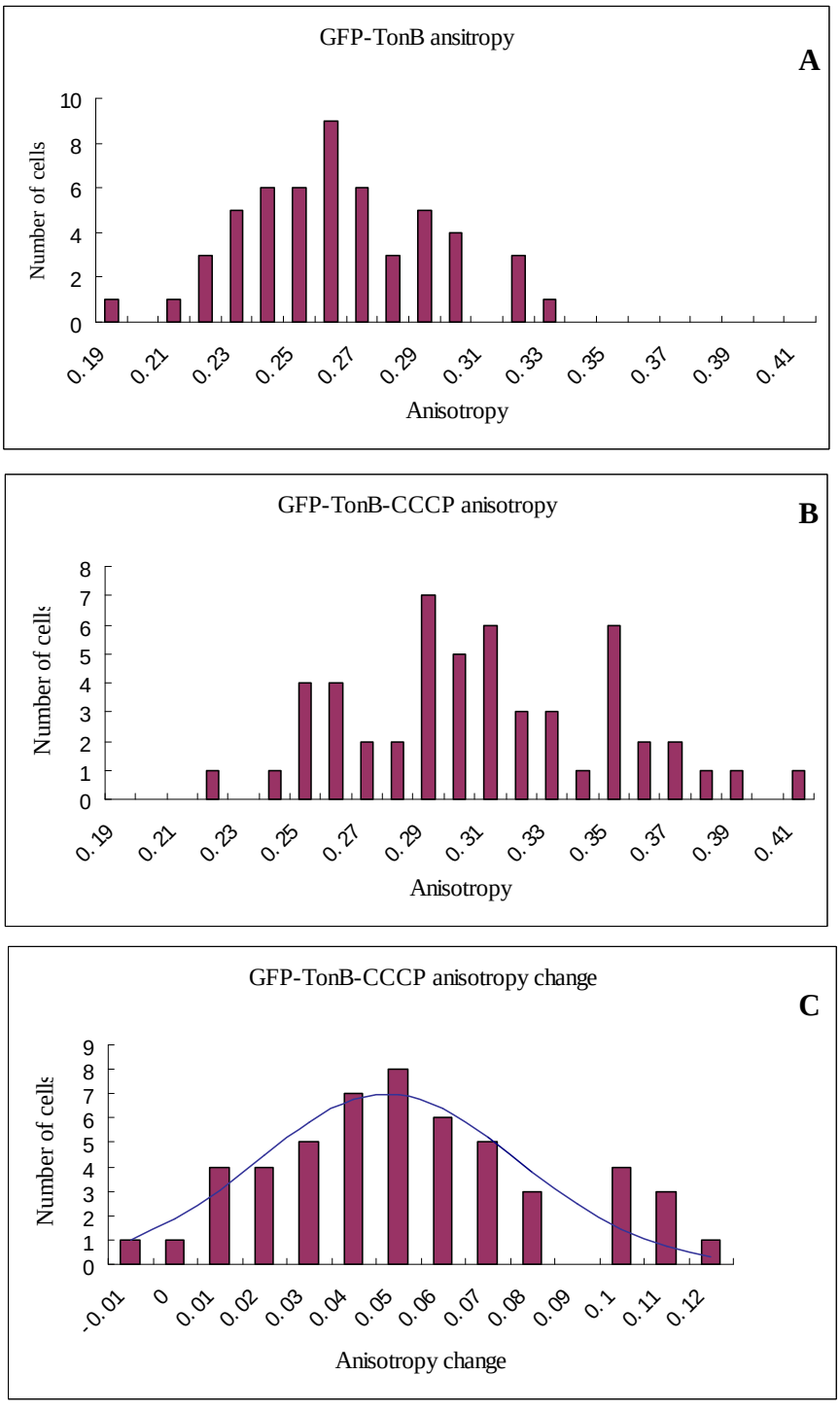

Figure 4.11 The anisotropy of GFP-TonB before and after adding CCCP

(A) before adding CCCP; (B) after adding CCCP; (C) the anisotropy change of GFP-TonB after adding CCCP (the curve in C is the Gaussian fitting).

Several control experiments were performed in order to ensure that the anisotropy change of GFP-TonB was indeed caused by the addition of CCCP and that CCCP affected the motion of TonB, not GFP. First, we investigated whether the 10-minutes waiting time and the action of adding 5 μL solution to the 500 μL cell sample solution during the measurement could cause any change in anisotropy. The experiments were repeated exactly the same way as those performed by adding CCCP except that, instead of adding CCCP, either no solution or 5 μL buffer was added. The results indicated that no significant change in anisotropy was observed. Therefore it is evident that the addition of CCCP is responsible for the anisotropy change in the GFP-TonB cells. Second, another control experiment performed was to compare the anisotropy change of GFP-TonB cells and the anisotropy change of cyto-GFP cells upon adding CCCP. The anisotropy of 25 cells was measured. Afterwards, 5 μL CCCP was carefully added to the 500 μL cell sample. Again, the anisotropies of 25 cells were measured. The results showed that the cyto-GFP cells did not have significant change in anisotropy (the average change in anisotropy ΔR=-0.020). Compared with cyto-GFP cells, the GFP-TonB cells showed a significant increase in the anisotropy (ΔR=+0.046). The second control experiment showed that CCCP causes GFP-TonB to become less mobile, through affecting TonB. GFP alone is not affected by CCCP, or at least does not have a decrease in motion when it encounters CCCP. Together with the one-cell-one sample experiment, our data demonstrated that TonB responds to the depletion of energy, resulting in an increase in anisotropy, which we interpreted as a decrease in motion due to lack of energy.

4.3.7 Effect of the energy inhibitor 2,4-dinitrophenol (DNP) on GFP-TonB's motion

A second energy inhibitor, DNP, was used to interrupt TonB's energy supply. The structure of DNP is shown in Figure 4.12. Similar to CCCP, the proton ionophore DNP is a weak acid and is fat-soluble. The uncoupling action of DNP is due to its ability to transport protons across the lipid bilayer and therefore dissipate the proton gradient across the membranes, leading to a rapid consumption of energy[30,31].

The effect of DNP on GFP-TonB's motion was investigated in a way similar to that of CCCP. The anisotropy of a single GFP-TonB cell was measured. 5 μL DNP (original concentration 200 mM) was added to the 500 μL cell solution. The final concentration of DNP in the cell sample solution is 2 mM. After 10 minutes, the anisotropy of the same cell was measured again. The measurement was performed on a one-cell-per-sample basis to guarantee obtaining accurate results. Different from adding CCCP, adding DNP to the cells caused a random change in the anisotropy. The average anisotropy, however, did not change much before and after adding DNP. The DNP solution has a bright yellow color similar to that of the GFP. The UV absorbance spectrum of the DNP solution (Figure 4.12) showed that at the concentration of 0.1 mM, DNP has a little absorption at 480 nm.

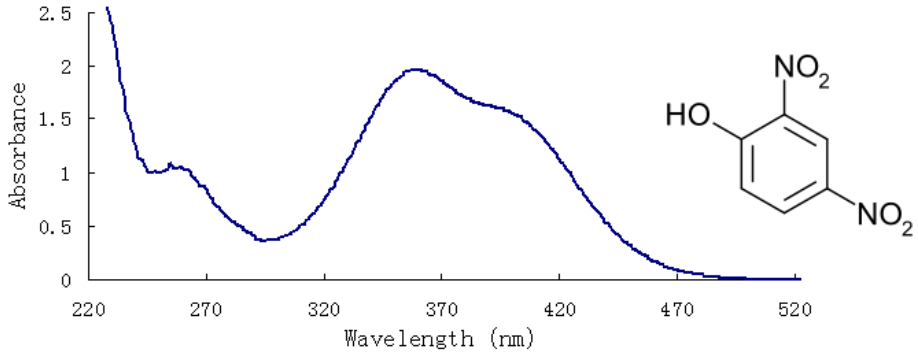

Figure 4.12 UV spectrum and structure and of DNP

It seems that DNP, at the concentration of 2 mM, is able to absorb a portion of the laser light (488 nm) and thus causes interference to the excitation light, which then affects the emission and the anisotropy measurements. Such interference might combine with the possible effect DNP may have on GFP-TonB cells, resulting in a random change in the anisotropy. To decrease such interference, we diluted the DNP solution by one fourth from 200 mM to 50 mM, which ended up with a final concentration of 0.5 mM in the cell sample solution. We measured the anisotropy before and after adding the DNP again. The results showed that the average anisotropy of GFP-TonB cells before adding DNP was 0.221 (n=53, standard deviation is 0.050), and after adding DNP the average anisotropy of these same GFP-TonB cells changed to 0.277 (n=53, and standard deviation is 0.076). By just comparing the average anisotropy, it seemed that adding DNP increased the anisotropy of GFP-TonB cells. However, the big standard deviation (0.076) in the second data set revealed that the anisotropy change fluctuated a lot after addition of DNP, which agreed with the results obtained at a higher concentration of DNP.

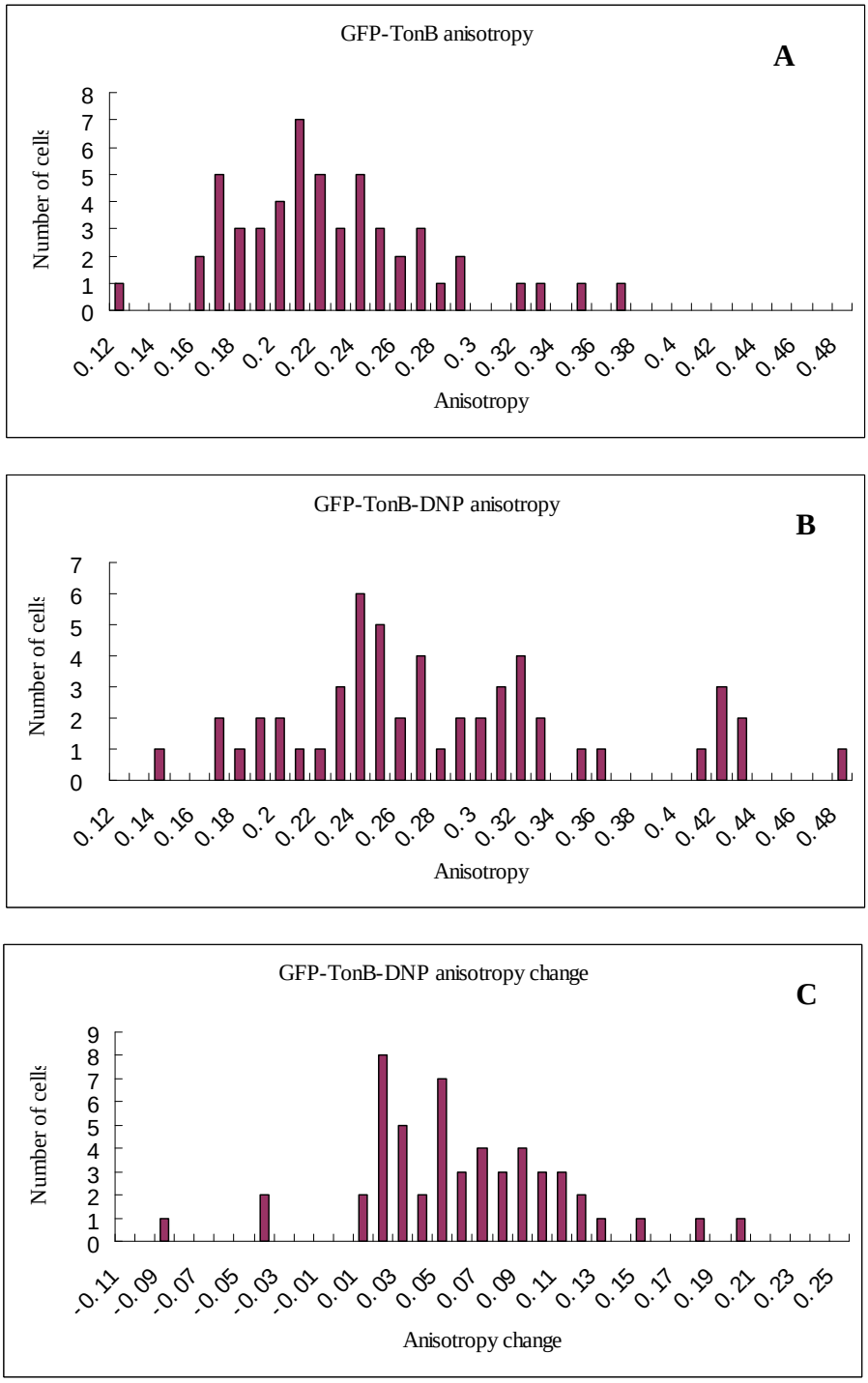

Figure 4.13 The anisotropy of GFP-TonB before (A) and after (B) adding DNP and the anisotropy change after adding DNP (C).

Figure 4.13A and B give the anisotropy distribution histogram of GFP-TonB before (A) and after (B) adding DNP. The anisotropy distribution of GFP-TonB cells without adding DNP (Figure 4.13A) shows a Gaussian shape. The anisotropy distribution of GFP-TonB with addition of DNP (Figure 4.13B), however, does not show a good Gaussian shape. Figure 4.13C gives the distribution of the anisotropy change after adding CCCP. It does not show a Gaussian shape, either, possibly due to the interference caused by DNP's absorption of the excitation light. Though the distribution of the anisotropy change does not look like Gaussian, it seems to indicate a positive change in the anisotropy since most data fall within the positive part of the x-axis.

Similar to that in the CCCP experiments, a control experiment was performed in order to ensure that the effect of DNP is directly on TonB. The experiment was performed by comparing the anisotropy change of GFP-TonB cells and the anisotropy change of cyto-GFP cells upon adding DNP. The anisotropy measurements of both cells were performed on the same day to guarantee that the instrumental condition was the same. The anisotropy of 25 cells was measured. Afterwards, 5 µL DNP 50 mM was carefully added to 500 µL cell sample. Again the anisotropies of another 25 cells were measured. The average anisotropy of each cell strain before and after adding DNP was calculated. The results showed that the GFP in the cytoplasm did not display an increase in anisotropy upon adding DNP, rather the anisotropy dropped a little (ΔR=-0.024). As for GFP-TonB cells, the anisotropy was found to increases slightly upon adding DNP (ΔR=0.004). The control experiment showed that DNP caused GFP-TonB to become less mobile, through

affecting TonB. GFP alone was not affected by DNP, or at least did not have a decrease in motion when it encounters DNP. Together with the one-cell-per-sample experiment, our data indicate that adding DNP as energy inhibitor seems to cause a positive change in the anisotropy of the GFP-TonB cells, but the change is not as significant as adding CCCP. This might be due to DNP's ability in absorbing part of the laser excitation, resulting in interference to the anisotropy of GFP-TonB.

4.3.8 Effect of the energy inhibitor sodium azide on GFP-TonB's motion

A third energy inhibitor sodium azide was used to interrupt TonB's energy supply. The structure of sodium azide is seen in Figure 4.14. Sodium azide blocks electron transport along the respiratory chain (complex IV), which is one of the five respiratory enzyme complexes. It inhibits cytochrome oxidase by binding irreversibly to the heme cofactor. As a result, the transfer of H^+ ion across the membrane to produce the proton gradient is stopped.

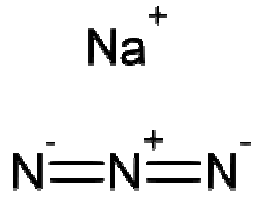

Figure 4.14 Structure of sodium azide

5 µL NaN_3 (concentration 1 M) was added to 500 µL GFP-TonB cells solution, resulting in a final concentration of 10 mM NaN_3. The measurement was performed on a one-cell-per-sample-basis. Similar to the CCCP experiments, adding NaN_3 caused a significant increase in anisotropic values. The results showed that the average anisotropy

of GFP-TonB cells was 0.241 (n=61, standard deviation was 0.049), and after adding azide the average anisotropy of these cells was changed to 0.302 (n=61, and standard deviation was 0.063). Figure 4.15A and B give the anisotropy distribution of GFP-TonB before (A) and after (B) adding azide. From the curves, it was found that the anisotropy distribution of GFP-TonB after adding azide shifts to the right size of the x-axis that stands for higher anisotropy, indicating that GFP-TonB's motion was restricted once the energy supply was gone. Figure 4.15C gives the distribution of the anisotropy change after adding azide, which shows a rough Gaussian shape, with the mean of the curve at 0.052 (indicating the average amount of the change in anisotropy) and the FWHW at 0.059. From the histogram, it seems that there are two Gaussian populations (with their means roughly at 0.06 and 0.1, respectively, suggesting *E. Coli* bacteria might undergo two different behaviors upon adding azide. The change in anisotropy were both positive, indicating that both types of *E. Coli* were less mobile upon adding azide. As we look at the data at section 4.3.6 again, *E coli* upon adding CCCP seemed to show two Gaussian populations (with their means roughly at 0.06 and 0.11, respectively) as well, although the second population (with the mean at 0.1) was smaller.

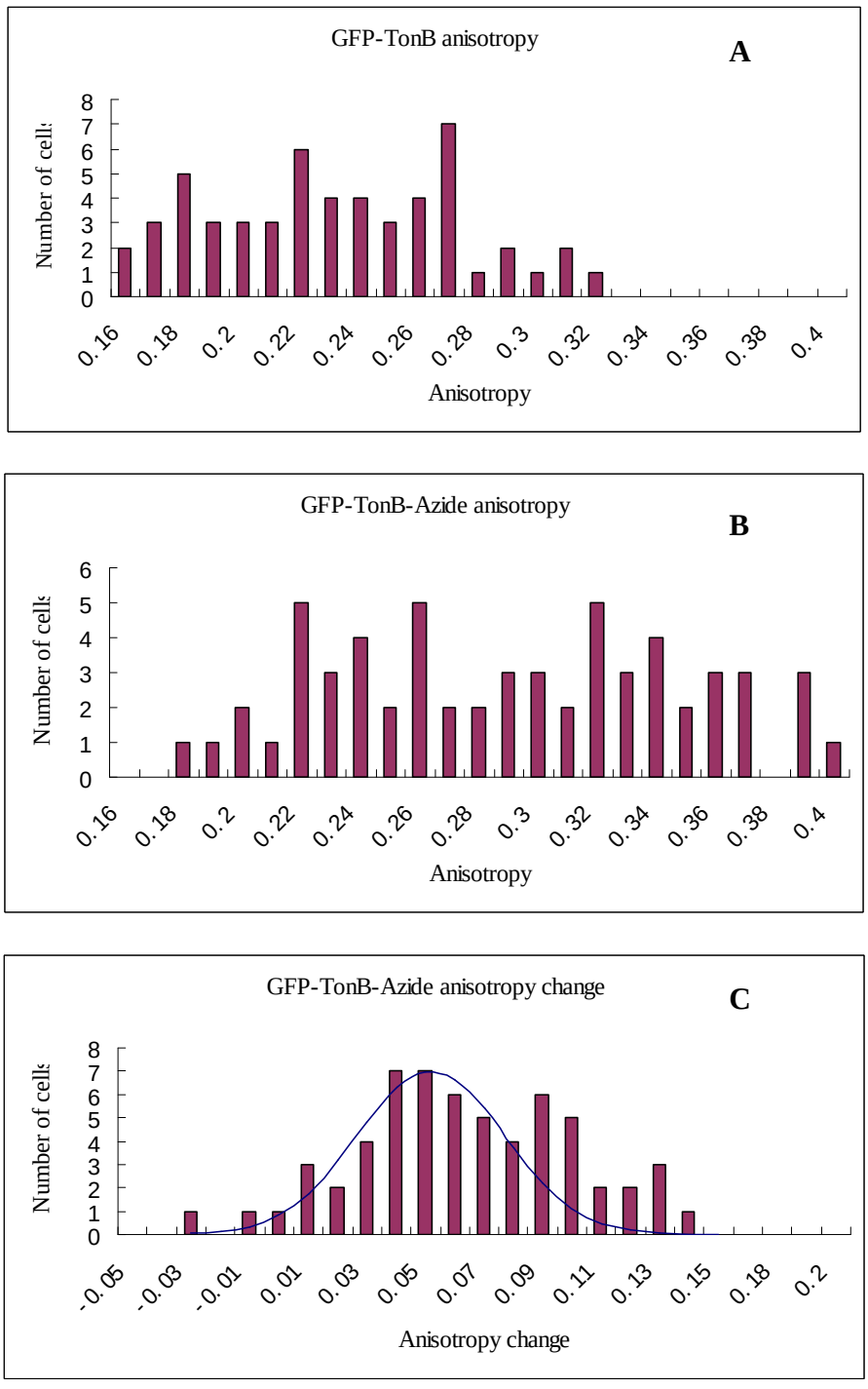

Figure 4.15 The anisotropy of GFP-TonB before (A) and after (B) adding azide and the anisotropy change after adding azide (C).

Similar to that in the CCCP and DNP experiments, a control experiment was performed in order to ensure that the effect of sodium azide was on TonB. The experiment was performed by comparing the anisotropy change of GFP-TonB cells and the anisotropy change of cyto-GFP cells upon adding sodium azide. The anisotropy measurements of both cells were performed on the same day to guarantee that the instrumental condition was the same. The anisotropy of 25 cells of each was measured. After that 5 μL sodium azide (1 mM) was carefully added to 500 μL cell sample. The anisotropies of 25 cells were measured again. The average anisotropy of each cell strain before and after adding sodium azide was calculated. The results showed that compared to cyto-GFP cell (the change in anisotropy $\Delta R = +0.007$), GFP-TonB cells ($\Delta R = +0.035$) showed a significant increase in the anisotropy. The control experiment indicated that sodium azide caused GFP-TonB to become less mobile, through affecting TonB. GFP alone was not affected by sodium azide, or at least did not have a decrease in motion when it encountered sodium azide. Together with the one-cell-one sample experiment, our data demonstrate that TonB responds to the depletion of energy, resulting in an increase in anisotropy, which we interpret as a decrease in motion due to lack of energy.

4.3.9 Change of anisotropy in GFP-TonB during iron transport

Previous study in Dr. Klebba's group showed that the *E. Coli* strain that expresses GFP-TonB hybrid proteins can bind and transport the iron siderophore complex, FeEnt. This indicates that TonB is functional even when it is linked to a GFP, the protein of equal

size. In this experiment, we examined whether or not the addition of FeEnt would cause any change in the motion of TonB. 5 µL FeEnt at an original concentration of 100 µM was added to 500 µL GFP-TonB cell solution, which ended up with a final concentration of 1 µM. The measurement was performed on a one-cell-per-sample basis. That is, we measured the anisotropy of each cell at the same location without touching the microscope between two measurements, before and after addition of FeEnt. The results showed that the average anisotropy of GFP-TonB cells was 0.234 (n=51, standard deviation was 0.58), and after adding FeEnt, the average anisotropy of these same GFP-TonB cells stayed about the same, 0.242 (n=51, and standard deviation was 0. 065). Figure 4.16A and B give the anisotropy distribution of GFP-TonB before (A) and after (B) adding FeEnt. From the histograms, it is found that the anisotropy distribution of GFP-TonB adding FeEnt almost completely overlap with that of GFP-TonB without adding FeEnt. Figure 4.16C gives the distribution of the anisotropy change after adding FeEnt, which looks like a Gaussian shape with the left side of the peak filled with data but the right side lacking data. If fit with a Gaussian function, the Gaussian curve has the mean at 0.014 (indicating the average amount of the change in anisotropy) and the FWHM at 0.052. Overall, we think that the anisotropy of GFP-TonB does not change much after adding FeEnt.

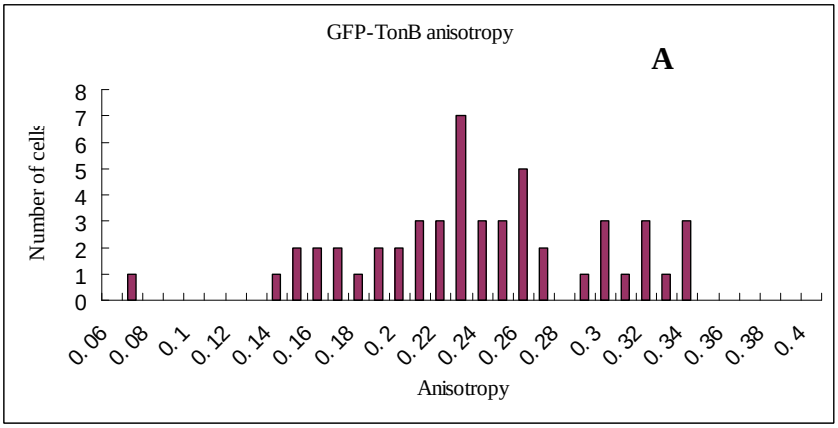

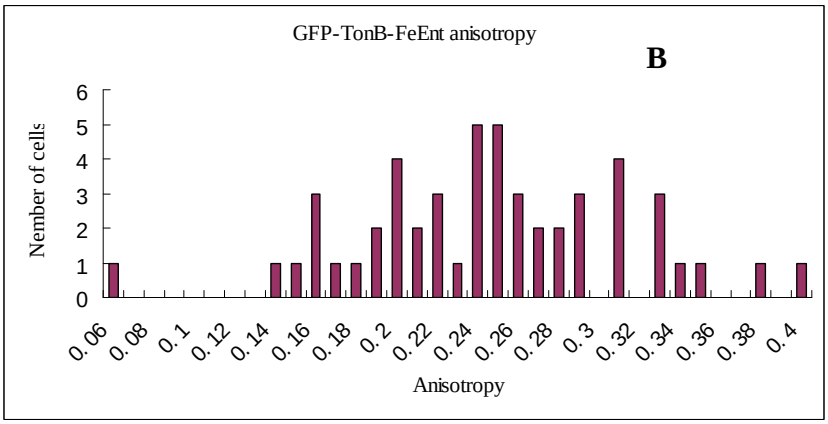

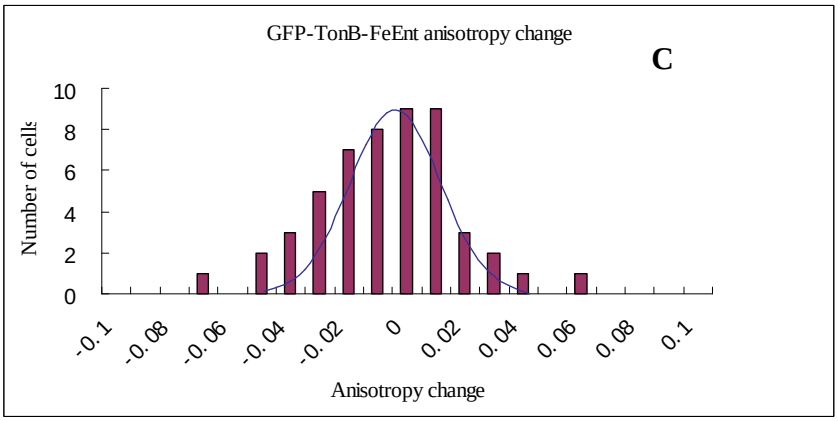

Figure 4.16 The anisotropy of GFP-TonB before (A) and after (B) adding FeEnt and the anisotropy change before and after adding FeEnt (C)

There are two explanations for such results. (1) The motion of GFP-TonB does not change during iron transport. However, as mentioned in the introduction, TonB was believed to undergo at least some conformational motion in order to facilitate iron transport. (2) The motion of GFP-TonB changes during iron transport, but it is not detected by anisotropy measurements. This seems more possible. The anisotropy we calculated was the average anisotropy of many GFP-TonB molecules measured at 50 ms dwell time for a time period of 5 s. If after adding FeEnt, the GFP-TonB molecules rotate more frequently and constantly during the measurement, we should see that the anisotropy of GFP-TonB decreases. Since we did not see the anisotropy decrease significantly, we can conclude that GFP-TonB does not experience such kind of motion upon adding FeEnt. If after adding FeEnt, GFP-TonB molecules undergo such motions: (i) GFP-TonB responds by decreasing or increasing in motion quickly and then returning to the original state for a much longer period of time (characteristics of a low duty cycle), or (ii) GFP-TonB increases or decreases its motion too slowly compared to the period for the measurement, we may not see much change in anisotropy. A more useful tool to observe such motions could be single-molecule spectroscopy. In single molecule measurements, only one single molecule is focused each time, and any change in the motion can be detected by tracking the fluorescence time trajectory. Therefore, single molecule spectroscopy can be the direction of our future study in this project in order to observe the motions of TonB during iron transport.

4.3.10 Comparison between the anisotropy of GFP-TonB and GFP-TonB with ExbB and ExbD deleted in E. Coli cells

TonB functions as an energy transducer for the transport of iron through the outer membrane to the periplasm. It is believed that TonB needs the other two inner membrane proteins in this process, ExbB and ExbD. These three proteins form a heteromultimetic complex and thus stabilize TonB and anchor TonB to the cytoplasmic membrane. TonB is therefore able to harness PMF and transduce the energy to facilitate iron transport, in a not yet well-understood way. In this case, the motion of TonB is restricted, and when ExbB and ExbD are not available, TonB should be more mobile. To verify this, the *E. coli* construct GUC41/pGT was cultured, in which the ExbB and ExbD genes were deleted (for convenience, this construct is called GFP-TonB-Mutant). The anisotropy of GFP in both the GFP-TonB and GFP-TonB-Mutant were measured in order to compare their motions. The anisotropy of GFP-TonB and GFP-TonB-Mutant were measured on the same day under the same conditions. The results showed that the average anisotropy value of the GFP-TonB cells was 0.223 (n=31, standard deviation was 0.055), and the average anisotropy of the GFP-TonB-Mutant was at 0.195 (n=53, standard deviation was 0.045). Figure 4.17A and B show the anisotropy distribution of GFP-TonB and GFP-TonB-Mutant. The curves show that the anisotropy of GFP-TonB-Mutant slightly shifts to the left side of the x-axis, indicating that it is a bit more mobile than GFP-TonB. The data are consistent with the hypothesis that ExbB and ExbD complex with TonB and

stabilize TonB at the inner membrane. When these two proteins are absent, TonB might be able to move around and even away from the inner membrane[14], thus causing a drop in the anisotropy value. In the case of GFP-TonB, TonB is less likely to get away from the inner membrane since it is linked to the reporter protein GFP at its N-terminus at the cytoplasmic side while the C-terminus part of it is in the periplasm; therefore TonB only showed a slightly decrease in anisotropy with deletion of ExbB and ExbD.

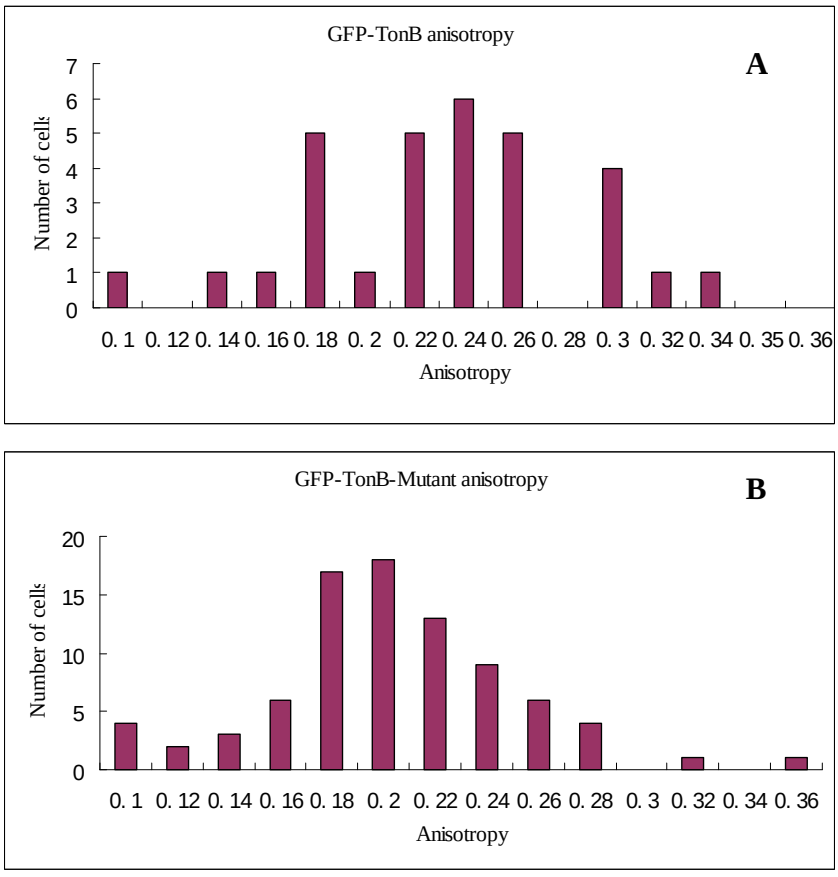

Figure 4.17 The anisotropy of GFP-TonB (A) and GFP-TonB-Mutant (B)

4.4 Conclusion

The inner membrane protein TonB plays an important role for iron transport in bacteria. It harnesses the proton motive force and transduces the energy to facilitate the iron transport through the outer membrane into the periplasm. TonB's role in iron transport has been well established, but exactly how it accomplishes this is still unclear. This project aims to continue with the investigation of TonB's mechanism through the study of TonB's motions. A series of experiments were designed for the observation of TonB's motions under different circumstances, such as without energy availability, during the process of iron transport, and without ExbB and ExbD proteins stabilizing TonB. The motions of TonB under these circumstances were compared with those under the normal conditions, using GFP as a reporter, which was genetically fused to the N-terminus of TonB.

The change in the sample's focusing positions and the polarization alignment of the instruments were two major influences on the measurements of anisotropy of living *E. Coli* cells. As a result, it is difficult to obtain reproducible anisotropy values measured in different periods. Nevertheless, our methodology is valid for the anisotropy of different samples measured in the same period, where the instrumental conditions vary less.

In the two control experiments, we compared GFP-TonB with cyto-GFP and compared GFP-TonB with FM-FepA in order to validate that our methodology was able to differentiate the different extent of motions that TonB undergoes in living bacteria, through the observation of GFP. In the first case, the average anisotropy of GFP-TonB

was found slightly higher than that of the cyto-GFP, which was consistent with the different mobility GFP experiences, due to different localizations of GFP in these cells. In the second case, GFP-TonB showed a significantly higher average anisotropy value than FM-FepA, which was consistent with the different mobility GFP and FM experience, due to great difference in molecular size. The two control experiments showed that we were able to observe and compare the motions of the GFP inside living bacteria cells by measuring anisotropy using a fluorescence microscope.

The role of energy availability on TonB's motions in living *E. Col*i cells was then examined. The apparent increase in the anisotropy of GFP-TonB after adding the energy inhibitors, CCCP and sodium azide, demonstrated that the motion of TonB is restricted due to depletion of PMF. Next, the motion of TonB during iron transport was investigated. When the iron siderophore complex FeEnt was added to the cells, the process of iron transport was activated. The anisotropy of GFP-TonB cells after adding FeEnt does not change much, indicating that transport of iron does not measurably affect the motion of TonB. Finally, the effect of two inner membrane proteins, ExbB and ExbD, on TonB's motion was studied. When ExbB and ExbD are deleted, the anisotropy of GFP-TonB decreases, indicating that TonB is more mobile without ExbB and ExbD. Our result agrees with the idea that the TonB/ExbB/ExbD complex stabilizes and anchors TonB to CM.

To summarize, (1) TonB's motion decreases in response to depletion of PMF, suggesting that TonB is using the energy, in form of PMF, for some constant motion. Our results support the TonB's "membrane surveillance" mechanism [17], which suggests that

TonB surveys under the outer membrane proteins in search of iron-bound receptors to activate iron transport through FepA. (2) During the process of iron transport, the change in TonB's motion is not measurably detected by anisotropy measurements, indicating that TonB does not become constantly more mobile. TonB might undergo quicker movement for a moment and then return to the original state for a much longer period (characteristics of a low duty cycle) or it might change its motion too slowly. Both types of motions can escape from being detected by bulk anisotropy measurements. In these cases, single GFP-TonB measurements will be more useful for the study of the motion of TonB during iron transport. This can be the direction of our future study. 3) TonB's motion increases when ExbB and ExbD are absent, which on the other hand indicates that ExbB and ExbD restrict TonB's motion.

Chapter 4 References

(1) Nikaido, H.; Saier, M. H., Jr. *Science* **1992**, *258*, 936.

(2) Winther, T.; Xu, L.; Berg-Sorensen, K.; Brown, S.; Oddershede, L. B. *Biophys. J.* **2009**, *97*, 1305.

(3) Postle, K.; Larsen, R. *BioMetals* **2007**, *20*, 453.

(4) Stintzi, A.; Barnes, C.; Xu, J.; Raymond, K. N. *Proc. Natl. Acad. Sci. U. S. A.* **2000**, *97*, 10691.

(5) Klebba, P. E.; Rutz, J. M.; Liu, J.; Murphy, C. K. *J. Bioenerg. Biomembr.* **1993**, *25*, 603.

(6) Carrano, C. J.; Raymond, K. N. *J. Am. Chem. Soc.* **1979**, *101*, 5401.

(7) Nikaido, H. *J Biol Chem* **1994**, *269*, 3905.

(8) Braun, V.; Gaisser, S.; Herrmann, C.; Kampfenkel, K.; Killmann, H.; Traub, I. *J Bacteriol* **1996**, *178*, 2836.

(9) Hannavy, K.; Barr, G. C.; Dorman, C. J.; Adamson, J.; Mazengera, L. R.; Gallagher, M. P.; Evans, J. S.; Levine, B. A.; Trayer, I. P.; Higgins, C. F. *J. Mol. Biol.* **1990**, *216*, 897.

(10) Larsen, R. A.; Thomas, M. G.; Postle, K. *Mol. Microbiol.* **1999**, *31*, 1809.

(11) Linton, K. J.; Higgins, C. F. *Mol. Microbiol.* **1998**, *28*, 5.

(12) Bradbeer, C. *J Bacteriol* **1993**, *175*, 3146.

(13) Braun, V. *ACS Chem. Biol.* **2006**, *1*, 352.

(14) Letain, T. E.; Postle, K. *Mol. Microbiol.* **1997**, *24*, 271.

(15) Postle, K.; Larsen, R. A. *Biometals.* **2007**, *20*, 453.

(16) Hancock, R. W.; Braun, V. *J. Bacteriol.* **1976**, *125*, 409.

(17) Kaserer, W. A.; Jiang, X.; Xiao, Q.; Scott, D. C.; Bauler, M.; Copeland, D.; Newton, S. M. C.; Klebba, P. E. *J. Bacteriol.* **2008**, *190*, 4001.

(18) Moeck, G. S.; Coulton, J. W. *Mol. Microbiol.* **1998**, *28*, 675.

(19) Larsen, R. A.; Letain, T. E.; Postle, K. *Mol. Microbiol.* **2003**, *49*, 211.

(20) Brewer, S.; Tolley, M.; Trayer, I. P.; Barr, G. C.; Dorman, C. J.; Hannavy, K.; Higgins, C. F.; Evans, J. S.; Levine, B. A.; Wormald, M. R. *J. Mol. Biol.* **1990**, *216*, 883.

(21) Roof, S. K.; Allard, J. D.; Bertrand, K. P.; Postle, K. *J. Bacteriol.* **1991**, *173*, 5554.

(22) Chang, C.; Mooser, A.; Plückthun, A.; Wlodawer, A. *J. Biol. Chem.* **2001**, *276*, 27535.

(23) Newton, S. M.; Trinh, V.; Pi, H.; Klebba, P. E. *J. Biol. Chem.* **2010**, *285*, 17488.

(24) Suhling, K.; Siegel, J.; Lanigan, P. M. P.; Lévêque-Fort, S.; Webb, S. E. D.; Phillips, D.; Davis, D. M.; French, P. M. W. *Opt. Lett.* **2004**, *29*, 584.

(25) Yang, F.; Moss, L.; Phillips, G. *Nat. Biotechnol.* **1996**, *14*, 1246.

(26) Ormo, M.; Cubitt, A. B.; Kallio, K.; Gross, L. A.; Tsien, R. Y.; Remington, S. J. *Science* **1996**, *273*, 1392.

(27) Hink, M. A.; Griep, R. A.; Borst, J. W.; van Hoek, A.; Eppink, M. H.; Schots, A.; Visser, A. J. *J Biol Chem* **2000**, *275*, 17556.

(28) Swaminathan, R.; Hoang, C. P.; verkman, A. S. *Biophys. J.* **1997**, *72*, 1900.

(29) Ghoul, M.; Pommepuy, M.; Moillo-Batt, A.; Cormier, M. *Appl. Environ. Microbiol.* **1989**, *55*, 1040.

(30) Donohue-Rolfe, A. M.; Schaechter, M. *Proc. Natl. Acad. Sci. U. S. A.* **1980**, *77*, 1867.

(31) Harold, F. M. *Bacteriol Rev* **1972**, *36*, 172.

Chapter 5: Molecular Mobility under Submicroscopic Liposomal Confinement inside the Hydrogel Matrix

5.1 Introduction

The incorporation of biomolecules into porous silica glass has provided a robust alternative to immobilize labile biological molecules for biosensor development[1-5]. Performance of a silica sol-gel biosensor is closely related to the characteristics of the encapsulated molecules and the sol-gel network. An enzyme that experiences restricted flexibility under nanoscopic confinement may not maintain its ability to undergo conformational changes as part of enzyme activity.

The effects of charge, size, and the polarity of the guest molecules and the porosity of the sol-gel network on the dopants' behavior had been investigated using both ensemble and single-molecule fluorescence spectroscopy[6-9]. It was found that regardless of molecular charges and polarity, small dye molecules were sufficiently immobilized in a silica alcogel, where the pore sizes are relatively smaller[6,7]. In a hydrogel with much larger pores and a high percentage of water, however, negatively charged fluorescein (FL) molecules enjoyed much greater rotational and translational mobility than the positively charged rhodamine 6G (R6G) molecules, indicating that electrostatic interactions dictated the mobility inside the hydrogel[8]. As for green fluorescence protein (GFP), its motion was restricted, possibly due to the effect of molecular templating.

Molecular templating is a very common phenomenon in silica sol-gel composites, where a doped guest molecule serves as a template for silica pore formation when a liquid sol gradually gels into a solid composite, thus trapping the guest molecule inside a pore of similar shape and dimension. For biosensor development, molecular templating continued to be a major concern in the synthesis of active silica biocomposite materials. Even though the pore dimension is opened up by diluting the liquid sol with a suitable solvent before gelation sets in, the effect of molecular templating on the mobility may not be completely avoided for macromolecules[8].

A novel protocol was proposed to solve for such problems mentioned above[10]. In the protocol, a protein was trapped inside 200 nm (diameter) liposomes. The liposomes templated the pores sizes of the silica sol-gel materials to a submicroscopic dimension and protected the protein molecules inside the liposomes from protein-silica interactions and molecular templating effect during the process of gelation. After the sol-gel solidified, the silica matrix was shocked by strong electrical pulse to break apart the liposomes and release the proteins for subsequent applications. The ability of this protocol to yield active silica biocomposites was demonstrated using proteins including GFP, horseradish peroxidase , and a more fragile enzyme firefly luciferase .

The current project focuses on examining how the spatial restriction exerted by the liposomes might affect the mobility of the entrapped molecules. The guest molecules are entrapped inside the submicroscopic liposomes of various sizes (100 nm, 200 nm, and 400 nm in diameter). The submicroscopic liposomes are used as they are big enough for

entrapping macromolecules. R6G and FL are chosen as fluorescence probes and are entrapped inside the liposomes. R6G and FL are positively charged and negatively charged, respectively, at neutral pH condition; therefore they can be good reporters for trapped biomolecules with charges at physiological condition.

The physical properties of many substances under nanoporous confinement had been studied and had been found different from that in the bulk state[11-14]. For instance, upon incorporation into the nanoporous silica (from 8 nm to 125 nm), phenolic resin was found to have a lower curing temperature and that there was an inverse linear dependence between the pore size and the curing temperature[13]. Under confinement (from 0.4 nm to 2.1 nm) in nanoporous organosilicate films, the mobility of the linear alkane molecules became increasingly affected by van der Waals interactions between the molecules and the methyl groups on pore surfaces as the pore size decreased[11]. As a result, the diffusivity of the organic molecules decreased as the pore size decreased and as the carbon chain length increased. When confined within random nanoporous glasses with nominal pore sizes between 2.5 nm and 20 nm, the poly(dimethyl siloxane) (PDMS) and poly(methyl phenyl siloxane) (PMPS) polymers were found to have faster molecular dynamics than in the bulk state[14]. A laser dye DCM was trapped in DPPC vesicle entrapped in a sodium silicate derived sol-gel glass[15]. It was found that the solvation dynamics of 4-(dicyanomethylene)-2-methyl-(p-dimethyl-aminostyryl) 4H-pyran (DCM) was different from the bulk solvation, which could be described by a fast and a slow component.

Those publications mentioned above were all for neutral molecules trapped in small

confinements. In this project, charged R6G and FL are trapped inside liposomes of known sizes (100 nm, 200 nm, and 400 nm) in order for us to investigate the effect of spatial, liposomal confinement on the molecular mobility. The mobility of R6G and FL inside the liposomes is studied using fluorescence polarization modulation and fluorescence anisotropy. Polarization modulation had been used to study the reorientational dynamics of single fluorescence dye molecules attached to DNA strands that were absorbed onto a glass surface[16,17]. Here, polarization modulation is used to obtain the rotational mobility of the confined R6G molecules. When probe molecules are excited with linearly polarized light whose polarization angle is modulated from 0 to 180 degrees, the extent to which the fluorescence is modulated will reveal the rotational mobility of the molecules within the period of the polarization modulation. The phase shift and the modulation depth, extracted from the modulation data, are used to evaluate the relative mobility of the molecules under the submicroscopic confinement. Meanwhile, the rotational flexibility of the dye molecules is also examined using fluorescence anisotropy, which is a more popular method.

5.2 Experimental

5.2.1 Materials

The Sol-gel materials (tetramethyl orthosilicate (TMOS) and tetraethyl orthosilicate (TEOS)), the fluorescence dyes (R6G and FL), cholesterol, and dihexadecyl phosphate were all purchased from Sigma-Aldrich. The lipid, dimyristoylphospatidylcholine

(DMPC), was purchased from Avanti Polar Lipids. All reagents were used as received. Microscope cover glasses (Fisher Premium) were purchased from Fisher Scientific and were thoroughly cleaned by consecutive sonication in a 10% sodium hydroxide solution, distilled water, acetone, and deionized water for 1 hour each, respectively, before use.

5.2.2 Preparation of dye loaded liposomes

A 5:4:1 molar ratio phospholipid stock solution of DMPC: cholesterol: dihexadecyl phosphate was prepared by dissolving 1.670 g DMPC, 773 mg cholesterol, and 273 mg dihexadecyl phosphate in 10 mL chloroform. This lipid cocktail stock solution of 250 mM DMPC, 200 mM cholesterol, and 50 mM dihexadecyl phosphate in a sealed round bottom flask was then stored in the refrigerator for future use. To prepare dye-doped liposomes, the solvent in a 14 μL lipid stock solution was evaporated using a dry and gentle nitrogen stream, which yielded a thin lipid film on the wall inside a microtube. The film was immediately reconstituted in 28 μL dry isopropanol with rapid vortexing. Next, 500 μL 1×10^{-4} M R6G or FL (prepared in 10 mM phosphate buffer, pH 7.0) was added to the reconstituted phospholipid mixture and the resultant solution was then vigorously mixed for 5 minutes to form R6G-liposomes or FL-liposomes. To prepare liposomes with different sizes, dye-doped liposomes were passed back and forth 20 times through the polycarbonate membranes of different pore sizes (100 nm, 200 nm, and 400 nm in diameter) installed inside a mini-extrusion device (purchased from Avanti Polar Lipids). All dye-doped liposomes were prepared freshly each day for use.

To separate the dye-doped liposomes from the free dye solution, a Nap™-10 column containing Sephadex™ G-25, purchased from GE Healthcare, was used. The Nap™-10 column allows big particles to be eluted first. A 500 μL R6G-liposome or FL-liposome sample was added to the column and allowed to enter the gel bed completely. The same amount of the elution buffer (10 mM phosphate buffer, pH 7.0) was added and allowed to enter the gel bed completely so that the combined volume of sample inside the gel bed equals 1.0 mL. Next, the sample was eluted with phosphate buffer (pH 7.0) and collected portion by portion for a total of 10 portions. For each portion, 500 μL buffer was used. The fluorescence intensity of each portion was measured. The first two portions (portion No.1 and No.2), containing dye-doped liposomes in the buffer solution, were used to prepare the liposome-incorporated hydrogel.

5.2.3 Preparation of the liposome-incorporated hydrogel

A sol solution was firstly prepared by mixing TMOS, H_2O, and HCl (0.01N) with volumes of 562.5 μL, 120 μL, and 11.25 μL, respectively. To facilitate acid hydrolysis, the sol solution was sonicated in an ice bath for half an hour. Trapping of the dye-doped liposomes was made before polycondensation of the sol solution. That is, the sol solution was mixed with the phosphate buffer solution (pH 7.0) containing the liposomes (portion No.1 or No.2) to facilitate the formation of a gel network. The volume ratio of the sol to the buffer was 1:10. Formation of the hydrogel occurred within half an hour.

A sandwich-structured thin hydrogel sample was made by first stacking two cover

glasses together using a double-sided tape as a spacer to form a thin solution chamber. Then a 50 μL sol solution was added to a 500 μL 10 mM phosphate buffer (pH 7.0) containing the liposomes of specific size and mixed by vortexing for about 10 s. 40 μL of the sample mixture was then transferred and spread inside the chamber. The opening of the solution chamber was then sealed to prevent drying of the hydrogel sample after gelation.

5.2.4 Fluorescence modulations

The mobility of molecules encapsulated inside the liposomes that were subsequently incorporated inside the hydrogel in the sandwich structure was examined by fluorescence polarization modulation. We used the fluorescence modulation depth and the phase shift obtained from the polarization modulation to evaluate mobility. To obtain the modulation depth, the experiment was performed by modulating continuously the polarization angle of the linearly-polarized laser excitation for four periods by manually and continuously rotating the half-wave plate from 0 degrees to 720 degrees. The polarizing beam-splitter was used to resolve the fluorescence into a parallel component (I_{II}) and a perpendicular component ($I_{\perp}$), however, only one component (for example, I_{II}) and its according detector (for example, detector 1) was used to record the fluorescence-time trajectory (a diagram for the instrumental setup is shown in Figure 2.2, Chapter 2). The fluorescence intensity *versus* time was then plotted. The fluorescence time course followed a cosine-square function as shown below,

$$I(t) = A\cos^2 \omega t + C \qquad (5.1)$$

where *A* is the amplitude of the cosine square curve, ω is the polarization rotation rate, *t* is time, and *C* is the minimum fluorescence of the data. Because the polarization angle was rotated manually, we did not have a known, constant ω. However, this did not matter because what we wanted to know was the modulation depth, which is related to *A* only. Since different samples have different dye concentrations, it is difficult to compare the modulation depth by just comparing the amplitude of the fluorescence modulation curve. We calculated the relative fluorescence intensity and generated a new cosine-square function for the data,

$$I'(t) = \frac{I(t)}{I_{ave}} = M\cos^2 \omega t + C' \qquad (5.2)$$

where $I'(t)$ is the relative fluorescence intensity, and I_{ave} is the average fluorescence of the sample during the period, *C'* is the minimum fluorescence of the new curve. *M* is the relative amplitude, which is the modulation depth with which we used to compare mobility.

For measurements of the modulation phase shift, the experiment was performed by modulating the polarization direction of the linearly-polarized laser excitation from 0° to 180° by rotating the half-wave plate from 0° to 90° with an increment of 5°. The polarizing beam-splitter was used and the total fluorescence was resolved into a parallel component (I_{II}) and a perpendicular component ($I_{\perp}$), which were subsequently collected by two APD detectors. The average fluorescence intensity of each component *versus* the

polarization angle was plotted. The two curves were fit to Eq. 5.3 to obtain their respective modulation phases (ϕ_{II} and $\phi_{\perp}$), as shown below,

(5.3)

$$I = A\cos^2(x+\phi) + C$$ where A is the amplitude of the cosine-square curve, x is the polarization angle, ϕ is the phase shift relative to that of the excitation light, and C is the minimum fluorescence of the data. The phase shift ($\Delta\phi$) between the two fluorescence modulation curves of the same liposome, with which we used to compare mobility, was calculated by the following equation,

$$\Delta\phi = \left|\phi_{II} - \phi_{\perp}\right| \qquad (5.4)$$

where ϕ_{II} and $\phi_{\perp}$ are the phase shifts of the parallel and perpendicular components relative to the excitation modulation, respectively.

5.2.5 Fluorescence anisotropy bulk measurements

Fluorescence anisotropy measurements of bulk liposome samples were performed using a Shimadzu RF-3101PC fluorometer in order to study the mobility of dye-doped liposomes incorporated inside the hydrogel monoliths. The spectra were recorded at λ_{ex} = 488 nm for FL and λ_{ex} = 514 nm for R6G. All fluorescence anisotropy values were calculated based on the following equations,

$$r = \left(I_{VV} - GI_{VH}\right)/\left(I_{VV} + 2GI_{VH}\right) \qquad (5.5)$$

$$G = I_{HV}/I_{HH} \qquad (5.6)$$

where r is the anisotropy and G is a correction factor used to correct any polarization bias

in the fluorometer. I_{VV}, $I_{VH,}$ I_{HH}, and I_{HV} are the fluorescence intensities measured with different excitation and emission schemes. For example, I_{VV} is the fluorescence intensity with vertically-polarized excitation and vertically-polarized emission, whereas I_{VH} is the fluorescence intensity with vertically-polarized excitation and horizontally-polarized emission.

5.2.5 Fluorescence anisotropy of FL in single liposomes

We measured the anisotropy of the fluorescent molecules within a single liposome using the home-built fluorescence microscope with linearly-polarized laser light. To measure the anisotropy, the liposome was first brought to the laser focus by the nano-positioning controlling electronics. The center of the liposome was then exposed to the excitation light for 5 to 10 seconds. Meanwhile, the fluorescence intensity was resolved into two components, and they were recorded by two detectors. All fluorescence anisotropy values were calculated on the basis of the following equation:

$$r(t) = \frac{I_{II}(t) - G \cdot I_{\perp}(t)}{I_{II}(t) + 2 \cdot G \cdot I_{\perp}(t)} \qquad (5.7)$$

where r is anisotropy, I_{II} and $I_{\perp}$ are the fluorescence intensities of the parallel and perpendicular components of the fluorescence emission. G is a correction factor used to correct any polarization bias in the microscope. The G factor was calculated daily using FL solution (10^{-5}M), by artificially forcing the anisotropy of this solution to be 0.

5.3 Results and discussion

5.3.1 Separation of dye-doped liposomes from the free dye residue

It is necessary to separate the dye doped liposomes from the free dye solution where liposomes are formed, so that the free dye molecules in the solution won't cause much interference. The separation was conducted using a Nap^{TM}-10 column (details are described in the experimental section 5.2.2). Figure 5.1 shows the results. The curve with diamonds (A) shows the change in fluorescence intensity of the dye-doped liposomes in each elution portion whereas the curve with squares (B) shows that of the free dye solution in each elution portion, which was used as a control. Both samples contained the same concentration of dye. Compared to curve B, the first two portions of curve A shows that there was fluorescence from the first two portions. In the Nap^{TM}-10 column, larger particles are eluted out first due to size exclusion. The fluorescence shown in the first two portions indicates these portions contained dye-doped liposomes. Curve B, on the other hand, does not show any fluorescence intensity in the first two portions since there were only free dye molecules, which would be kept in the gel bed longer due to small molecular size. From the fourth portion and afterwards, curve B shows a steady increase in fluorescence intensity, due to elution of free dyes, whereas Curve A shows similar trend except on portion 4 and 5, which has much higher fluorescence intensity, possibly due to the combination of very small liposomes with the free dye molecules. Based on the observation, the first two portions were collected for later study.

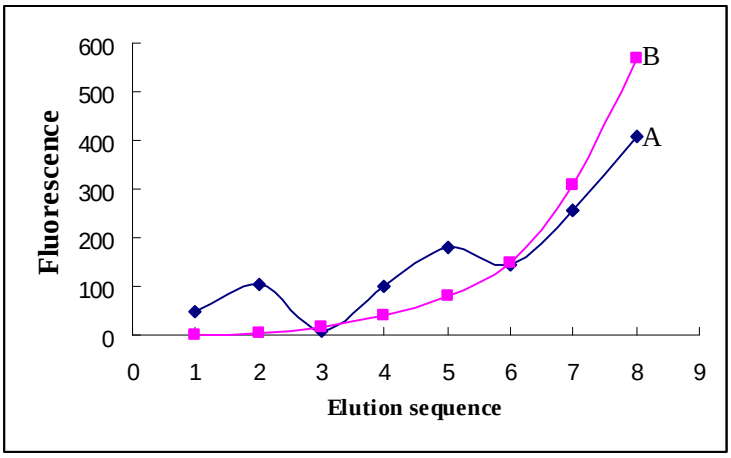

Figure 5.1 The separation of R6G-liposomes from free R6G solution by Nap^{TM} -10 column.
A. The R6G-liposomes sample; B. Free R6G solution used as a control.

5.3.2 Fluorescence images

Figure 5.2 shows the fluorescence images of R6G-liposomes (200 nm) entrapped inside the sol-gel. The image displays well-defined circular fluorescence spots, indicating R6G-liposomes. There are almost no non-circular fluorescent spots or streaks, characteristics of the single-R6G-molecule image, as shown in chapter 3. In addition, when the bright-spot area was shined by the laser light, no dark state and photobleaching were observed from it, which are also characteristics of the single-molecule spectra. Together, these prove that the bright spots are R6G-liposomes, not single R6G molecules. The R6G-liposomes image has liposome to background intensity ratio about 10:1. Compared to blank liposomes that do not contain R6G molecules, the intensity in the background area of the R6G-liposomes image is higher, indicating that the background

contained R6G molecules. The fluorescence from the background could be caused by leaking of a small portion of R6G molecules before and after the hydrogel gelation. The dimmer spots in the image are the out-of-focus R6G-liposomes.

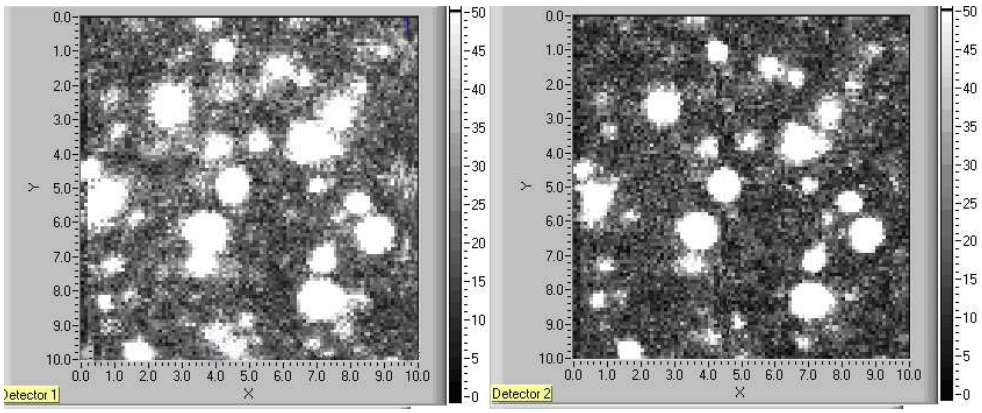

Figure 5.2 Fluorescence images of R6G-liposomes (200 nm) in a hydrogel

5.3.3 Polarization modulation

5.3.3.1 Polarization modulation depth

Figure 5.3 shows the fluorescence time trace of R6G molecules within the liposomes that were entrapped either in the hydrogel, in the solution, or directly entrapped inside the hydrogel. Within this time course, the half-wave plate was rotated from 0 to 360 degrees, meaning the direction of the excitation polarization was modulated for 4 periods, as seen in the figure. The polarizing beam-splitter was used to resolve the emission into two orthogonal components (I_{II} and $I_{\perp}$); however, only one component (I_{II}) and its according detector were used to record the fluorescence-time trajectory. For comparison,

the same fluorescence component and the same detector were used for all the three samples. The fluorescence intensity was normalized by the average fluorescence intensity (the instantaneous intensity divided by the average intensity during this time course), so that the modulation depth can be compared. As the figure shows, it is very apparent that the fluorescence emission of R6G molecules was modulated according to the excitation modulation to different degrees and the modulation depth reflected the different mobility of the molecules.

For R6G molecules in the solution, the molecules are freely tumbling, undergoing Brownian motion. While being excited by the excitation light at one polarization angle, these molecules keep tumbling around and therefore the emission distributes almost evenly at each polarization direction, forming circularly polarized fluorescence. When it comes to another excitation polarization angle, the same happens, that is, the quick reorientation of the transition dipoles of the molecules eliminates the excitation modulation. Therefore when the fluorescence is resolved into two orthogonal polarization components, ideally, the fluorescence intensity of both components should be the same and we should see just a flat line at y =1 in the modulation figure. However, as shown in Figure 5.3A, a small modulation with a depth of about 0.2 was shown. This is possibly due to the different transmission efficiency and detector sensitivity at different excitation polarization angle.

Compared to R6G in the solution, the R6G molecules directly encapsulated insider the hydrogel (Figure 5.3B) has a much bigger modulation depth (about 1.2). The R6G

molecules inside the hydrogel were reported to be mostly immobilized according to our previous research[8]. When the immobilized R6G molecules are excited by polarization-modulated laser light□the fluorescence intensity are determined by the angle (θ) between the electric field ($\vec{E}$) of the excitation light and the fluorescence component (in this case, I_{II}) of the emission, which was recorded. Generally, I_{II} follows a $cos^2(\theta)$ curve. When $\vec{E}$ is parallel with I_{II} (θ is 0 degrees), the fluorescence intensity recorded is at the maximum. On the contrary, if $\vec{E}$ is orthogonal to I_{II} (θ is 90 degrees), the fluorescence intensity recorded is at the minimum. Therefore when $\vec{E}$ of the excitation is modulated from 0 to 720 degrees, the fluorescence component I_{II} is modulated in a cosine-square fashion. As seen in the figure, the modulation depth of immobilized R6G inside the hydrogel is much larger than that of the free R6G in the solution.

Figure 5.3C shows that the modulation depth (about 0.5) of R6G molecules inside the liposomes (200 nm in diameter) is between free R6G molecules and immobilized R6G molecules, indicating that the mobility of the R6G-in-liposomes molecules are in between these two. Such observation would be supported by fluorescence anisotropy experiments which measures mobility in a more common way, as would be discussed later.

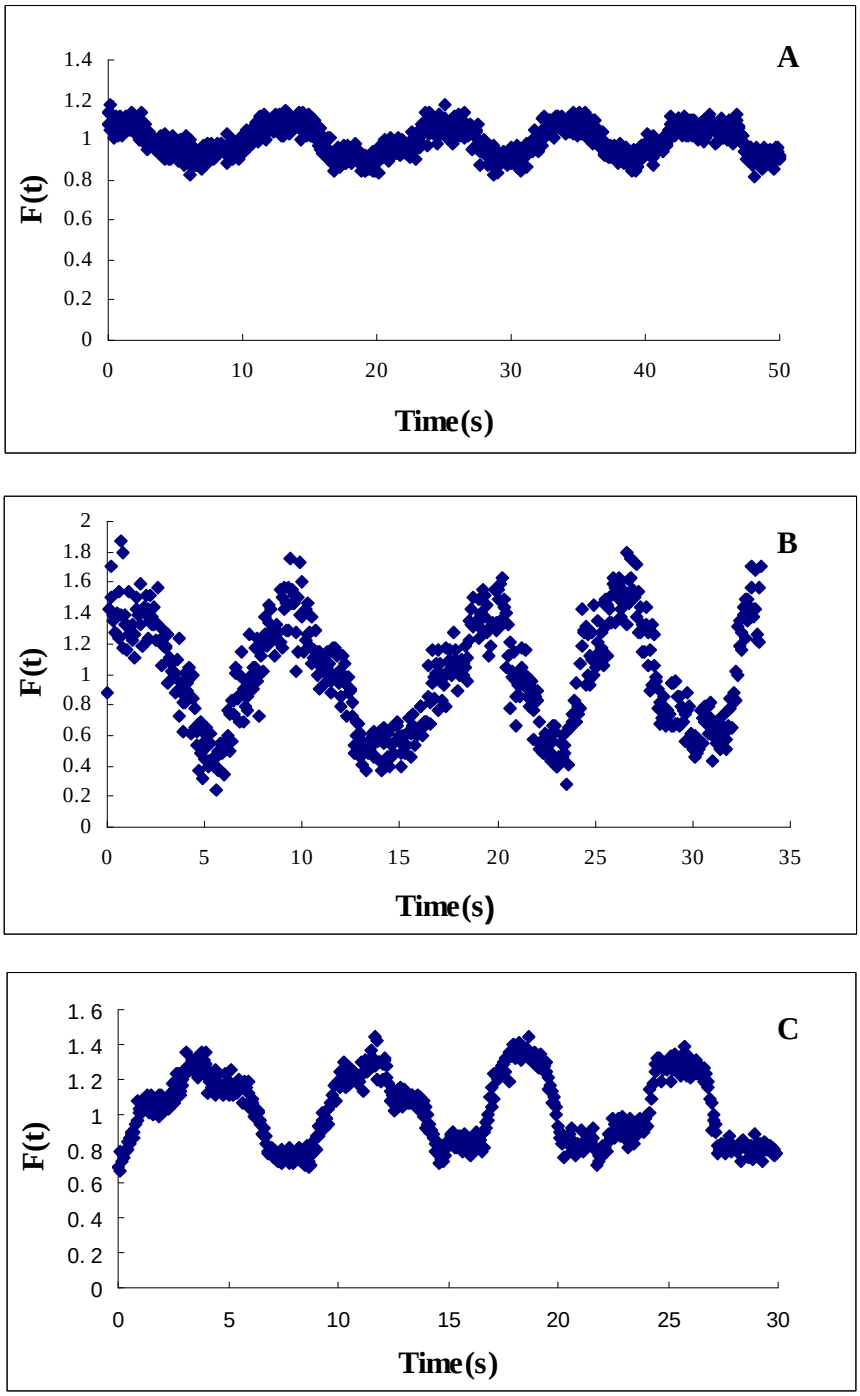

Figure 5.3 Fluorescence time trace of ensemble R6G molecules for four periods A: R6G in solution; B: R6G directly entrapped in hydrogel; C: R6G-liposome (200 nm) entrapped in hydrogel

5.3.3.2 Phase shift

Figure 5.4 compares the fluorescence phase shifts of R6G molecules in liposomes of different sizes. The polarization of the excitation light was modulated from 0 degrees to 180 degrees by rotating the half-wave plate from 0 to 90 degrees with an increment of 5 degrees. The emission upon the polarization-modulated excitation was split by a polarizing beam-splitter into two orthogonally polarized components (I_{II} and $I_{\perp}$), and their respective fluorescence signals were recorded by two detectors. For freely rotating molecules in the solution, similar to the explanation for modulation depth, the polarization of the emission is randomized, which means the fluorescence is equally resolved into two polarization components at each excitation polarization angle, resulting in the same phase between the two signals. For immobilized molecules, also similar to the explanation for modulation depth, the emission polarization will mostly follow the electric field of the excitation polarization, and the intensity of each fluorescence component depends on the angle between it and the electric field of the excitation (θ). Both I_{II} and $I_{\perp}$ follow a $cos^2(\theta)$ curve and they are anticorrelated. That is, when the electric field of the excitation aligns with I_{II} of the emission (θ for I_{II} is 0 degrees and for $I_{\perp}$ is 90 degrees), the signal of I_{II} is at the maximum and the signal of $I_{\perp}$ is at the minimum. On the other hand, when the electric field of the excitation aligns with $I_{\perp}$ (θ for I_{II} is 90 degrees and for $I_{\perp}$ is 0 degrees), the signal of I_{II} is at the minimum and $I_{\perp}$ is at the maximum. So for totally immobilized molecules, the two fluorescence signals have a 90° phase

difference. For intermediate molecules with the mobility lying between mobile and immobile, the phase change is between 0° and 90°. The phase difference therefore tells about the degree of mobility of molecules. The results shown in Figure 5.4 demonstrate that in the different sizes of liposomes, the R6G molecules show different phase shifts between the two fluorescence curves. In the 100 nm liposomes (Figure 5.4A), a phase shift of 73.8 degrees was found between I_{II} and $I_{\perp}$ curves, whereas in the 200 nm liposomes and 400 nm liposomes, the phase shifts are 58.7 and 34.1, respectively. The decrease in phase shift as the liposomes become larger reveals that the mobility of R6G molecules inside the liposomes are different, with a larger liposome rendering more mobile molecules, and vice versa. Such observation would be supported by the subsequent fluorescence anisotropy experiments which measured the mobility of R6G-liposomes of various sizes in a more popular way.

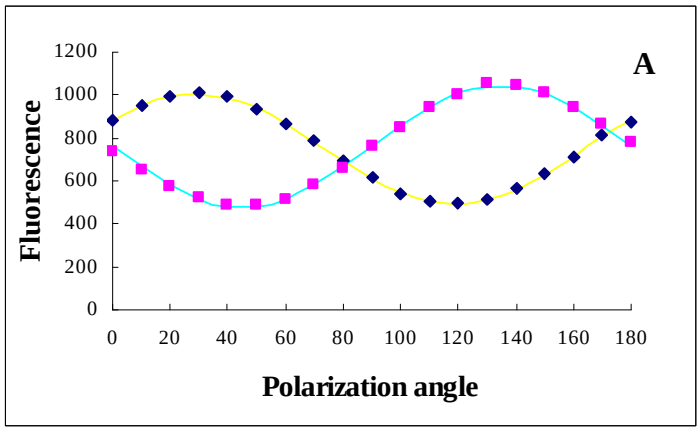

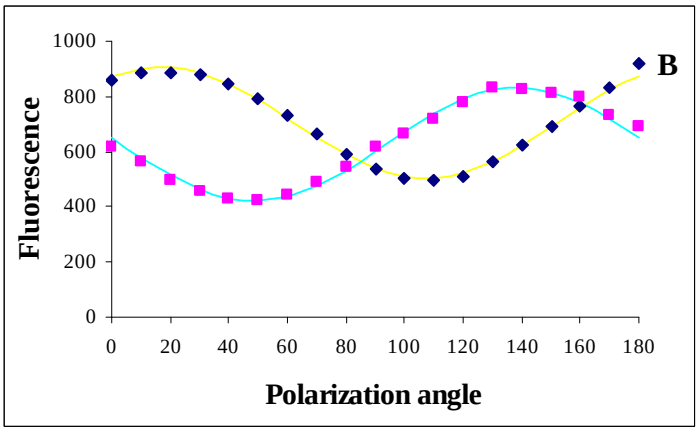

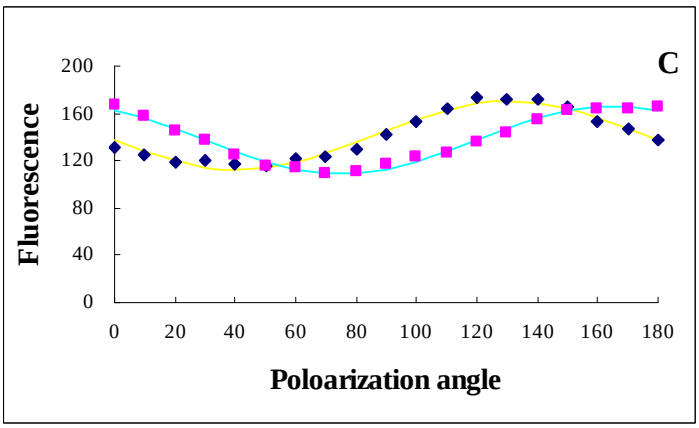

Figure 5.4 The fluorescence modulations of ensemble R6G molecules inside different sizes of liposomes entrapped in hydrogel.

A. a 100 nm liposome; B. a 200 nm liposome; C. a 400 nm liposome. Excitation polarization was modulated from 0 to 180 degrees, and the signal was measured in two orthogonally polarized channels. Diamonds and squares are the data points. Smooth lines are the fitting curves.

5.3.4 Steady-state fluorescence anisotropy

As complementary experiments, steady-state fluorescence anisotropy was performed. Table 5.1 shows the steady-state anisotropy values of R6G-liposomes in the hydrogel. The anisotropy of R6G molecules are 0.241 (n=4, standard deviation is 0.020), 0.214 (n=4, standard deviation is 0.020), 0.177 (n=4, standard deviation is 0.025), in 100 nm, 200 nm, and 400 nm liposomes, respectively. It was obvious that the anisotropy of R6G molecules decreases as the liposomes' diameter increases, indicating that R6G molecules are more mobile in a less confined environment.

Table 5.1 Fluorescence anisotropy of R6G in different samples

Liposomes 100 nm	Liposomes 200 nm	Liposomes 400 nm	Hydrogel	Solution
0.241±0.020	0.214±0.020	0.177±0.025	0.301±0.022	0.013±0.001

For comparison, the fluorescence anisotropy of R6G molecules that were directly entrapped in a freshly prepared hydrogel was measured. The anisotropy of R6G inside the hydrogel is higher (r = 0.301±0.022, n=4,) shown in Table 5.1. In addition, the anisotropy of bulk R6G in the solution was measured (r = 0.013±0.001, n=4), shown also in Table 5.1.

Altogether, both the anisotropy and the fluorescence modulation measurements agree with each other. First, the results demonstrated that trapping R6G molecules in the liposomes improved the mobility of R6G in the hydrogel (indicated as a smaller

modulation depth and a smaller anisotropy) compared to those directly entrapped inside the hydrogel. As Chapter 3 mentioned, due to electrostatic interactions, R6G molecules directly trapped in the hydrogel was firmly attracted to the silica surface during and after gelation process, thus the mobility was highly restricted[8]. Here we demonstrated that liposomes are able to protect the entrapped R6G molecules from directly contacting with the hydrogel matrix and thus avoid the electrostatic interactions between R6G and the sol-gel host.

Second, the results demonstrated that R6G trapped in liposomes (no matter what sizes) have lower mobility (indicated as a bigger modulation depth and higher anisotropy) compared with R6G in the solution. This indicates that while on the one hand liposomes protect R6G molecules from directly interacting with the hydrogel network, on the other hand, the submicroscopic confinement that the liposomes exert on the molecules affect the mobility of the molecules. It has been reported that molecules under the nanoscopic or microscopic confinement behaved differently in view of solvation dynamics, compared to those in the bulk solution[9,15,18,19]. Generally, the solvation dynamics display two components: a fast component and a slow component. While the fast component may be ascribed to the dynamics of the solvent molecules residing in the water pool of the compartment, the slow component originates from the surface retardation effect inside the confinement. Similarly, the mobility of R6G molecules in the liposomes could be explained as the co-functioning of a fast component and a slow component. R6G molecules residing at the lipid surface represent a slow component and the molecules in

the water pool represent a fast component. The decrease in mobility inside the liposomes compared to those in the solution could be explained as the influence of the slow mobility at the surface. For R6G in the liposomes, the slow mobility at the lipid surface may come from several factors as listed below. (i) As mentioned above, the solvation dynamics of R6G at the surface is slower. (ii) DMPC is known as a zwitterionic lipid carrying a positive charge and a negative charge at its hydrophilic head group. The structure of DMPC is shown below (Figure 5.5A),

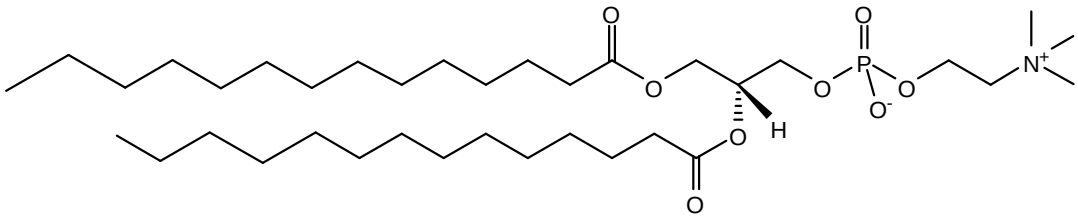

(A)

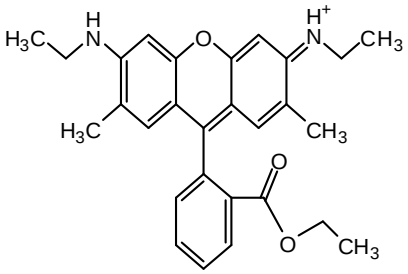

(B)

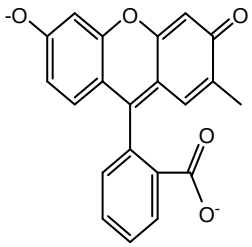

(C)

Figure 5.5 Structure of DMPC (A), R6G (B), and FL (C)

Thus R6G molecules could be attracted to the negative part at the head group of DMPC lipid due to electrostatic interaction. (iii) With 2 methyl and 3 ethyl side groups (as shown in Figure 5.5B), R6G could be attracted to the fatty alkyl groups of the lipid bilayer

through hydrophobic interaction, similar to the way that some membrane proteins are anchored to the biological membrane. (iv) The -NH group of the R6G molecule could also form hydrogen bonds with the oxygen atoms at the lipid head group. Together, these interactions restrict the mobility of R6G molecules at that area.

Third, the results demonstrated that, for R6G-liposomes of all three sizes, R6G mobility increases as the liposomes' diameter increases (indicated as decreasing modulation phase shifts and decreasing anisotropies). This can be explained as follow. As the diameter increases, both the surface area and the volume of the water pool increase. However, the increase in the volume is larger than the increase in surface. As a result, the fraction of molecules in the water pool versus those at the surface increases. Therefore the mobility of R6G in the liposome increases.

5.3.5 Fluorescence anisotropy of single FL-liposomes

The fluorescein (FL) molecules inside different sizes of liposomes were also studied. Table 5.2 shows that the average anisotropy of FL in 100 nm, 200 nm, and 400 nm liposomes are 0.160 (n=29, standard deviation 0.039), 0.124 (n=29, standard deviation 0.024), and 0.063 (n=21, standard deviation 0.024), respectively. Figure 5.6 shows the anisotropy distribution histogram of FL molecules inside 100 nm (Figure 5.6A), 200 nm (Figure 5.6B), and 400 nm liposomes (Figure 5.6C), respectively. Through the comparison of the histograms, it was very apparent that the same trend was followed, that is, the larger the size of the liposomes, the smaller the anisotropy of FL molecules in the liposomes.

These results indicate that, similar to R6G molecules inside the liposomes, FL molecules enjoy more rotational motions in a less confined compartment. This can be explained as follow: as the diameter increases, the volume of the water pool increases more than the surface area does, and therefore the fraction of molecules in the water pool to the molecules at the surface increases, resulting in an increase in FL's mobility in the liposome.

Table 5.2 Anisotropy of FL in liposomes of different sizes

Liposomes 100 nm	Liposomes 200 nm	Liposomes 400 nm
0.160 ± 0.039	0.124 ± 0.024	0.063± 0.024

Compared to R6G-liposomes, the decrease in the anisotropy of FL is more dramatic as the liposomes' size increases: a 61% decrease from 100 nm to 400 nm. This could be because the FL molecules at the lipid surface that represent the slow (mobility) component are less attracted to the lipid surface compared to R6G molecules at the same area. As Figure 5.5 shows, the electrostatic interaction between zwitterionic DMPC and negatively charged FL might help to draw some FL molecules close to the lipid surface. However, unlike R6G, FL is more hydrophilic. The solubility of FL disodium salt (600 g/L) in water is 30 times larger than that of R6G (http://www.chemicalland21.com). So it is more likely that FL prefer to stay in the water pool or at least at the lipid-water interface that close to the water pool, rather than inside the lipid bilayer. In addition, FL is unlikely to form

hydrogen bonding with the lipid, which otherwise might help attracting FL to the lipid surface.

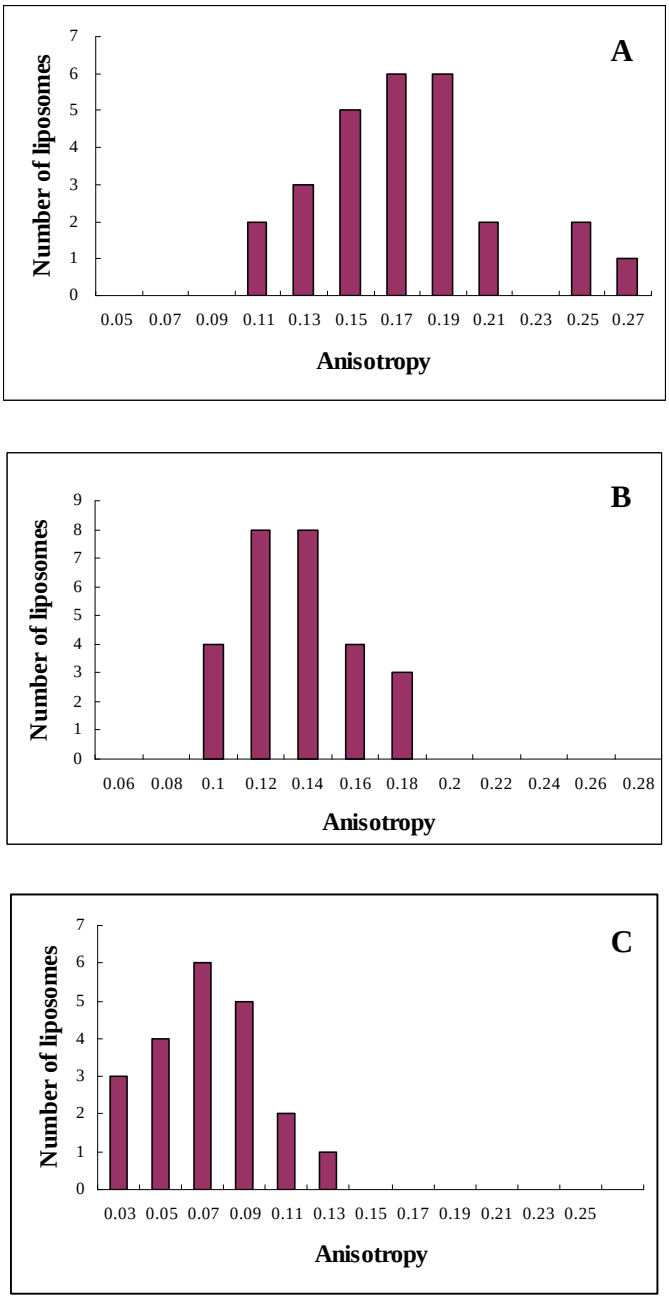

Figure 5.6 The fluorescence anisotropy distribution of FL-liposomes
A. 100 nm liposomes; B. 200 nm liposomes; C. 400 nm liposomes

5.4 Conclusion

We examined how the submicroscopic confinement exerted by the liposomes might affect the mobility of the charged molecules encapsulated inside. R6G and FL molecules were chosen as fluorescence probe due to their opposite charge and similar structure. R6G and FL molecules were entrapped inside the submicroscopic liposomes of various sizes (100 nm, 200 nm, and 400 nm in diameter), which were subsequently incorporated in the hydrogel. Fluorescence modulation and fluorescence anisotropy were used to measure the mobility.

Trapping R6G molecules in the liposomes improved the mobility of R6G in the hydrogel. This confirmed that liposomes were able to protect the entrapped R6G molecules from directly contacting with the hydrogel matrix and thus avoid the electrostatic interactions between R6G and the sol-gel host.

R6G in the liposomes in the hydrogel had lower mobility compared to R6G in the solution, indicating that while avoiding a direct interaction with the hydrogel, liposomes also exerted a confinement effect on the mobility of R6G trapped inside. The restricted mobility might come from the R6G population residing at the lipid bilayer and at the lipid-water interface, which are less mobile due to a combination of several factors, including slower solvation dynamics, electrostatic interaction, hydrophobic interaction, and possibly hydrogen bonding.

Among all R6G-liposomes, R6G mobility increase as the liposomes' diameter

increases. Our explanation for this result is: as the liposomes become larger, both the surface area and the volume of the liposomes increase. However, the volume increases more than the surface area does, resulting in a larger fraction of FL population in the water pool and therefore an increase in mobility.

Study of FL molecules inside liposomes of various sizes also indicates that FL molecules enjoy more rotational motions in a less confined compartment. Meanwhile, it is noticeable that there is a dramatic decrease (61%) in the anisotropy of FL as the liposomes' diameter changes from 100 nm to 400 nm, compared to those of R6G. This implies that the FL molecules residing at the surface might be less attracted to the lipid surface, compared to R6G molecules. Thus, the FL population with a slow mobility attributes less to the overall mobility of FL molecules as the liposomes' size increases.

Chapter 5 References

(1) Ellerby, L. M.; Nishida, C. R.; Nishida, F.; Yamanaka, S. A.; Dunn, B.; Valentine, J. S.; Zink, J. I. *Science* **1992**, *255*, 1113.

(2) Jin, W.; Brennan, J. D. *Anal. Chim. Acta* **2002**, *461*, 1.

(3) Gill, I. *Chem. Mater.* **2001**, *13*, 3404.

(4) Pierre, A. C. *Biocatal. Biotransform.* **2004**, *22*, 145.

(5) Avnir, D.; Coradin, T.; Lev, O.; Livage, J. *J. Mater. Chem.* **2006**, *16*, 1013.

(6) Gilliland, J. W.; Yokoyama, K.; Yip, W. T. *Chem. Mater.* **2004**, *16*, 3949.

(7) Gilliland, J. W.; Yokoyama, K.; Yip, W. T. *J. Phys. Chem. B* **2005**, *109*, 4816.

(8) Zhou, Y.; Yip, W. T. *J. Phys. Chem. B* **2009**, *113*, 5720.

(9) Gilliland, J. W.; Yokoyama, K.; Yip, W. T. *Chem. Mater.* **2005**, *17*, 6702.

(10) Li, Y.; Yip, W. T. *J. Am. Chem. Soc.* **2005**, *127*, 12756.

(11) Kim, T.-S.; Dauskardt, R. H. *Nano Lett.* **2010**, *10*, 1955.

(12) Zorn, R.; Mayorova, M.; Richter, D.; Schonhals, A.; Hartmann, L.; Kremer, F.; Frick, B. *AIP Conf. Proc.* **2008**, *982*, 79.

(13) Amanuel, S.; Malhotra, V. M. *J. Appl. Polym. Sci.* **2006**, *99*, 3183.

(14) Schönhals, A.; Goering, H.; Schick, C.; Frick, B.; Zorn, R. *J. Non-Cryst. Solids* **2005**, *351*, 2668.

(15) Sen, P.; Mukherjee, S.; Halder, A.; Dutta, P.; Bhattacharyya, K. *Res. Chem. Intermed.* **2005**, *31*, 135.

(16) Xie, X. S.; Dunn, R. C. *Science* **1994**, *265*, 361.

(17) Ha, T.; Enderle, T.; Chemla, D. S.; Selvin, P. R.; Weiss, S. *Phys. Rev. Lett.* **1996**, *77*, 3979.

(18) Loughnane, B. J.; Fourkas, J. T. *J. Phys. Chem. B* **1998**, *102*, 10288.

(19) Loughnane, B. J.; Farrer, R. A.; Fourkas, J. T. *J. Phys. Chem. B* **1998**, *102*, 5409.